Increase of photovoltaic panels lifespan by monitoring and control

Bechara Nehme

Aix-Marseille Université
LSIS UMR 7296

USEK

T H È S E

présentée à

Université d'Aix-Marseille

pour obtenir le titre de
Docteur de l'Université d'Aix-Marseille , spécialité Automatique (ED184)

par Monsieur

Bechara Nehme

Augmentation de la durée de vie des Panneaux Photovoltaïques par surveillance et contrôle

Laboratoire des Sciences de l'Information et des Systèmes

Thèse préparée en co-direction entre l'AMU au LSIS (France) et L'USEK à la Faculté d'Ingénierie (Liban)

Soutenance à Marseille le 27 Mai 2016

devant le jury composé de

Président et Rapporteur	:	M Giuseppe Marco Tina	-	Professeur à l'Université de Catane
Rapporteur	:	M Fernando Tadeo Rico	-	Professeur à l'Université de Valladolid
Examinateurs	:	Mme Geneviève Dauphin-Tanguy	-	Professeur à l'École centrale de Lille, CRIStAL UMR CNRS
	:	M Yasser Gaber Dessouky	-	Professeur à l'Arab Academy for Science, Technology & Maritime Transport
Membres Invités	:	M Abdelhamid Rabhi	-	Maître de Conférences Université de Picardie Jules Verne, MIS
	:	M Franck Medlege	-	Docteur Ingénieur au CEA
Encadré par	:	M Nacer Kouider M'Sirdi	-	Professeur à Aix-Marseille Université, LSIS UMR CNRS
Co-Directeurs	:	Mme Tilda Karkour Akiki	-	Professeur Assistant à l'Université Saint-Esprit de Kaslik
	:	M Aziz Naamane	-	Maître de Conférences à Aix-Marseille Université, LSIS UMR CNRS

Acknowledgment

Foremost, I would like to express the deepest appreciation to my thesis director, Mr. Nacer Kouider M'SIRDI, professor at Polytech Marseille of Aix-Marseille Université (AMU), and director of the SASV project of the LSIS laboratory. Prof Nacer has the attitude and the substance of a project director. He continually conveyed me guidelines and support to realize this project. Without his help, the project would not be possible.

I would also like to express my deep gratitude to my co-director, Mrs. Tilda KARKOUR AKIKI, assistant professor at the Faculty of Engineering of the Holy Spirit University of Kaslik (USEK), and chairperson of the Electrical and Electronics Engineering Department. Dr. Tilda showed the greatest support, advise, valuable comments, and encouragement. She has the spirit of caring and supporting. Without her effort, all research grants and travel opportunities could not be ensured.

I would like to express the deepest appreciation to Mme Geneviève DAUPHIN-TANGUY, professor at the École centrale de Lille and researcher at the CRIStAL laboratory, for accepting the role of examiner and for chairing my defense committee.

I would like to express my deep gratitude to Mr Giuseppe Marco TINA, professor at the University of Catania, for accepting the role of reporter and for traveling from Italy to France to attend the defense.

I would like to express the deepest appreciation to Mr Fernando Tadeo RICO, professor at the University of Valladolid, for accepting the role of reporter and for traveling from Spain to France to attend the defense.

I would like to express my deep gratitude to Mr Yasser Gaber DESSOUKY, dean of Scientific Research and Innovation of the Arab Academy for Science and Technology and Maritime Transport, for accepting the role of examiner and for traveling from Egypt to France to attend the defense.

I would like to express the deepest appreciation to Mr Abdelhamid RABHI, Maître de Conférences at the Université de Picardie Jules Verne and researcher at the MIS laboratory, for his advise during my research and for attending my defense.

I would like to express my deep gratitude to Mr Franck MEDLEGE, Docteur Ingénieur at the CEA, for attending my defense.

I would also like to express the deepest appreciation to my thesis co-supervisor, Mr. Aziz NAAMANE, Maître de Conférences at Polytech Marseille of Aix-Marseille Université. Dr. Aziz showed the highest suggestions, remarks, and advise. He has the spirit of friendship and assistance.

I would also like to express the deepest appreciation to Mr. Mustapha OULADSINE, director of the LSIS laboratory, for welcoming me within the laboratory.

I would also like to express my deep gratitude to Mr. Pascal DAMIEN, dean of the Faculty of Engineering of USEK, for welcoming me within the faculty and for facilitating me the opportunity to seek my doctoral degree.

I would also like to express the deepest thanks to Mr. Barbar ZEGHONDY, associate professor at the Faculty of Engineering of the Holy Spirit University of Kaslik (USEK), and chairperson of the Chemical Engineering Department, for the advise and help he offered during my research.

Finally, I would like to express my deep thanks to my family for supporting me during my doctoral studies. They showed the best support and encouragement.

Abstract

Conversion efficiency of solar cells is now on average reaching 15%. Despite these acceptable yields, it remains important to raise a technological limitation: the improvement of the life span of photovoltaic modules. Effects are observed during the use of these components in intermittent weather: rain, snow, molds, dust UV rays, shock, corrosion etc... rapid losses of optoelectronic properties depending on the usage conditions. The objective of this thesis is in twofold: -to try to improve the lifespan of solar panels, and -to improve the reliability of the photovoltaic modules by decreasing their degradation rate.

Our approach begins by taking into account the effects of aging of photovoltaic modules whose degradation is related to temperature, moisture, Ultra violet light, cracks etc... Faults are analyzed and studied to understand the impact and the importance of each parameter in the different modes of degradation to develop simulation models that take into account external environmental conditions.

Control algorithms have been developed for a best utilization avoiding defects and allowing photovoltaic modules to operate in optimal conditions for mitigation of degradation processes.

Keywords: photovoltaic panels, degradation, faults, lifespan, control, modeling, thermal behaviour.

Résumé

Les rendements de conversion des cellules solaires atteignent en moyenne aujourd'hui 15%. Malgré ces rendements acceptables, il reste un verrou technologique important à lever : l'amélioration de la durée de vie des modules photovoltaïques. On observe en effet au cours de l'utilisation de ces composants dans des conditions climatiques intermittentes : pluie, neige, moisissures, poussières rayons UV, chocs, corrosion etc.... une perte rapide des propriétés optoélectroniques en fonction des conditions d'utilisation.

L'objectif de cette thèse est d'essayer d'améliorer la durée de vie des panneaux solaires et d'améliorer la fiabilité des modules en diminuant le taux de dégradation.

Notre approche commence par prendre en compte les effets de vieillissement et des défauts des modules photovoltaïques dont la dégradation est liée à la température, humidité, à la lumière Ultra violette, les fissures etc.... Les défauts de fonctionnement sont analysés et étudiés pour comprendre l'effet et l'importance de chaque paramètre dans les différents modes de dégradation afin de développer des modèles de simulation qui tiennent compte des conditions environnementales.

Des algorithmes de commande ont été développés pour une utilisation qui évite au mieux les défauts et permet aux modules photovoltaïques de fonctionner dans des conditions optimales pour l'atténuation des dégradations.

Mots clés: panneaux photovoltaïques, dégradation, défauts, durée de vie, contrôle, modélisation, comportement thermique.

Cette thèse, préparée en co-direction avec l'Université de Saint Kaslik et dans la collaboration du HyRES Lab, du LSIS et de l'USEK, ouvre des perspectives très intéressantes pour l'exploitation des énergies renouvelable en ville (méditerranéenne) à moindre coût et d'une manière très efficace et à moindre coût, grâce aux outils mis au point.

Acronyms

AAST: Arab Academy for Science, Technology & Maritime Transport.
AC: Alternating Current.
AM: Air Mass.
AMU: Aix-Marseille Université.
ANN: Artificial Neural Networks.
ARC: Anti Reflective Coating.
AUF: Agence Universitaire de la Francophonie.
a-Si:H: Hydrogenated Amorphous Silicon.
BOS: Balance Of System.
BSF: Back-Surface Field.
CNRS: Centre National de la Recherche Scientifique.
COP: Conference Of the Parties.
CTE: Coefficient of Thermal Extension.
DAQ: Data Acquisition System.
DC: Direct Current.
DEE: Differential Equation Editor.
DH: Damp Heat Test.
DSSC: Dye-Sensitized Solar Cells.
DYI: Delta Yellowness Index.
EFG: Edge-defined Film-fed Growth.
EMS: Energy Management Systems.
ESC: Extremum Seeking Control.
EVA: Ethylene Vinyl Acetate.
FF: Fill Factor.
FLC: Fuzzy Logic Controllers.
HC: Hill Climbing.
HCR: Higher Center for Research.
HOMO: Highest Occupied Molecular Orbital.
HyRES: Hybrid Renewable Energy Sources.
ICT: Information and Communications Technology.
IncCond: Incremental Conductance.
LID: Light Induced Degradation.
LSIS: Laboratoire des Science de l'Information et des Systèmes.
LUMO: Lowest Unoccupied Molecular Orbital.
LWFE: Large Work Function Electrode.
MEPO: Modified Enhanced Perturb and Observe.
MID: Moisture Induced Degradation.
MIS: Modélisation, Information & Systèmes.
MLP: Maximum Lifetime Point.
MOSFET: Metal–Oxide–Semiconductor Field-Effect Transistor.
MPP: Maximum Power Point.
MPPT: Maximum Power Point Tracking.
Mo: Molybdenum.
NAE: National Academy of Engineering.
NASA: National Aeronautics and Space Administration.
NCC: NonCurrent Carrying.
NL-ESC: Newton Like Extremum Seeking Control.
NOCT: Nominal Operating Cell Temperature.
OC: Open Circuit.

ODE: Ordinary Differential Equation.
PERL: Passivated Emitter and Rear Locally diffused.
PID: Potential Induced Degradation.
PO: Perturb and Observe.
PV: Photovoltaic.
PVT: Photovoltaic Thermal hybrid collector.
PWM: Pulse Width Modulation.
RES: Renewable Energy Sources.
RH: Relative Humidity.
RMEI: Réseau Méditerranéen des Ecoles d'Ingénieurs.
SASV: Systèmes Automatisés à Structure Variable.
SC: Short-Circuit.
SF: Silicon Film.
SR: Spectral Response.
SRV: Surface Recombination Velocity.
STC: Standard Test Conditions.
STR: STring Ribbon.
SWE: Staebler-Wronski Effect.
SWFE: Small Work Function Electrode.
Si: Silicon.
TBP: *Tert*-Butylpyridine.
TCO: Transparent Conductive Oxide.
TEPSI: Thermal Electric Solar Panel Integration.
TF: Thin Film.
TJIC: Tunnel-Junction Interconnect.
UMR: Unité Mixte de Recherche.
USEK: Holy Spirit University of Kaslik.
USMBA: Université Sidi Mohamed Ben Abdellahde Fès.
UV: Ultraviolet.
UVD: Ultraviolet light Degradation.
WVTR: Water Vapor Transmission Rate.
YI: Yellowness Index.

Contents

List of Figures

List of Tables

General Introduction

Humanity is in continuous demand of energy. Since the dawn of time, the tribes have initiated wars to possess energy (fire). They improved their weapons by heating iron and progressed in development. Today the form of energy changed to oil, gas, and electricity. Thus, earth is in constValues of the eant threat of pollution mainly originated from energy production. Humanity has organized many events to fight against climate change, we enumerate: The Kyoto Protocol (1997), The Copenhagen Summit (2009), COP 21 (Conference Of the Parties) (2015). Other action plans have been initiated to encourage and force the penetration of renewable energy sources, we enumerate: the Russian Renewable Energy Program (2000), the 25x'25: US resolution for a new national renewable energy goal (2004), the 20-20-20 European Union climate and energy package (2008), and the Zero Carbon Australia Stationary Energy Plan (2010).

Leaders have three main challenges to accomplish: Energy Security, Social Equity, and Environmental Impact Mitigation. PV (Photovoltaic) panels present a serious solution to these challenges. We can list here a number of advantages of using the PV technology:

- Solar energy is the most abundant and equitable source on earth.
- PV panels constitute a green energy source that does not pollute or contribute to climate change.
- PV panels can support electricity to rural places.
- We must note that the third of earth's population does not have access to the electric grid.
- Electricity is the most convertible form of power.
- PV panels are safe and reliable.
- PV panels can be produced from scrap materials of electric industry.
- With automated and intelligent systems, no operators are needed.
- Once installed, no operating cost is required.
- No parts move during PV panel operation.
- PV panels can be integrated in any new or existing building.

Despite these advantages, we must note some disadvantages that limit the development of the PV market:

- The output of PV panels is directly linked to the meteorological conditions of the area.
- The installation cost is high relatively to traditional power generation.
- PV panel's lifetime is small relatively to traditional power generation sources.
- The BOS (Balance Of System) (storage, inverter, DC (Direct Current) to AC (Alternating Current) converter) decreases the reliability and the efficiency of the system.

- PV panel's production is complex and expensive. A PV panel needs at least two years of operation to generate the power used during its fabrication.

The most flagrant disadvantage of PV panels is their initial high cost that leads to a high energy production cost, that is a high kWh cost. The NAE (National Academy of Engineering) defined 14 grand challenges for engineering, for the 21st century. One of these challenges is to "Make Solar Energy Economical" [10]. Besides, the 20-20-20 European Union climate and energy package suggests to increase the lifespan of the photovoltaic panels up to 40 years [11]. Our PhD research aligns with the above two recommendations. Our objective is to increase the lifespan of PV panels by monitoring and control.

One of the main objectives of the SASV (Systèmes Automatisés à Structure Variable) project team of the LSIS (Laboratoire des Science de l'Information et des Systèmes) laboratory is the exploitation of ICT (Information and Communications Technology) for control, prediction, maintenance, diagnosis, and management of RES (Renewable Energy Sources). SASV became interested in control applied to RES, systems of energy production, mixed RES, and the coupling of several HyRES (Hybrid Renewable Energy Sources). The SASV project team has many collaboration in this area through its involvement in the RMEI (Réseau Méditerranéen des Ecoles d'Ingénieurs).

Context

The thesis was held in co-direction between the l'Ecole Polytechnique of the Aix-Marseille Université (AMU) and the Faculty of Engineering of the Holy Spirit University of Kaslik (USEK). The thesis supervisor at Polytech Marseille is Professor Nacer K. M'SIRDI, head of SASV project at LSIS UMR CNRS 7296 (Unité Mixte de Recherche) (Centre National de la Recherche Scientifique). The thesis director at the Faculty of Engineering (USEK) is Dr. Eng. Tilda Karkour Akiki, head of the Electrical and Electronics Engineering Department. This thesis is included in the HyRES Lab. The HyRES lab is an International Associated Laboratory for Mediterranean collaborations on Renewable Energies and sustainable building. This research carried many benefits on the research and development relations between the two institutions. Indeed, this partnership initiated research in the axis of renewable energy within USEK. The field of photovoltaic panels is expected to have an important impact in improving the conditions of energy production for Lebanon, since Lebanon enjoys 300 days of sunshine per year. In reality, power generation deficit overwhelms Lebanon in blackouts, which turns into a vital and economic problem.

This thesis was also conducted in parallel to other thesis at the SASV project team. We enumerate the thesis of Miss Mouna Abarkan on the modeling and analysis of behavior of a building equipped with HyRES in a cooperation with l'Université Sidi Mohamed Ben Abdellahde in Fès (USMBA) [12] [13]. The thesis of Mr. Motaz Amer on power consumption optimization based on controlled demand for smart home in cooperation with the Arab Academy for Science, Technology & Maritime Transport (AAST) [14]. The thesis of Mrs. Rana Ahmed on energy management and control for renewable energy sources in rural area with the AAST [15, 16].

The cooperation between the SASV project team of the LSIS and the Faculty of Engineering of USEK led to a Mobility Scholarship granted by the AUF (Agence Universitaire de la Francophonie). In addition, a research grant has been given to the project by the HCR (Higher Center for Research) of USEK. The works on the MPPT (Maximum Power Point Tracking) algorithms, reported in chapter 1, were in cooperation between USEK, LSIS, and MIS (Modélisation, Information & Systèmes) laboratory of the Université de Picardie Jules Verne.

Future works are being carried with the participation of different teams from different countries (France, Spain, Italy, Greece, Lebanon, Egypt, Morocco). All teams are gathered within the HyRES lab and the RMEI. In addition, a collaboration for delivering a double diploma in master of electrical engineering is being prepared between AMU and USEK.

Motivation

Several reasons and arguments exist to justify the utility of this researche project. The economic aim always being flagrant does not dominate the environmental causes which may cause threats to human life. Adding also the help presented by our work to the 20-20-20 European project and to the production of electricity in Lebanon.

Economically speaking, the cause that initiates a person to invest in a project is to increase the amount of money originally paid. The investor also calculates the payback period of the project and compares it to the total time of production. For extended lifespan of photovoltaic panels, investors will be more encouraged to adopt solar photovoltaic solutions. Currently Photovoltaic panels are not gainful in France and in Lebanon. However in a few years with the depletion of fossil resources, the production of photovoltaic electricity will be essential to humanity.

Ecologically speaking, the increase in the lifespan of any product is generally favorable. In fact, factories are a major source of pollution and are calling for a substantial amount of electrical energy. The increase in production also causes over-exploitation of raw materials and adding transportation of photovoltaic panels and their accessories from the factory to the recipient increases with lower lifespan.

In 2025, the photovoltaic panels already installed will reach their end of life. They will become electrical waste generating toxic substances to the environment and to humans. Recycling of photovoltaic panels is required by the rules [11]. However, according to experts, recycling is not economically viable due to low volumes of waste generated.

The main cause that require an increase in the lifespan of photovoltaic panels is related to the depletion of raw materials. Some components of photovoltaic panels are aluminum, lead, silver, indium, gallium, and germanium.

Another cause that supports the achievement of this work is the danger of leaching of lead. Lead is a chemical element in the carbon group, it is a bluish gray malleable metal. Lead is a toxic and mutagen element. It has indeed been classified as potentially carcinogenic in 1980 and as probably carcinogenic to humans and animals in 2004. Another cause that involves this research in preserving nature and wildlife is the leaching of cadmium. Cadmium is a white metal, soft and malleable. When cadmium concentrations in the soil are important, they can influence the microorganisms soil processes and threaten the entire ecosystem of the soil. Animals eating or drinking cadmium can sometimes have high blood pressure, liver disease and problems with nerves or brain.

Objectives and Organization

The objective of this research project is to increase the lifespan of PV panels by means of control. In order to achieve this objective, we must start first by studying the degradation process and faults of PV panels. In an other way, what decreases the efficiency of PV panels, and what marks their failure. Then we start investigating a way of using and operating PV panels for alleviating and mitigating their degradations. Then we explicit our monitoring and control strategy to achieve the objective. All the above physical interpretation is accompanied with modeling and simulation.

This report is organized as follows:

Chapter 1 presents general information concerning PV panels. it introduces the history, the technical and physical features behind photovoltaic effect. Then it presents engineering view of photovoltaic solar panels starting by their characteristic, installation, and sizing. Chapter 1 also surveys existing types of PV panels, their operation principles, utility, features, efficiency, and applications. In addition, Chapter 1 presents the work done on MPPT algorithms that were conducted alongside to the PhD work. A comparison of these algorithms is presented. This chapter helps to understand the operation of PV panels and presents a solid base to be upgraded in chapter 5.

Chapter 2 surveys the degradation modes and faults of PV panels. Degradation modes leads to a continuous decrease in efficiency, and faults occurring to panels leads to a sudden decrease in power production.

Chapter 3 shows our main contribution in this project. It starts by presenting a brand new PV

panel physical model (ideal model). Then it presents a PV model that takes into consideration its degradation modes. A real-time simulation model presents the variation of the equivalent circuit of the PV panel as a function of time. In addition, faults modeling is also presented. Model validation using real hardware is presented to ensure a good representation of the real panel.

Chapter 4 presents a thermal model of PV panels. We noticed that degradation and faults are caused by external environmental conditions, where temperature plays an important and common parameter in all degradation modes and faults of PV panels. In this chapter, thermal behavior of PV panels is explained and modeled giving new findings. The model is validated with real hardware.

Chapter 5 presents our faults characterization and control actions necessary to increase the lifespan of PV panels. The diagnosis algorithm identifies faults occurring to PV panels and helps maintaining the system. Our actions mitigate the degradation process of PV panels and increase their energy production.

List of Publications

Publications

A1. Nehme, B., M'Sirdi, N. K., Akiki, T., & Naamane, A.. Real-time Thermo-Electrical model of PV panels for degradation assessment. Submitted to the IEEE Journal of Photovoltaics.

A2. Nehme, B., M'Sirdi, N. K., Akiki, T., & Naamane, A. (2014). Contribution to the modeling of ageing effects in PV cells and modules. Energy Procedia, 62, 565-575.

A3. M'Sirdi N. K., Rabhi A., Nehme B. (2015). THE VSAS APPROACH GIVES THE BEST MPPT FOR SOLAR. journal of renewable energy and sustainable development, 1, 60-71.

Conference papers

C1. M'Sirdi, N. K., Nehme, B., Abarkan, M., & Rabbi, A. (2014, November). The best MPPT algorithms by VSAS approach for Renewable Energy Sources (RES). In Environmental Friendly Energies and Applications (EFEA), 2014 3rd International Symposium on (pp. 1-7). IEEE.

C2. Nehme, B., M'Sirdi, N. K., & Akiki, T. (2014, November). A geometric approach for PV modules degradation. In Renewable Energies for Developing Countries (REDEC), 2014 International Conference on (pp. 49-53). IEEE.

C3. Bechara Nehme, Tilda Akiki, Nacer K. M'Sirdi. Modeling the degradation modes of PV panels as addition events. To be published in MGEF 2015.

C4. Bechara Nehme, Nacer K. M'Sirdi, Tilda Akiki. Survey on PV panels: materials and types. To be published in MGEF 2015.

C5. Nacer, K., M'Sirdi, N. K., Rabhi, A., & Nehme, B. THE VSAS APPROACH GIVES THE BEST MPPT FOR SOLAR ENERGY SOURCES (RES). To be published in MGEF 2015.

C6. Bechara Nehme, Nacer K. M'Sirdi, Tilda Akiki, Assessing the Effect of Temperature on Degradation Modes of PV Panels To be published in MedICT'2015

Chapter 1

General information on Photovoltaic Panels

1.1 Introduction

In this chapter general information concerning PV panels is presented. We start by resuming the history, the principle of operation and the physics of the solar cell. In addition we present semiconductors, their doping, and the physics of the PN junction. We then start by reviewing the engineering behind PV panels: equivalent circuit, I-V characteristic, efficiency limit, installation and sizing. We also survey existing types of PV panels, their operational principle, utility, features, efficiency, and application.

In this chapter we study MPPT algorithms that are related to RES. We conduct a comparative study between different MPPT algorithms. The study will grant us understandings and knowledge of the operation of PV panels. The latter will be explored in chapter 5.

1.2 History

It was Alexandre-Edmond Becquerel who discovered the photovoltaic effect in 1839. The photovoltaic effect is the phenomena of producing electricity from a semiconductor when it is exposed to light. The photovoltaic effect was applied to Se (Selenium). The first PV panel with 6% efficiency was developed by Chapin, Pearson, and Prince in 1954. NASA (National Aeronautics and Space Administration) started using PV panels to power up satellites in 1958. Many countries started developing PV systems because of the oil crisis in 1973. Then PV technology started to grow from 1MW power plant (1982) to 6MW power plant (1984). The total peak power installed in 1999 reached 1000MW, this power doubled by 2002. Now the total worldwide installed PV panel's power exceeds 100GWp [2].

1.3 Principle of operation

A conductor is a material possessing a high number of free electrons; it conducts the electrical current. An electric insulator has no free electrons; it blocks current from flowing. A semiconductor is a body having a resistivity intermediate between that of the conductor and the insulator. A semiconductor possesses electrons situated in the valence band (the farthest layer from the nucleus). These electrons are called valence electrons. If these electrons acquire some energy which exceeds the band gap energy, they become free to navigate in the conduction band. Thus the resistivity of the semiconductor decreases. Heat and light are two examples of energy sources that extract electrons from the valence band. Photons, particles of light, hit valence electrons and carry them to conduction band. The built in voltage drive electrons to the external circuit. If an electron is freed by a photon carrying energy more than the band gap energy, the electron can do some useful work in an external electric circuit.

1.3.1 Semiconductors

The electronic configuration of silicon is:
Si: $1s^2\ 2s^2\ 2p^6\ 3s^2\ 3p^2$

We can see that the valence band contains 4 electrons. The top band is then partially filled with electrons, which describes well the state of semiconductors. In fact, the top band of conductors contains a small number of electrons and this band is called the conduction band. The top band of isolators is filled with electrons. Each electron is qualified by his energy and by his join to a band. This quantum mechanics approach is derived by solving the Schrödinger equation and obtaining the electron wave function, ψ:

$$\nabla^2\psi + \frac{2m}{\hbar^2}\left(E - U(\overrightarrow{r})\right)\psi = 0 \tag{1.1}$$

Where:
m: electron mass in g.
$\hbar$: the reduced plank constant in $eV.s$.
E: energy of the electron in eV.
$U(\overrightarrow{r})$: periodic potential energy in eV.

Introducing k, the wave vector of the electron wave function, we can define the crystal momentum [2]:

$$p = \hbar k \tag{1.2}$$

Knowing that [17]:

$$E = \frac{\hbar^2 k^2}{2m} \tag{1.3}$$

And knowing that the wave function is periodic for chain of atoms of length L [17]:

$$\psi(x + L) = \psi(x) \tag{1.4}$$

For solving the Schrödinger equation and respecting the above conditions, the allowable values of the wave vector k are [17]:

$$k = N \times \frac{2\pi}{L} \tag{1.5}$$

Where N is an integer.

This study is made for linear approach and the wave vector is taken a scalar for simplicity.

According to the Schrödinger equation, electrons occupy bands with discrete levels. A forbidden band is also noticed. This leads to the quantum repartition of electrons in the atom.

The forbidden band (or band gap) separates the valence band from the conduction band. The energy width of the band gap is called energy gap Eg.

$$E_g = E_c - E_v \tag{1.6}$$

Where :
E_c: bottom of the conduction band energy in eV.
E_v: Top of the valence band energy in eV.

For conductors, the band gap is small, the conduction band is partially filled with electrons. If an electric field is applied to a conductor, the conduction band electrons present at the Fermi level can jump to a higher level and move in the conductor. The Fermi level is defined as the level over which no electrons exist see (figure 1.1). For insulators, the band gap is high (more than $4eV$), the conduction band is empty. If an electric field is applied to an insulator, the valence band electrons present at the Fermi level cannot jump to the conduction band. If we apply a very high electric field, electrons can

leave the valence band and cross the high energy gap to reach the conduction band. This is called the dielectric break down.

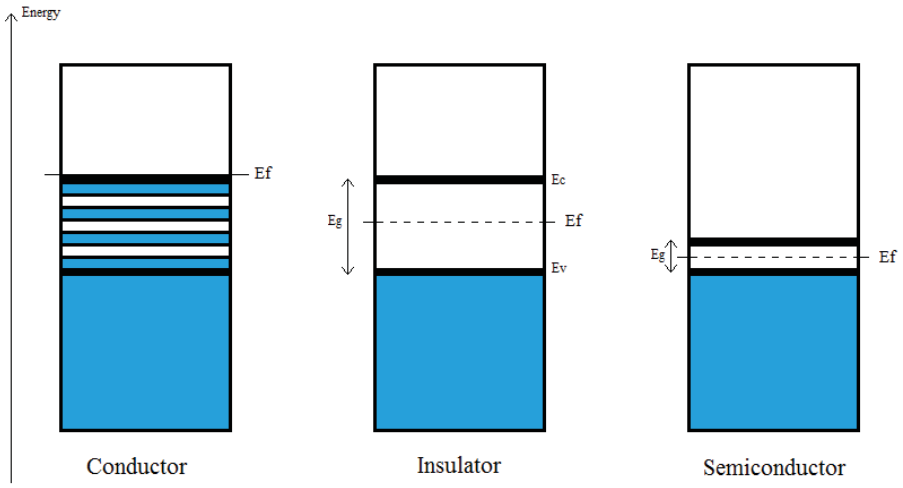

Figure 1.1: Energy diagram of conductors, insulators, and semiconductors.

For semiconductors, the band gap is small (1.1 eV for silicon and 0.67 eV for germanium), the conduction band is empty. At absolute zero, a semiconductor acts like an insulator. If the temperature increases, some electrons of the valence band can jump to the conduction band creating a hole in the valence band. This process is called "electron-hole generation" and the semiconductor is at an excited state. If we apply an electric field to the excited state of a semiconductor, electrons of the conduction band and holes of the valence band will contribute to conduction. Electrons will move in the opposite direction of the electric field, in the conduction band. Holes will move in the direction of the electric field, in the valence band. The current density ($C.m^{-2}.s$) is given by:

$$J = e \times n_e \times v_e + e \times n_h \times v_h \tag{1.7}$$

Where:
e: the electron charge in $C.particule^{-1}$.
n_e, n_h: respectively the electron and hole densities in $particule.m^{-3}$.
v_e, v_h: respectively the electron and hole velocities in $m.s^{-1}$.

We must note that the electron and hole velocities are different. In fact, the electrons move in the conduction band and the holes moves in the valence band. In conclusion, the resistivity of semiconductors decreases with temperature. Many mechanisms like heat can conduct to electron hole generation. We may list: field emission effect (applying a high electric field to a semiconductor), light (photovoltaic effect) and thermal vibrations (vibrating the silicon atoms to break the bonds between atoms).

1.3.1.1 Direct and indirect band gap semiconductor

A direct band gap semiconductor is a semiconductor where the maximum energy of the valence band and the minimum energy of the conduction band occur at the same momentum (e.g. GaAs, GaInP, CdTe, Cu(InGa)Se_2...). When the maximum and minimum do not align, the semiconductor is an indirect band gap semiconductor (Si, Ge, Sn...) [2].

1.3.1.2 Fermi energy

The Fermi energy level is the energy level over which no filled bands exist. Following this definition, the Fermi energy is then taken as the midpoint of the band gap for semiconductors and insulators. It is the maximum energy level of the conduction band for conductors.

1.3.1.3 Doping

The resistivity of intrinsic semiconductors is high; semiconductors are not useful until they are doped. For example, when silicon (semiconductor of the fourth group in the periodic table) is doped with phosphorus (fifth group), an electron is generated to the conduction band. As phosphorus and silicon have almost the same atomic radius, a phosphorus atom can replace a silicon atom in the crystal. The phosphorus atom will form four bounds with 4 neighboring silicon atoms and will generate a free electron to the crystal figure 1.2. The doping rate is 1 to 10^6. Phosphorus is called donor because it has donated an electron to the crystal. And we have an n-type material. We define N_D the number of donors per unit volume in an n-type material.

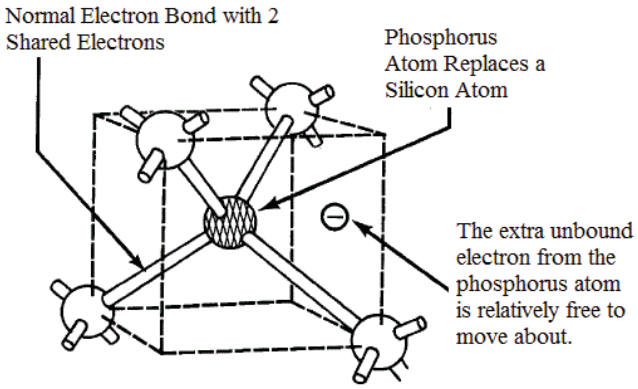

Figure 1.2: Crystal lattice of a n-doped silicon semiconductor [1].

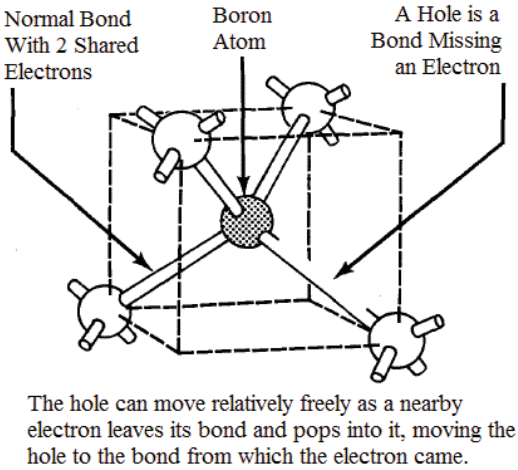

Figure 1.3: Crystal lattice of a p-doped silicon semiconductor [1].

When silicon is doped with boron (third group) a hole is generated in the valence band. A boron atom can replace a silicon atom in the crystal. The boron atom will form four bounds with 4 neighboring silicon atoms and will generate a hole in the crystal figure 1.3. The doping rate is 1 to 10^6. Phosphorus is called acceptor because it has accepted an electron from the crystal. And we have a p-type material. We define N_A the number of acceptors per unit volume in a p-type material.

1.3.1.4 Photovoltaic Effect

As mentioned before, in semiconductors, the energy level of a valence electron can be increased and the latter electron will become in the conduction band. This process of electron hole generation can be achieved by photon absorption (fundamental absorption). Many rules must be taken into consideration for photovoltaic effect. Fist, the energy of the incident photon must be greater or equal to the band gap energy. The photon energy is given by:

$$E = \frac{hc}{\lambda} \tag{1.8}$$

Where :
h: constant of Plank in $eV.s$.
c: speed of the light in $m.s^{-1}$.
λ: wavelength in m.

This first rule implies taking into consideration the frequency spectrum of sun light when designing PV panels and choosing semiconductors. With a $1.11eV$ band gap, silicon is the most used semiconductor in PV panels industry. As $1.11eV$ is the most suited band gap for terrestrial solar radiation.

Second, the initial and final wave vector of the electron must be the same. The transitions are called vertical or direct transitions. In figure 1.4, transition a is possible but transition b is not.

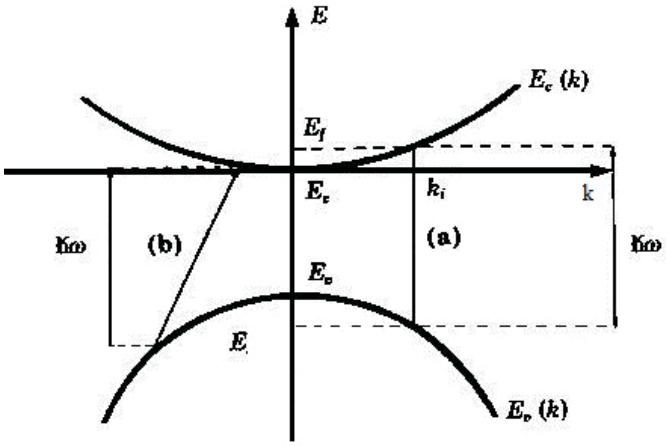

Figure 1.4: Possible and impossible transitions of direct band gap semiconductors [2].

Third, in direct band gap semiconductors (GaAs, GaInP, CdTe, and Cu(InGa)Se_2), the electron hole generation is explained as above. However, in indirect band gap semiconductors (Si and Ge), the electron hole generation requires the emission or absorption of an additional particle; the phonon. Phonons are particles having high momentum (wave vector) with low energy. In figure 1.5, the fundamental absorption of a photon by a valence electron can be accompanied with a phonon absorption or emission so that the electron attends the final state E2.

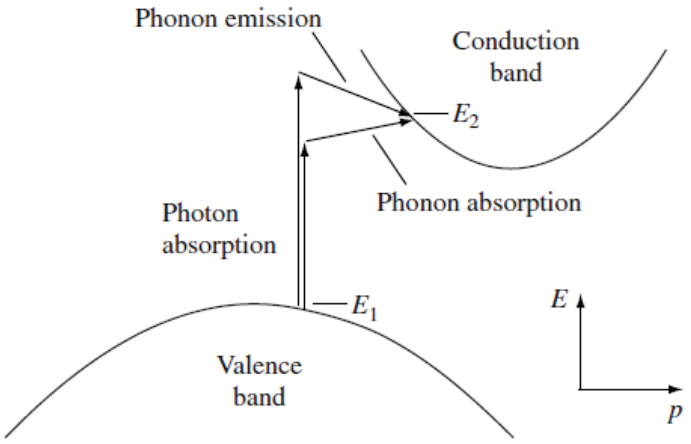

Figure 1.5: Possible transitions in indirect band gap semiconductors [2].

Fourth, the probability of transition of a valence electron to the conduction band is proportional to the density of electrons present in the valence band, to the number of available final places. To the phonon availability (regarding energy and momentum) when dealing with indirect band gap semiconductors.

Fifth, the total energy of all particles taking part in the electron hole generation must be conserved. In PV panels, if the energy of an absorbed photon is greater than the energy gap, the electron can do some useful work in the external circuit.

1.3.1.5 The recombination

If a process (e.g. light) applied on a semiconductor continuously generates electron-hole pairs, the resistivity of the latter semiconductor must theoretically decrease to zero. However, in reality, a phenomenon called recombination will cease this resistive decrease. The recombination is the inverse of electron-hole pair generation. We define exciton, the excited electron (present in the conduction band) and the corresponding hole (present in the valence band) that attract each other. The destruction of the exciton or the electron-hole joint is called recombination. The phenomenon of recombination can generate a photon or a phonon [2, 17]. The most important three recombination mechanisms are: The radiative recombination: it is also called band to band recombination, when an electron, in the conduction band, falls back to its place in the valence band and generates a photon. The recombination through traps in the forbidden gap: when we have impurities in the crystal, an electron can be captured by an impurity. The energy of the electron may be in the forbidden band gap. Then the hole is attracted to the level of the electron and the electron reaches the valence band. The Auger recombination: it is similar to the radiative recombination. However, in the Auger recombination, the excited electron and the excited hole release energy to phonons before recombination. For a semiconductor, we define n: number of free electrons, p: number of holes, and ni=n=p for intrinsic semiconductors. The recombination rate is proportional to the product of n and p ($n \times p$). In intrinsic semiconductors it is proportional to n_i^2. At equilibrium the generation rate of electron hole pairs must be equal to the recombination rate. For a silicon intrinsic crystal, at 25^oC, $n = p = ni = 1,5 \times 10^{10} particle.cm^{-3}$. The recombination rate for doped semiconductors is proportional for p_n*N_D for n-type semiconductors, where N_D is the number of donors and p_n is the number of holes per unit volume in the n-type semiconductor. And similarly, the recombination rate is proportional to N_A*n_p for p-type semiconductors, where N_A is the number of acceptors and n_p is the number of electrons per unit volume in an p-type semiconductor. We define surface recombination by electron-hole recombination at edges of the semiconductor. Surface recombination decreases the short circuit

current (I_{SC}) (by increasing the dark current) and the open circuit (OC) voltage (V_{OC}). In fact at the edges of the semiconductor, the silicon crystal is discontinued creating energy levels in the band gap. These intermediate energy levels are called surface states. Electrons can be present in the forbidden band and recombine easily figure 1.6. The SRV (Surface Recombination Velocity) defines the surface recombination rate ($\cong 10^6 cm.s^{-1}$). In order to decrease the SRV, many chemical approaches can be undertaken. A BSF (Back Surface Field) is mounted on the back contact. It is a heavily doped p-type silicon layer. The BSF will generate an electric field that repulses electrons from accessing the back contact and thus minimizing the SRV at the back surface. In the front surface, under the metallic grid, a layer of heavily doped n-type layer is added. It decreases the SRV at the front surface. For exposed silicon surface, the discontinuation of silicon is rearranged by adding a layer of SiO_x.

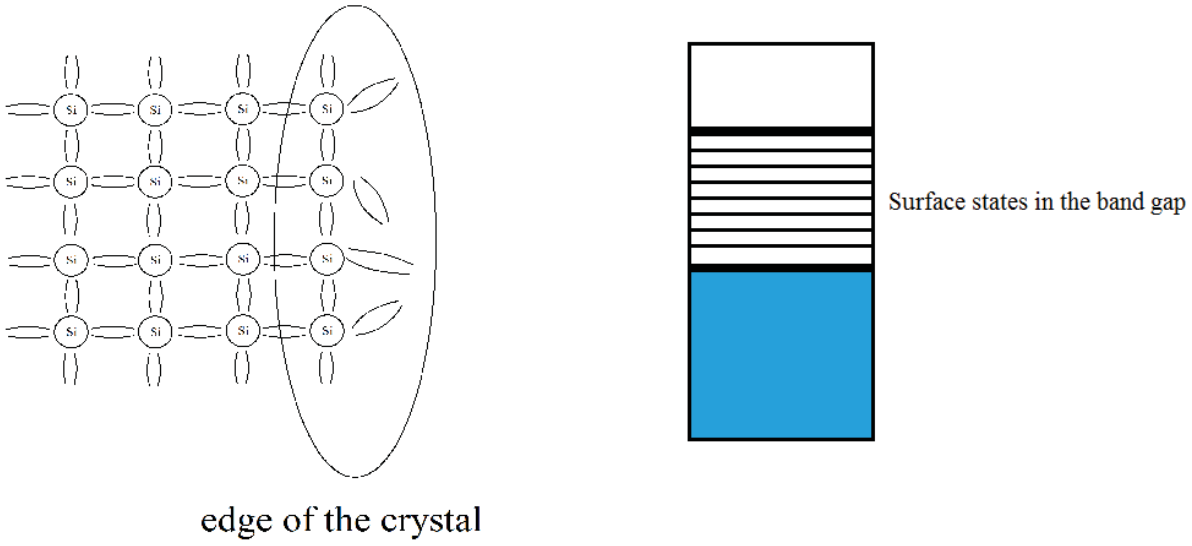

Figure 1.6: Edge of the crystal and its corresponding states.

1.3.2 The PN junction

As seen before, doping of a semiconductor increases its conductivity and creates two electrical types of the latter semiconductor P and N. If we juxtapose the P and N layers of the semiconductor, we form a PN junction. The PN junction is one crystal having a difference of holes and electrons concentration between the P type and the N type. This causes electrons to diffuse to the p-type region and holes to diffuse to the n-type region. The diffusion will cease because electrons and holes are charged particles (they will produce an electrostatic potential difference). In reality, the diffusion current and the drift current will cancel each other's and no net current will be noted. The region where charged particles diffuse is called the depletion region. Assuming that the axis x=0 represents the border of the p-type and n-type regions, the depletion region is defined from $-x_N$ to x_P. Its thickness is inversely proportional to the number of donors N_D in the p-region and inversely proportional to the number of acceptors N_A in the n-region. In fact we must maintain an electric neutrality in the region $N_D{*}x_N{=}N_A{*}x_P$.

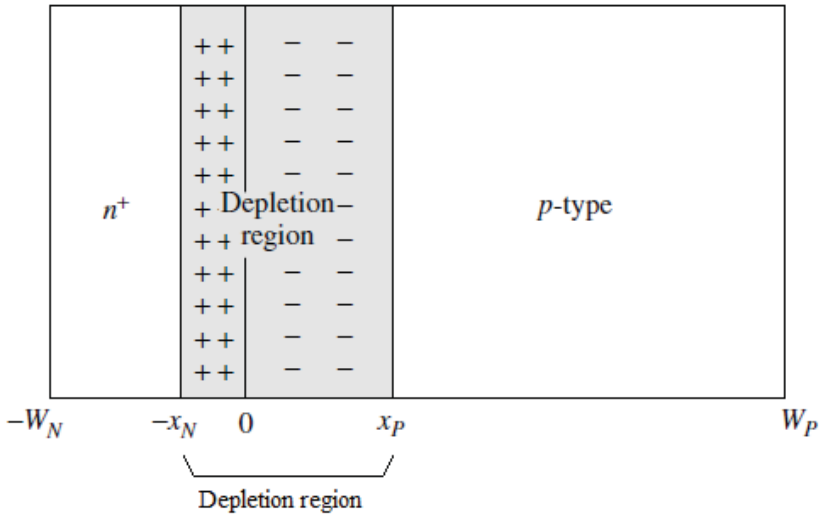

Figure 1.7: The PN junction [2].

In the neutral region (outside the depletion region), we define N_{P0} the density of electrons in the p-region at equilibrium and P_{N0} the density of holes in the n-region. We must always have the following, because of charge neutrality :

$$N_A \times N_{P0} = n_i^2 = N_D \times P_{N0} \tag{1.9}$$

In figure 1.7, we can see a quantitative approach of the PN junction. The depletion region is defined from $-x_N$ to x_P. The analysis of this figure gives the following qualitative approach. The charge of the region $[-x_N, 0]$ is positive and the charge of the region $[0, x_P]$ is negative. This will create a dipole generating a positive electric field E (left to right). This field will allow electrons only to move from the p-region to the n-region. At equilibrium, we can describe a potential energy U to the electric field according to Boltzmann process:

$$\frac{P_{N0}}{N_A} = \frac{N_{P0}}{N_D} = exp\left(-\frac{U}{K_B \times T}\right) = exp\left(-q \times \frac{V_{bi}}{K_B \times T}\right) \tag{1.10}$$

Where:
K_B : Boltzmann constant $1.3806488 \times 10^{-23} m^2.kg.s^{-2}.K^{-1}$.
T : temperature in K.
q: electron charge $1,602 \times 10^{-19} C$.
V_{bi}: built in voltage in V.

The PN junction built in voltage is:

$$V_{bi} = \frac{K_B \times T}{q} \times log\left(\frac{N_D}{N_{P0}}\right) = \frac{K_B \times T}{q} \times log\left(\frac{N_A \times N_D}{n_i^2}\right) \tag{1.11}$$

If we bound an electric contact to the p-region and to the n-region, we get a diode. The p-region is called anode and the n-region is called cathode(see figure 1.8). If we apply a positive voltage (V_{AK}) across the diode (in the opposite way of V_{bi}), we decrease the magnetic field, whose role is to stop the flow of electrons from the n-region to the p-region. And consequently a current I_D (exponentially proportional to V_{AK}) can be seen crossing the diode. If we apply a negative voltage, we can see a very small negative current. This is the fundamental operation of a rectifier. I_D is given by the following equation:

$$I_D = I_{01}\left(exp\left(\frac{e \times V_{AK}}{K_B \times T}\right) - 1\right) \tag{1.12}$$

Where :
I_{01}: the dark saturation current in A.

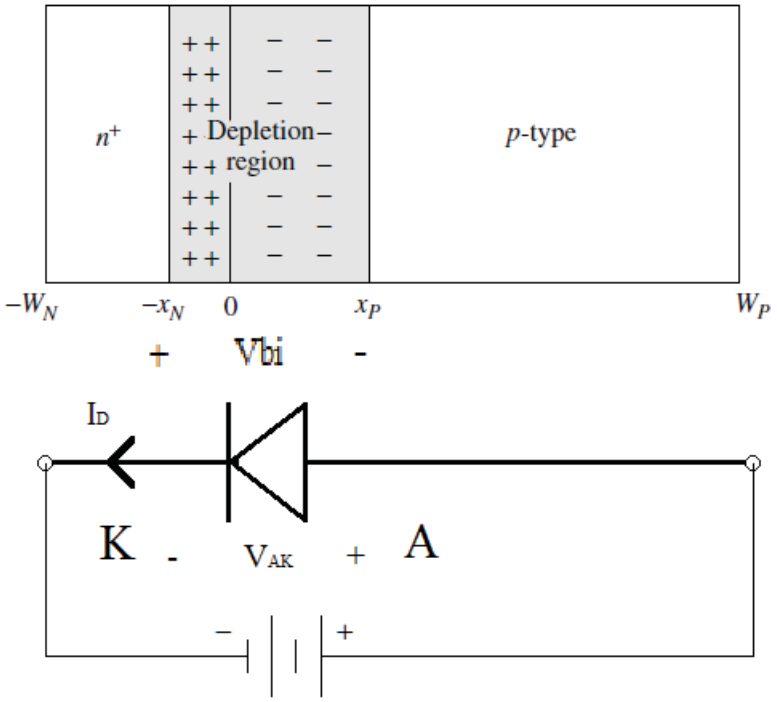

Figure 1.8: Closed circuit fundamental operation of a diode.

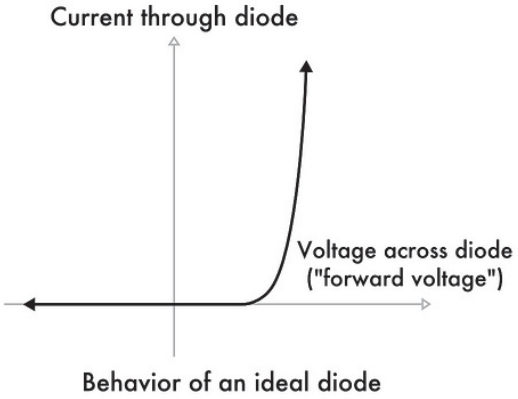

Figure 1.9: The forward current of a diode as a function of the applied voltage.

1.4 The Solar Cell

1.4.1 Electron-hole pair generation

A solar cell is basically a PN junction. An electric contact is mounted to boundaries of the p-region and n-region. The contact of the n-region is a grid allowing sun light to reach the semiconductor. Typically, the doping rate of the n-region is high relatively to the doping rate of the p-type region. The n-region is called the emitter and the p-region is called the base. The emitter is generally thin allowing sun light to reach the base where it can be absorbed. When sun light reaches the n-type silicon layer, electrons are freed, they are collected by the electrical contacts and conducted to the external load via wires. The electrons then return to the metal contact via another wire and reach the holes of the p-type silicon layer. The electrons go through the PN junction and reach the n-type silicon layer; the loop continues [1].

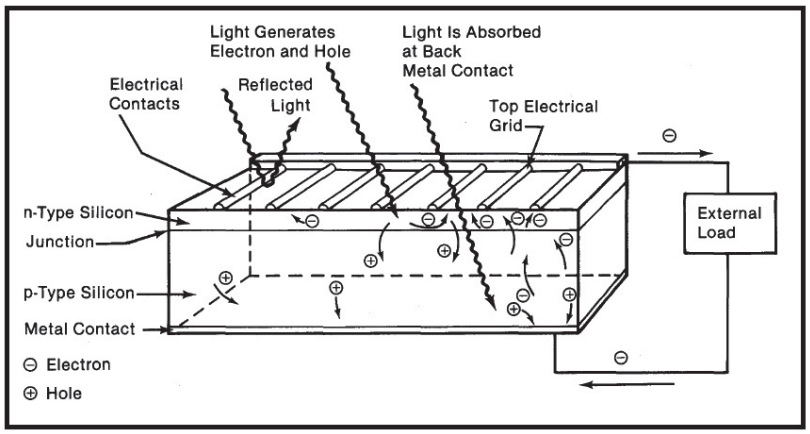

Figure 1.10: Architecture of a PV cell [1].

A BSF is often added to the back of the base. It is a heavily doped region allowing collection of electrons by keeping them away from the back contact.

The electron hole pairs generation rate is an empirical equation (number of electron hole pairs per second per cm^3) [2]:

$$G(x) = (1-s)\int (1-r(\lambda))\, f(\lambda)\alpha(\lambda) exp\,(-\alpha x)\, d\lambda \tag{1.13}$$

Where :
s: the grid shadowing factor.
$r(\lambda)$: the reflectance.
λ: photon wavelength in m.
$f(\lambda)$: the incident photon flux.
$\alpha(\lambda)$:the absorption coefficient.
x: position at which the generation is calculated (the light is incident at x=0).

The absorption coefficient α varies mainly with the type of the semiconductor. In fact, a direct band gap semiconductor absorbs light much faster than an indirect band gap semiconductor. G is integrated on all the photons with energy exceeding the gap energy E_g $\left(\frac{hc}{\lambda} > E_g\right)$. Photons with energy less than the gap energy $\left(\frac{hc}{\lambda} > E_g\right)$are absorbed by conduction band electrons to move to a higher level in the conduction band.

1.4.2 Equivalent circuit of a PV cell

A PV cell is a current source. Its electrical model is described as a current source (I_{SC}) in parallel with two diodes (D1 and D2) and a shunt resistor (R_{sh}). The latter model is mounted in series with a resistor (R_s). The photo-generated current is proportional to the incident irradiance G in $W.m^{-2}$ and to the temperature T in K. The current flowing in the shunt resistor R_{sh} represents leakage current in the edge of the cell. The resistor R_s represents the internal losses of the PV cell caused by the electric contact [1]. The current I flowing in the load will become [2]:

$$I = I_{SC} - I_{01} \times \left(\exp\left(\frac{e \times (V + R_s \times I)}{K_B \times T} \right) - 1 \right) - I_{02} \times \left(\exp\left(\frac{e \times (V + R_s \times I)}{2 \times K_B \times T} \right) - 1 \right) - \frac{V + I \times R_s}{R_{sh}} \tag{1.14}$$

Where I_{SC} is the short-circuit current:

$$I_{SC} = I_{SCN} + I_{SCD} + I_{SCP} \tag{1.15}$$

I_{SCN} : contribution of the n-region in A.
I_{SCD} : contribution of the depletion region in A.
I_{SCP} : contribution of the p-region in A.
I_{01} : the dark saturation current (in neutral region) in A.
I_{02} : the dark saturation current (in depletion region) in A.
R_s : series resistance in Ω.
R_{sh} : shunt resistance in Ω.
V: the output voltage of the cell in V.

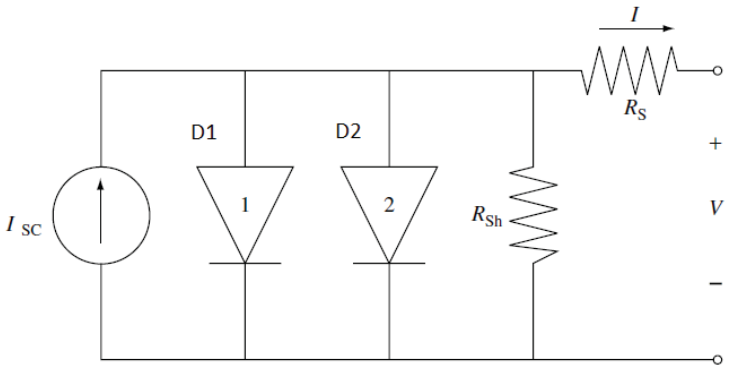

Figure 1.11: Equivalent electric circuit of a PV cell.

$I_{01} \times \left(\exp\left(\frac{q \times (V + R_s \times I)}{K_B \times T} \right) - 1 \right)$ corresponds to the current leaking in the first diode, it represents the recombination occurring in the neutral region. $I_{02} \times \left(\exp\left(\frac{q \times (V + R_s \times I)}{2 \times K_B \times T} \right) - 1 \right)$ corresponds to the current leaking in the second diode, it represents the recombination occurring in the depletion region.

1.4.3 The I-V characteristic

As mentioned before, the output of a PV panel is directly attached to the incident irradiance G. In figure 1.12, we can see the output current as function of the output voltage for different values of G. For a certain incident irradiation, the operating point is defined by the impedance of the load. We can see the linear increase in short circuit current (I_{SC}) with the increase of irradiance and we can see the logarithmic increase of the voltage V_{OC} with the increase of irradiance.

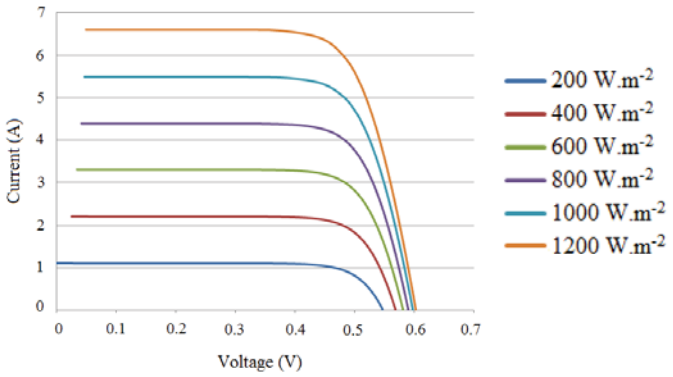

Figure 1.12: I-V characteristic of a cell for different irradiations.

If we neglect the dark saturation current I_{02}, and looked at the I-V characteristic of an ideal diode (see figure 1.9), we can see that the I-V characteristic of a PV cell is the opposite of the diode I-V characteristic. to which we added the short-circuit current I_{SC}.

For each level of the incident irradiation, we define the short-circuit current, I_{SC}, it corresponds to the state where the diodes' current (recombination current) is negligible. The generated current entirely circulates in the external circuit and the voltage is zero. The open circuit voltage, V_{OC}, corresponds to the maximum recombination current passing through the diodes. The MPP (Maximum Power Point) is defined to be the point where the power produced is at its maximal value (V_{MPP}, I_{MPP}). Between all the points on the I-V characteristic the MPP defines with the origin the biggest area rectangle.

For studying the quality and efficiency of a cell we define some ratios:

The FF (Fill Factor) represents the square shape of the I-V characteristic [2]:

$$FF = \frac{I_{MPP} \times V_{MPP}}{I_{SC} \times V_{OC}} = \frac{P_{MPP}}{I_{SC} \times V_{OC}} \tag{1.16}$$

The external collection efficiency is the ratio between I_{SC} and I_{ph}, the maximum current that can be generated if all photons with energy greater than E_g where absorbed [2]:

$$\eta_c^{ext} = \frac{I_{SC}}{I_{ph}} \tag{1.17}$$

Where :

$$I_{ph} = q \times A \times \int f(\lambda)\, d\lambda \tag{1.18}$$

Where :

A: cross section area of the PV cell in cm^2.

$f(\lambda)$: the incident photon flux.

λ: energy of photons, $\lambda \geq Eg$.

1.4.4 Efficiency limits

The efficiency of a photovoltaic cell is defined to be the ratio between the electrical output power and the incident light power. Efficiency is one of the major disadvantages that limit the PV market. The efficiency of single junction solar cells has only reached about 18%. A theoretical efficiency limit of solar cells was studied by William Shockley and Hans Queisser [3]. They demonstrated that the maximum efficiency 44% is observed for a semiconductor with a 1.1 eV band gap. They explain that the optimum efficiency is achieved when the recombination reaches its minimum (balance between photo generation and recombination). The AM 1.5 (Air Mass) normalized to 1000 W.m^{-2} contains

photons with different energies. Only photons with energy greater than the band gap can be absorbed by the semiconductor. The optimum efficiency is obtained when:

- All incident photons with energy greater than the band gap energy are absorbed.
- No net recombination is noted.

In maximum efficiency calculation, the only allowed recombination is the radiative recombination. The photon emitted must be reabsorbed by the semiconductor and must generate an electron-hole pair; it is not assumed to leave the semiconductor. The latter will lead to zero net recombination. According to Shockley and Queisser [3], the efficiency also depends on the temperature of the sun, the temperature of the cell, the band gap. When plotting the efficiency of solar cells in function of the energy band gap we can see that the maximum efficiency is reached with band gap of 1.1eV (see figure 1.13). It is also clear that the efficiency decreases with high and low band gaps. In fact, when the band gap increases, the open circuit voltage increases but the photo generated current decreases. When the band gap decreases, the open circuit voltage decreases but the photo generated current increases. The maximum current voltage product is obtained with a band gap of $1.1eV$.

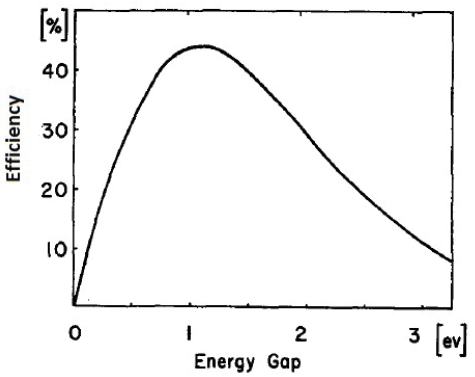

Figure 1.13: Efficiency of solar cell as a function of the band gap [3].

A PV cell is illustrated to be a funnel. The photo generated current is the water poured into the funnel. The water that comes out of the funnel is the current that passes through the load. A valve is implemented on the funnel exit, it represents the load impedance. The funnel is defected; holes are created on its sides. Water coming out of the holes represents the recombination and the collection losses. The water level in the funnel represents the cell voltage. If the valve is opened, the PV cell is in the short circuit state, the load current is high, the recombination and collection losses are low and the cell voltage is null. If the valve is closed, the PV cell is in the open circuit state, the load current is null, the recombination and collection losses are maximal and the cell voltage is high [2].

1.5 Installation and Sizing

To form a PV panel we associate different PV cells in series and in parallel to obtain a certain resultant voltage and current as needed. The output current is then calculated in STC (Standard Test Conditions) $AM1.5$ $G = 1000W.m^{-2}$ and $T = 25^oC$.

The installation of a PV power system is directly affected by the utility. Some installations are autonomous; others are connected to the grid. Some systems supplies water umping motors for rural areas [18, 19]. Some systems connected to the grid can inject power to the grid or can consume electricity from the grid [20]. A net metering device is used to measure the bought and sold energy

between the system and the grid. The balance of system (BOS) is the accessories added to the system to transform PV electricity to useful electricity or to store the energy generated. The BOS is generally constituted of :

- Energy storage (battery).
- A power conditioning device (buck-boost converter, inverter)
- A controller.

The system may also include a backup generator. The PV panels may also be equipped with a sun tracking system to optimize power generation. Systems with a two-axis tracker can increase energy capture by 40%. PV modules are connected to form panels. PV panels are connected to form arrays. The goal of PV modules connection is to multiply the output voltage by the number of series connected modules and to multiply the output current by the number of parallel connected modules. We may note that interconnected modules may present difference in current or voltage which leads to mismatch losses. We also note the possibility of hot-spot formation. This occurs when a module is shaded. In darkness, a PV cell acts as a reverse bias diode; it will dissipate all the produced power. To mitigate hot-spot formation bypass diodes are connected in parallel with modules.

Energy storage is needed in PV systems to support power provision during night and bad weather conditions. The energy storage is generally an electrochemical battery. Lead-Acid batteries are commonly used. Other energy storage systems may be used like mechanical storage systems (water pumping to water storage, artesian well, compressed air) or electromagnetic system (superconducting ring). Power conditioning devices are used to convert electrical energy between the PV panels, the storage and the utility. A buck-boost converter (DC/DC converter) decreases or increases the output voltage to meet charging or utility voltage. An inverter (DC/AC converter) generates power to be used for AC loads or for injecting power in the grid.

The controller is used for handling the electrical energy conversion. It is also implemented for handling the charge and discharge of batteries. A battery must not be overcharged and deeply discharged. The controller is also responsible for delivering indicators and alarms for the end user. The user needs to know the charge state of the battery, the temperature, the irradiance... The controller must also handle hybrid systems. When the minimum discharge level of a battery is reached, the load must be cut off and a diesel generator must be connected to supply the load [21].

When sizing a PV power system, we must take into consideration the daily energy (Bj) need in $Wh.day^{-1}$, the minimum daily generation factor $Hmin$ in $Wh.day^{-1}.m^{-2}$, the number of days of autonomy of the system j (the number of days to power up the system from batteries when there is no sun).

The total capacity of batteries in Ah is given by:

$$C = \frac{Bj \times j}{V_b \times d} \tag{1.19}$$

Where :
V_b: the voltage of the battery in V.
d: the degree of discharge of a battery (50 to 70%).

The needed peak power of the PV panels is:

$$Pc = \frac{Bj}{Hmin \times \eta_{bat} \times \eta_{elec}} \tag{1.20}$$

Where :
η_{bat}: the efficiency of the batteries.
η_{elec}: the efficiency of the other components of the system.

1.6 Types of PV panels

1.6.1 Silicon based PV Panels

Silicon (Si) is the most abundant material of the earth crust after oxygen. Si based PV panels dominate the market [2] and are chosen for our future work because of history processing of Si in electronics, and because the maximum efficiency of PV panels can be reached for a semiconductor having a band gap of 1.1eV [3]. Moreover, most of the research works are done on Si panels, and it is used for power generation.

1.6.1.1 Silicon crystals

Silicon used in PV panels can be divided into different categories according to its crystal organization or grain size. The manufacturing process is responsible in generating different grain size. PV panel efficiency varies with the obtained crystal. Single crystal (or mono-crystal) silicon solar cells are made from the microelectronic industry rejects through the Czochralski process. The grain size of single crystal solar cells is around 15 cm. The Czochralski process is complex and expensive. Single crystal is a high-quality material, it constitutes efficient PV modules (up to 18%) and is stable in electric production. Its lifetime ranges between 20 and 30 years. It is used in aerospace shuttles and home power production [2]. Multi-crystalline (mc-Si) or polycrystalline (pc-Si) or microcrystalline (μc-Si) silicon solar cells are made of lower quality silicon feedstock via less expensive processes (Bridgman and block-casting). The multi-crystalline (1mm), polycrystalline (1μm), and microcrystalline (<1μm) grain size present defects or discontinuations that increase recombination. This limits multi-crystalline or polycrystalline PV panels efficiency (up to 15%). Their lifetime ranges between 20 and 30 years. They are mass produced and cover 50% of the market. They are used in home power production and in power plants. Silicon ribbons solar cells are made via EFG (Edge-defined Film-fed Growth), STR (STring Ribbon), SF (Silicon Film) ... which are characterized by low cost processes. The grain size and the optimum thickness of the cell vary with the manufacturing process.

1.6.1.2 Wafer silicon cells

A silicon crystal cell structure is optimized to reach the following objectives:

- Decrease of incident light reflection.
- Increase of refracted light absorption.
- Decrease of recombination
- Decrease of surface recombination
- Decrease of contact resistance

In figure 1.14, we can find the structure of a PERL (Passivated Emitter and Rear Locally diffused) Cell. This model presents a typical optimization of a cell that responds to the cited objectives. A metallic grid of Silver, Titanium, and Palladium is mounted onto the cell. Its role is to collect electrons generated in the n-type material. The most negative side effects of the grid are shadowing and series resistance increase. If the width of the metallic grid is increased, we obtain a low series resistance but high shadowing. If the width of the metallic grid is decreased, we obtain a high series resistance but low shadowing. A trade off recommends that thin metal fingers are formed with a width of 15 μm [2].

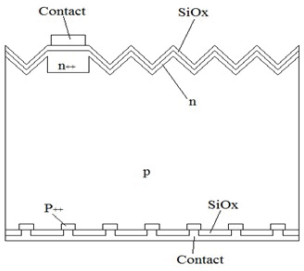

Figure 1.14: Scheme of a Passivated Emitter and Rear Locally diffused.

The exposed surface of the cell is textured in the form of inverted pyramids allowing increase in the refraction of incident light. This mechanism is called light trapping. The side effect of texturing the surface is an increase of the SRV. However, the effective length traversed by the refracted light is multiplied by a factor of:

$$4 \times \left(\frac{n_{Si}}{n_{air}}\right)^2 = 50 \tag{1.21}$$

Where :
n_{Si}: refractive index of silicon (3.48).
n_{air}: refractive index of air (1).

An ARC (Anti Reflective Coating) is added to the surface of the silicon substrate. Without the ARC, 30% of the incident light is reflected to the air because of the high refractive index of the silicon.

1.6.1.3 Thin film Si cells

The main purpose of developing thin film (TF) cells remains in decreasing the total quantity of silicon used. Silicon being an indirect band gap semiconductor, a thick wafer (up to 700µm) is required to absorb the solar spectrum. Raw material used in TF cells may be less pure. At first look, the photocurrent generated by a TF cell will appear to be low. However, with technological enhancement, TF cell of 10µm thickness can reach 10% efficiency. Efficient TF solar cells must complete the following requirements:

- Efficient photo-generation.
- Efficient carrier collection.
- Efficient mechanical support.

Reducing the thickness increases the surface recombination part in total recombination. To mitigate the SRV, surface fields are created and oxide insulator covers the illuminated areas. A superior light trapping technique is applied to TF cells. Both the illuminated surface and the back surface are textured. One side effect of surface texturing resides in the increase of total surface area that increases recombination. A trade off must be taken in consideration. Reflective metal constitutes the back contact to increase effective thickness, but some light is lost by metal absorption. A comparison between a 300µm wafer silicon cell and a 10µm silicon TF cell proves that light absorption is 3 times more important in TF cell. A 10µm TF cell cannot self stand, TF are deposited over a substrate that acts as a mechanical support. Additional enhancements of TF silicon cells can be noted. A back contact made of Aluminum can serve as an impurity-gettering material. Besides, a high grain to thickness ratio presents upper efficiency regarding V_{OC} and FF. In summary, TF solar cells offer:

- A reduction in recombination allowing lower dark current, higher V_{OC}, and higher FF.

- Low quality and low quantity of feedstock.
- Low cost and low energy for fabrication.
- Low cost module.
- Low weight module.
- Flexible solar cells.

1.6.1.4 Amorphous silicon cells

a-Si:H (Hydrogenated Amorphous Silicon) solar cells represent a simple and inexpensive type of solar cells. The properties of amorphous silicon are suitable for photo-generation. A thickness of only 500nm can reach 11% efficiency. As they are less than 1μm thick, a-Si:H cells need a mechanical support. A superstrate or a substrate is used. A superstrate is a transparent plastic or glass layer. The light first propagates through the superstrate before reaching the cell. A substrate is a traditional back support of the cell made of stainless steel. Amorphous silicon is made of unorganized lattice structure of silicon atoms. Hydrogen is added to the crystal. In this way, a percentage of silicon atoms make 3 covalent bounds with Si atoms and one bound with an H atom. When a-Si:H is heated, H atoms are detached leaving one unbounded electron. This is called a dandling bond. This is why the efficiency of amorphous silicon solar modules increases with temperature. a-Si:H solar modules lose 15% to 30% of their efficiency after 1000h of illumination. This is called the Staebler-Wronski Effect (SWE). In fact, the excessive light soaking increases the dandling bonds which increase the recombination rate. Light soaking also damages the PV panel material and the Si network [22]. The general architecture of a pin (p-intrinsic-n) amorphous silicon cell represents a thin p-layer, a relatively thick intrinsic layer, and at the bottom a thin n-layer. Sun light enters from the p-layer which is called the window layer. In amorphous silicon, doping is not efficient, the Fermi energy is not raised and each generated electron is collected by a dandling bond. This is why the p-layer is made with a high band gap to reduce its absorption coefficient and increase the built-in voltage. Efficient photo-generation occurs in the intrinsic layer. As all cells, a-Si:H cells are textured and a back reflector is used to increase the effective thickness of the cell. a-Si:H cells absorb photons with high energy . It means that an a-Si:H solar cell can act as a low pass filter. Instead of wasting low frequency photons, a second a-SI:Ge PV cell is added. The obtained cell is called a multi-junction cell; we can also form an a-Si/a-SiGe/a-SiGe triple-junction cell. The key principle of multi-junction cells is the spectrum splitting. As each cell will absorb a portion of the solar spectrum, the intrinsic layer is thinner than that of single junction cell. A higher voltage is generated with a lower current; a lower voltage drop is then induced. The V_{OC} of the multi-junction cell is the sum of the V_{OC} of each cell. The current is limited by the cell generating the minimum current. The FF is limited by the cell having the smallest FF. To optimize multi-junction cells, the thickness of i-layers and the band gaps must be arranged. We can reach an ideal efficiency of 56% with triple-junction cells to be used under concentrated sun light [2].

a-Si:H based solar cells are used because of their low cost fabrication. They are light, flexible, and resistant to radiation. They are rather used for terrestrial applications and in warm regions because their efficiency increases with temperature. Superstrate cells are integrated in buildings and substrate cells are made for flexible design.

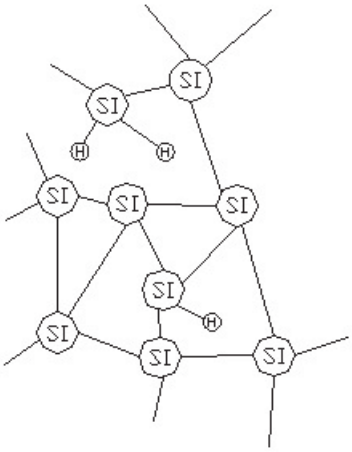

Figure 1.15: a-Si:H crystal.

1.6.2 Multi-junction GaInP/GaAs/Ge cells

When talking about multi-junction GaInP/GaAs/Ge cells (or III-V multi-junction cells) we mean high efficiency high cost solar cells. They are designed to work under concentrated sun (up to 2000 suns). Their efficiency can reach 34% [2].

III and V groups of semiconductor present an attraction for solar application. In fact, many of them are direct band gap semiconductor with a high absorption coefficient. Their energy gap ranges between 1 and 2 eV. In addition N and P doping is simple for III-V semiconductors. Se and Si are examples of n-type dopants. Zn, Mg, and C are examples of p-type dopants.

The key operation of multi-junction solar cells relies on spectrum splitting. The solar spectrum is divided into regions [hνi, hνi+1[and each region is redirected to a dedicated subcell (Egi=hνi). Theoretically, increasing the number of subcells increases the overall efficiency of the cell [23]. To divide the spectrum and redirect the regions to their dedicated subcell, we must simply mount the subcells one onto the other respecting order of band gaps and illuminating first the subcell of the highest band gap. A subcell with a high band gap will act as a low pass filter; it will absorb only photons with high frequency. The next subcell (Egi) will receive a spectrum with photons of maximum energy hνi+1 and will absorb photons of the region [hνi, hνi+1[.Optimum efficiency of multi-junction solar cells relies on band gap matching of subcells.

Each subcell is now considered to act as an independent current source. However, when they are electrically connected in series, they must have the same polarity and the same generated photocurrent. In fact, the cell current will be limited by the smallest photocurrent of the stack. This requires subcells matching. The output voltage of the multi-junction cell is the sum of the voltage of each subcell. Optimum matching of multi-junction cells occurs when subcell have the same I_{MPP}. In this case, the maximum power output of the cell is the sum of all subcells maximum power (I_{MPPi}*V_{MPPi}). Top cell thickness affects current matching. In fact, varying the thickness of the top subcell affects the light transmission to the bottom subcell. And thus an optimum thickness is elaborated when top and bottom photocurrent matches.

In general, high efficiency multi-junction solar cells are used with concentrators because of their high cost. The efficiency of such cells increases when they are illuminated with 100 suns or 1000 suns. In reality, the photocurrent increases and according to the I-V characteristic, V_{OC} increases, thus giving a push to the cell efficiency. Lattice matching is also important when dealing with multi-junction solar cells. Ge is used as substrate in multi-junction GaInP/GaAs/Ge cells. Its lattice constant is close to that of Ga/As, it is rigid, I_{SC} of Ge subcell is higher than that of the GaAs. One last difficulty in

multi-junction design is the interface between subcells called the TJIC (Tunnel-Junction Interconnect). As first approach, the polarity of a TJIC is opposite of that of the PN junction, which will reduce V_{OC}. In reality, the TJIC is made of a tunnel junction or a narrow heavily doped P and N regions. A tunnel junction will act as a resistor for current values not exceeding the peak tunneling current. In summary, III-V solar cells are expensive for one sun use. They are commonly used with concentrators and in spacecrafts [24] . They enjoy a high V_{OC} and a low I_{SC}, an excellent radiation resistance, and a small temperature coefficient. Their temperature may increase under concentrate sun which require intervention and control for cooling.

1.6.3 Cu(InGa)Se_2 cells

Cu(InGa)Se2 solar cells power small equipments like calculators. Their fabrication is costly. Their surface is of the order of 0.5cm^2. They have a high radiation resistance, they are light, and can be made flexible. Their efficiency can reach 18.8%.

The Cu(InGa)Se_2 composition can vary in function of In and Ga concentration. This concentration affects the band gap of the p-type Cu(InGa)Se_2 material. The maximum efficiency is obtained with a band gap of 1.12eV. Cu(InGa)Se_2 is a direct band gap semiconductor with high absorption coefficient. Its grain boundaries do not increase the surface recombination.

A Cu(InGa)Se_2 solar cell is formed over a soda-lime glass. Then a molybdenum (Mo) layer is added acting as a back contact. The Cu(InGa)Se_2 layer is then deposited. The PN junction is formed by adding a thin layer of CdS. A heavily doped ZnO layer and an intrinsic layer of ZnO are deposited to the stack. At the end a metallic grid is added for collection [2].

The defects between p-type (Cu(InGa)Se_2) and n-type (CdS) lattice structures do not affect the behavior of the cell or reduce V_{OC}. The role of the ZnO layer is to minimize the defects of Cu in the PN junction interface [2]. The substrate (soda-lime glass) is suited to Cu(InGa)Se_2. In fact, the thermal expansion coefficients of the two materials are similar ($9x10^{-6}K^{-1}$). After deposition, the temperature decreases of about 500^oC. Soda-lime glass is also chemically suited for Cu(InGa)Se_2.

The absorption coefficient of Cu(InGa)Se_2 is high and the open circuit increases when the band gap is increased. The device losses can be enumerated:

- Optical losses (Shading and reflection).
- Recombination losses.
- Resistive losses.
- Light absorption in ZnO and in CdS (electrons and holes in the CdS region are not collected).
- Incomplete absorption and collection in the Cu(InGa)Se_2 layer

Cu(InGa)Se_2 fabrication is delicate; Cd is a cancer causing element. It is recommended, because of environmental and health concerns, that PV panels becomes Cd-free. When talking about materials availability, In is the least available material. This causes mandatory recycling of Cu(InGa)Se_2 modules [11].

1.6.4 CdTe cells

CdTe alloy is suited for solar spectrum. With a direct band gap (Eg=1.5eV) and a high absorption coefficient, CdTe can absorb 99% of photons ($h\nu > 1.5eV$) with a 2 µm of thickness. CdTe PV panels present only 10% efficiency and need pollutant materials as Cd. They are typically used for small appliances like calculators. CdTe cells can also be used in space power generation, infrared detection, gamma radiation detection, and thermal imaging.

Cd excess in CdTe provides n-type material and Te excess in CdTe provides p-type material. CdTe solar cells are made with substrate or superstrate structure. The superstrate structure is the most dominant. A TCO (Transparent Conductive Oxide) and a high resistance oxide layer are deposited.

Then a thin layer of CdS is deposited acting as an n-region. Then the CdTe layer acts as a p-region. At the end a contact is made to collect the carriers [2].

The CdS layer is thin to permit photons to reach the CdTe layer and produce higher photocurrent. The back contact is made of two layers. The layer attached to CdTe is enriched with Te and Cu to form a heavy p-region. The second layer is a normal metal contact.

The poor efficiency of CdTe solar cells and their cancer causing material Cd mark some disadvantage of this technology. However, CdTe present the best market price inducing low payback time. This emphasizes the interest they can give for enhancement of their life time by use of the new control and diagnosis technologies.

1.6.5 Dye-sensitized cells

Dye-Sensitized Solar Cells (DSSC) are Photoelectrochemical cells. They are fundamentally an oxide semiconductor immersed in an electrolyte. Their efficiency can reach 10%. They have low cost fabrication and need low cost materials. They can be made transparent or colorful they can be used as window glass. They are not pollutant and easily recyclable.

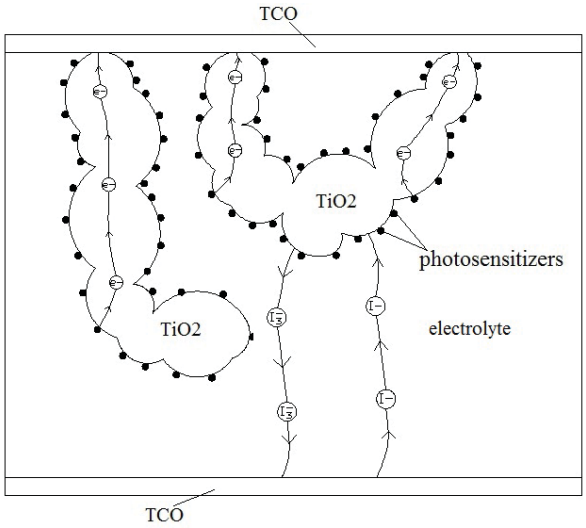

Figure 1.16: Structure of a DSSC.

Dye-sensitized solar cells are first encapsulated by two TCO layers that form the front and back contacts. SnO_2 is typically used as TCO. A thin film of TiO_2 is deposed near the front contact. The thickness is about 10 µm with nanoparticles of 10-30 nm. This structure yields a high porosity and a high effective surface compared to the apparent surface. The TiO_2 film will be immersed in an electrolyte containing I^- and I_3^- ions. Complex structures of photosensitizers will be attached on the large surface of the TiO2. The stack must be sealed to prevent leakage and evaporation.

Photosensitizers at their ground state (S) will absorb light and become in the excited state (S^*). Then they will release an electron in the TiO_2 electrode [2].

$$S + h\nu \rightarrow S^* \tag{1.22}$$

$$S^* \rightarrow S^+ + e^- \tag{1.23}$$

The electrons will be transported via the TiO_2 to the front contact. They will pass through the load and reach the back contact. I_3^- will receive electrons at the back contact and generate I^-. S^+will gain an electron from I^- to become in the ground state and generate I_3^-.

$$I_3^- + 2e^- \rightarrow 3I^- \tag{1.24}$$

$$S^+ + e^- \rightarrow S \tag{1.25}$$

No recombination is noted in DSSC. In fact, electrons are conducted by the TiO_2 crystal and no holes are formed in the valence band. But a recombination dark current is noted when I_3^- receives electrons at the level of TiO_2. To reduce the dark current, TBP (*tert*-butylpyridine) is used on the TiO_2 surface. Voltage is then increased but current is decreased.

Even their low cost fabrication and low cost row materials, DSSC need some improvements to become commercialized like efficiency improvement, stability for outdoor use, and solid electrolyte. The latter discouraged us in searching for increasing their life span.

1.6.6 Organic cells

Organic solar cells are formed with polymers. Polymers have conjugated systems. In conjugated systems, atoms bonds by alternating single and multiple bonds. π bonds and π* bonds are formed. π bonds corresponds to the HOMO (Highest Occupied Molecular Orbital) and π* bonds corresponds to LUMO (Lowest Unoccupied Molecular Orbital). The energy gap between the HOMO and the LUMO is defined to be the band gap. The band gap of organic cells is generally greater than 1.8eV.

Many architecture types of organic cells can be noted. The single layer photovoltaic cell or Pochettino cell is made of an organic layer sandwiched between two electrodes the LWFE (Large Work Function Electrode) and the SWFE (Small Work Function Electrode). The LWFE corresponds to the positive electrode it collects holes and the SWFE corresponds to the negative electrode it collects electrons. A schottky junction is formed near the SWFE where excitons are dissociated into electron and holes figure 1.17. The second architecture type of an organic cell is the double layer donor/acceptor Heterojunction. A donor and an acceptor organic layers are mounted between two electrodes. A donor/acceptor interface is formed. Electrons and holes are more likely to be collected because they move in different layers. A third architecture type of organic cells is the bulk heterojunction organic cell. Acceptors and donors are randomly distributed in the bulk creating thus delocalized donor/acceptor interfaces.

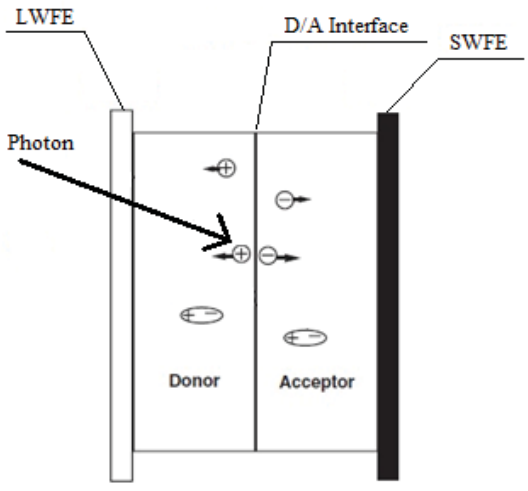

Figure 1.17: Organic bilayer cell.

When a photon with energy equal to the energy of the band gap excites an organic polymer, an electron is transferred from the HOMO to the LUMO. Organic cells are made using thin films which decrease the amount of light absorption. After that the exciton is formed, it will diffuse to the donor/acceptor interface, the average exciton diffusion length is between 5 and 50 nm. In order to increase the average exciton diffusion length, materials must be defect-free and a large donor/acceptor interface must be built. Once an exciton reaches the donor/acceptor interface, charge carriers (electrons and holes) will dissociate and will start diffusing to the corresponding electrode. The driving force of the charge carriers is generally due to the work function difference between the electrodes. At the end charge carriers will be collected. It is proposed for ideal contact resistance that the acceptor LUMO level matches the SWFE Fermi level and that the donor HOMO level matches the LWFE Fermi level.

Organic solar cells present many advantages: lightweight, flexible, low fabrication cost, integration in decoration, and continuous variation of band gap. They also present disadvantages: low efficiency, low durability, and low stability. The latter discouraged us in searching for increasing their life span.

1.7 Maximum Power Point Tracking

In this section, we discuss the MPPT algorithms that are a control topic associated to RES, especially PV panels. We start by expressing the need of MPPT in PV panels. Then we will survey existing MPPT algorithms and we compare these techniques based on their convergence, robustness, oscillation, and simplicity of implementation.

This work was developed in parallel to our PhD studies. The gain of the work is in strengthening the understanding of operation of PV panels and will be used in chapter 5.

1.7.1 Problem statement

The P-V curve of PV panels presents a nonlinear mountain shape. The curve has generally a MPP. In some mismatch cases we can see a multimodal shape of the curve where we can note a global maxima and local maximas as shown in figure 1.18. The objective of any MPPT algorithm is to extract the maximum power from a PV panel by changing the impedance of the load seen by the panel. A DC/DC converter is used with a variable duty cycle. The main problem relies that the MPP in the P-V curve varies dynamically with irradiance and temperature as shown in figures 1.19 and 1.20. Besides, for the same irradiance and temperature, the operating voltage of the MPP varies with change in the equivalent circuit of the PV panel as shown in figure 1.21. The equivalent circuit of the panel varies due to the degradation process.

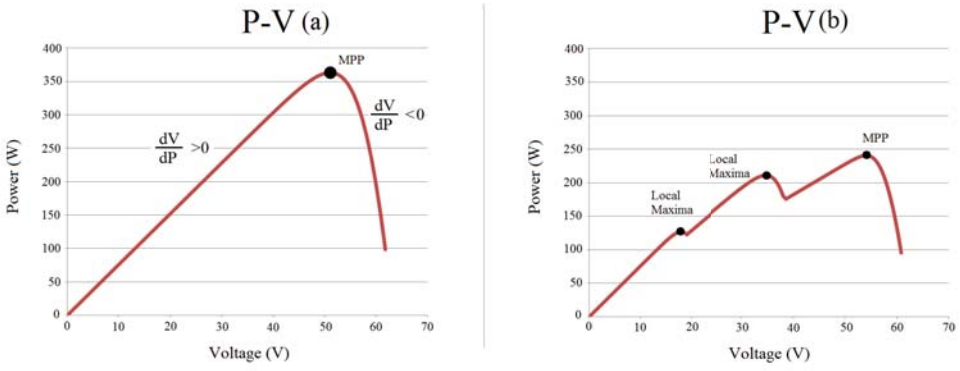

Figure 1.18: P-V curve of a PV system in STC conditions (a) and in partial shading (b).

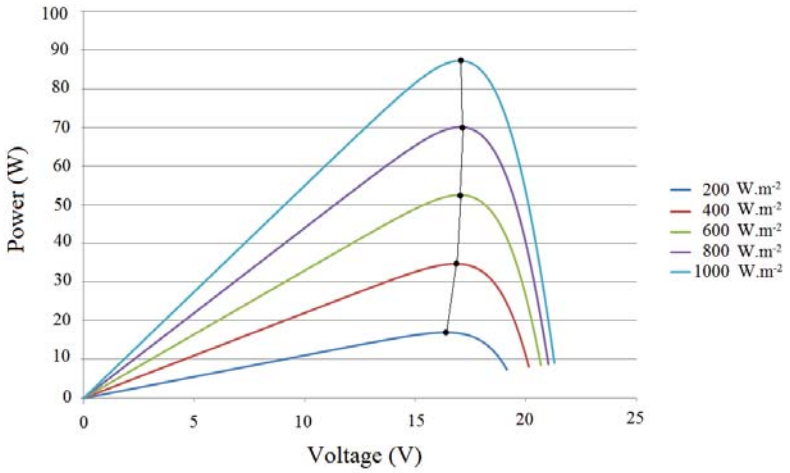

Figure 1.19: Variation of the voltage of the MPP as a function of irradiance change.

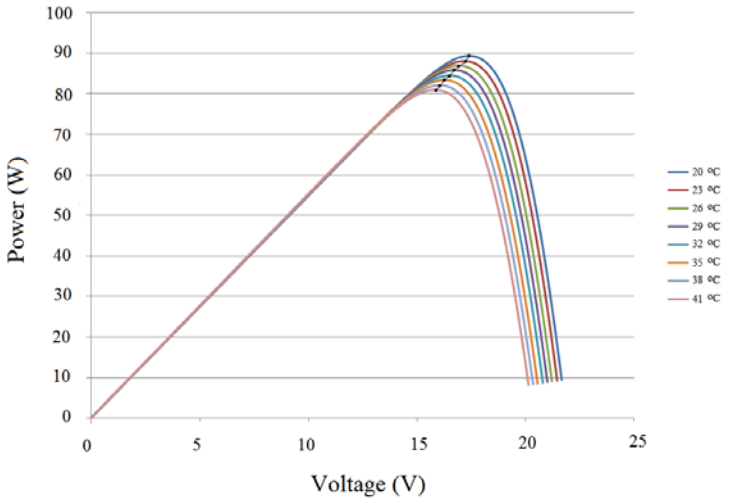

Figure 1.20: Variation of the voltage of the MPP as a function of temperature change.

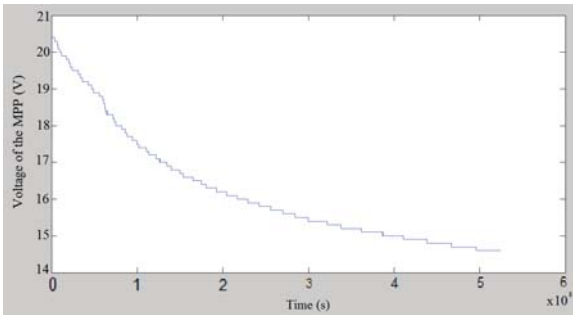

Figure 1.21: Variation of the MPP voltage as a function of time.

1.7.1.1 DC/DC converter

In order to understand the operation of the DC/DC converter in varying the impedance seen by the PV panel, we develop a state model of a buck-boost converter based on the averaging technique.

Figure 1.22 shows the principal diagram of a buck-boost converter. The switch is driven by a PWM (Pulse Width Modulation) signal with a duty cycle s. When the switch is closed (SW=1) we can write the following relations:

$$\begin{cases} I_{in} = I_L \\ V_{in} = L\frac{dI_L}{dt} \\ C\frac{dV_{out}}{dt} = -I_{out} \end{cases} \Rightarrow \begin{cases} I_L = I_{in} \\ \frac{dI_L}{dt} = \frac{V_{in}}{L} \\ \frac{dV_{out}}{dt} = \frac{-I_{out}}{C} \end{cases}$$

Where:
I_{in}: input current in A.
I_L: Current passing through inductor in A.
V_{in}: input voltage in V.
L: Inductance in H.
C: Capacitance in F.
V_{out}: output voltage in V.
I_{out}: output current in A.

When the switch is opened (SW=0) we can write the following relations:

$$\begin{cases} V_{out} = L\frac{dI_L}{dt} \\ C\frac{dV_{out}}{dt} = -I_L - I_{out} \end{cases} \Rightarrow \begin{cases} \frac{dI_L}{dt} = \frac{V_{out}}{L} \\ \frac{dV_{out}}{dt} = \frac{-I_L - I_{out}}{C} \end{cases}$$

Applying the averaging technique, the averaged state equations become:

$$\bar{I_L} = s \times \bar{I_{in}} \tag{1.26}$$

$$\frac{d\bar{I_L}}{dt} = \frac{s \times \bar{V_{in}} + (1-s) \times \bar{V_{out}}}{L} \tag{1.27}$$

$$\frac{d\bar{V_{out}}}{dt} = \frac{-\bar{I_{out}} - (1-s) \times \bar{I_L}}{C} = \frac{-s \times \bar{I_{out}} - (1-s) \times \bar{I_{in}}}{s \times C} \tag{1.28}$$

Where, $\bar{x}$ is the averaged variable of the variable x.

The DC/DC converter will always generate DC values during steady state. The AC or variable terms in V_{in}, V_{out}, I_{in}, and I_{out} are negligible and small comparing to the DC variables. We can assume that

$$\frac{d\bar{I_L}}{dt} = \frac{s \times \bar{V_{in}} + (1-s) \times \bar{V_{out}}}{L} = 0 \tag{1.29}$$

$$\frac{d\bar{V_{out}}}{dt} = \frac{-s \times \bar{I_{out}} - (1-s) \times \bar{I_{in}}}{s \times C} = 0 \tag{1.30}$$

therefore:

$$s \times V_{in} + (1-s) \times V_{out} = 0 \tag{1.31}$$

$$V_{out} = \frac{-s \times V_{in}}{1-s} \tag{1.32}$$

$$-s \times I_{out} - (1-s) \times I_{in} = 0 \tag{1.33}$$

$$I_{out} = \frac{(1-s) \times I_{in}}{s} \tag{1.34}$$

From equations 1.32 and 1.34 we can see the relations between input and output voltage, and between the input and output current. The input power and the output power are equal ($P_{out} = V_{out} \times I_{out} = \frac{-s \times V_{in}}{1-s} \times \frac{(1-s) \times I_{in}}{s} = -V_{in} \times I_{in} = -P_{in}$). The DC/DC converter changes the representation of power by changing the current and voltage in an inversely proportional way. The ratio between voltage and current varies which changes the impedance seen by the PV panel.

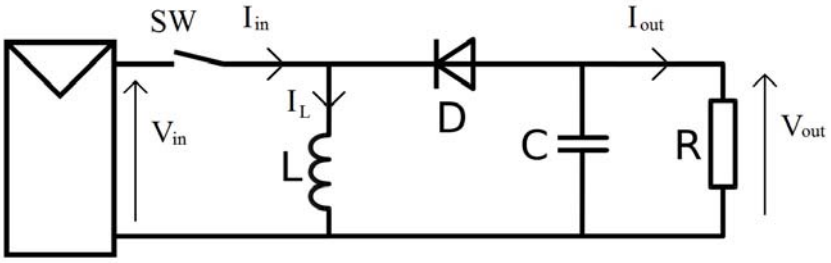

Figure 1.22: Principal diagram of a buck boost converter.

1.7.2 MPPT algorithms

1.7.2.1 Open-loop algorithms

These methods are based on estimation of the voltage of the MPP. They mainly use artificial intelligence like ANN (Artificial Neural Networks) and FLC (Fuzzy Logic Controllers). ANN MPPT control is achieved by training an ANN having as input the irradiance and the temperature and as output the reference voltage of the MPP. During control, the reference voltage (V_{MPP}) is generated from the ANN based on the weather conditions, the duty cycle is adjusted in order to reach the reference voltage [25]. Others use V_{OC} as the input to the ANN. The output is also the reference voltage of the MPP [26]. FLC algorithms use generally two inputs (a value and its variation) e.g. $\frac{\Delta P}{\Delta I}$ and the variation of $\frac{\Delta P}{\Delta I}$. The FLC will generate the duty ratio of the DC/DC converter [27]. Others take the irradiance and temperature as inputs to the FLC and generate the duty cycle [28].

Some methods are based on the approximation that the ratio between the reference voltage of the MPP (V_{MPP}) and the open circuit voltage (V_{OC}) is constant. In this case the controller measures periodically the V_{OC} and adjusts the value of the operating voltage. The ratio between V_{MPP} and V_{OC} ranges between 0.73 and 0.8. The same method can be applied by approximating the ratio between the MPP current (I_{MPP}) and the short circuit current (I_{SC}); this ratio is constant. The ratio between I_{MPP} and I_{SC} ranges between 0.8 and 0.9 [26].

The above mentioned algorithms present low performance comparing to closed loop algorithms. In fact, the open loop algorithms are based on training of ANN that cannot be generalized to all types, sizes, and manufacturers of PV panels. Other open loop algorithms are based on approximations. The main limitation of open loop algorithms remains in the fact that the equivalent circuit of the PV panels changes with time. The latter will lead to changes in the reference voltage of the MPP (see figure 1.21).

1.7.2.2 Closed-loop algorithms

Closed-loop algorithms for MPPT are also known as online methods or model free methods. They use a feedback value of voltage or current to generate the control signal of the system. They present more precise tracking than open loop algorithms. In fact, open loop algorithms do not take into consideration the variation of the PV panel model with time; figure 1.21 shows that the MPP voltage, for STC, varies with time because of the degradation process of the panel.

Perturb and Observe algorithm The most used algorithm is the PO (Perturb and Observe). The PO algorithm is based on the facts that: $\frac{dP}{dV} = 0$ when the system operates at the MPP, $\frac{dP}{dV} > 0$ when the system operates at the left of the MPP, and $\frac{dP}{dV} < 0$ when the system operates at the right of the MPP (see figure 1.18). The algorithm always checks the sign of $\frac{\triangle P}{\triangle V}$ (in discrete mode) and generates the new value of the reference voltage until it reaches the MPP. If the change in reference voltage (V_{ref}) increases the power, the same change will be applied in the next iteration, otherwise an opposite change will be applied to V_{ref}. Figure 1.23 shows the flowchart of the PO algorithm [4, 26]. The reference voltage is given by the following formula:

$$V_{ref}(k+1) = V_{ref}(k) + \alpha \times sign(\triangle V) \times sign(\triangle P) \tag{1.35}$$

Where:
α: is the step size of the reference voltage in V.
sign: is a function returning the sign of the value.

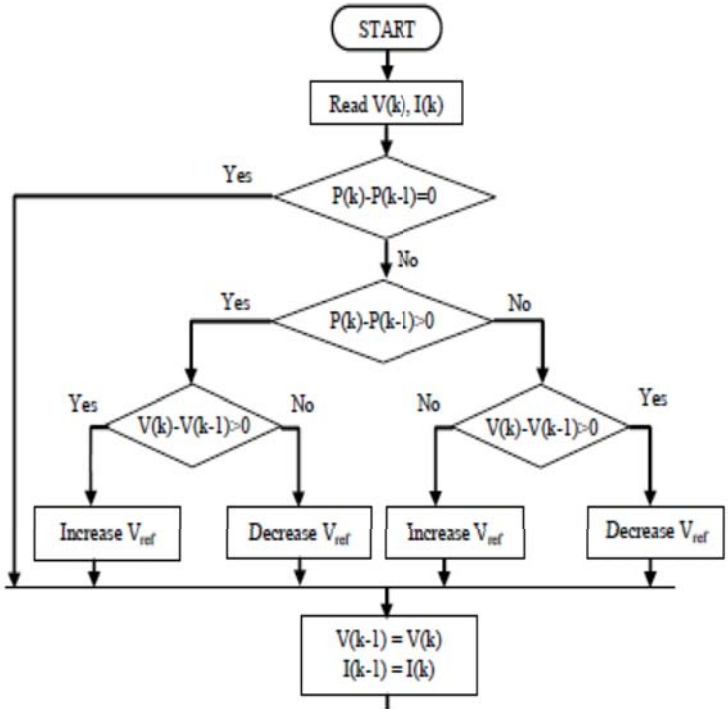

Figure 1.23: Flowchart of the PO algorithm.

Incremental Conductance algorithm The IncCond (Incremental Conductance) algorithm uses the same fact of the PO algorithm where always the slope of the power curve is always equal to zero at the MPP $\left(\frac{dP}{dV} = 0\right)$, it is negative at the right of the MPP $\left(\frac{dP}{dV} < 0\right)$, and it is positive at the left of the MPP $\left(\frac{dP}{dV} > 0\right)$.

$$\frac{dP}{dV} = \frac{d(V \times I)}{dV} = I\frac{dV}{dV} + V\frac{dI}{dV} = I + V\frac{dI}{dV} \tag{1.36}$$

We define the PV conductance by:

$$G = \frac{dI}{dV} \tag{1.37}$$

In order to track the MPP we must always direct the operating voltage to the point where we find that $\frac{\triangle P}{\triangle V} = 0$ otherwise $G = \frac{dI}{dV} = -\frac{I}{V}$. At each iteration the algorithm will test if $G < -\frac{I}{V}$ or $G > -\frac{I}{V}$. If $G < -\frac{I}{V}$ otherwise $\frac{\triangle P}{\triangle V} < 0$, the panel operates at the right of the MPP, the voltage must be reduced. If $G > -\frac{I}{V}$ otherwise $\frac{\triangle P}{\triangle V} > 0$, the panel operates at the left of the MPP, the voltage must be increased. Once at the MPP, the system will check for a change in the current that is related to a change in weather conditions. Figure 1.24 shows the flowchart of the IncCond algorithm [26, 4].

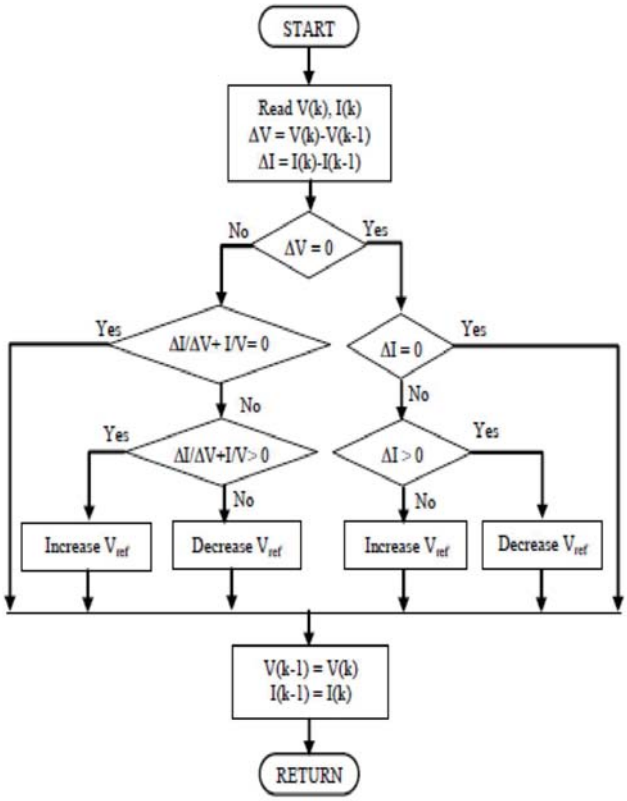

Figure 1.24: Flowchart of the IncCond algorithm [4].

Hill Climbing algorithm The HC (Hill Climbing) algorithm uses the same fact as the two above mentioned algorithms. The slope at the left of the MPP is positive and it is negative at its right. The only difference is that the HC acts directly on the duty cycle. However, PO and IncCond act on the reference voltage. Figure 1.25 shows the comparison between HC and PO [4, 29].

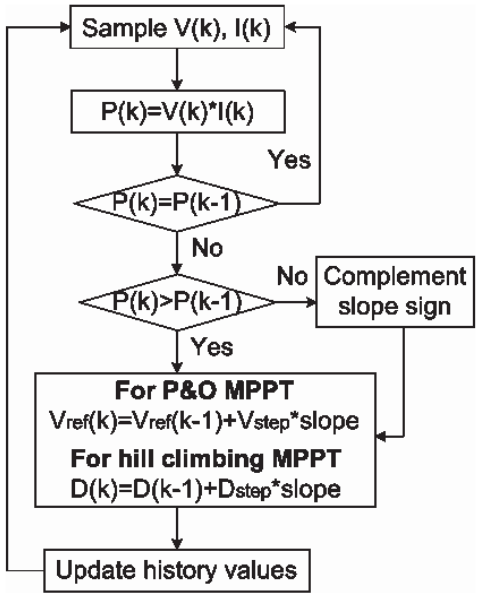

Figure 1.25: Flowchart of the HC algorithm.

Extremum Seeking Control algorithm The ESC (Extremum Seeking Control) algorithm studies the gradient of the P-V curve. The algorithm always uses the fact that the slope at the left of the MPP is positive and it is negative at its right. The ESC algorithm takes also into consideration the amplitude of the slope. In fact, the more the operating point is close to the MPP, the less is the amplitude of the derivative. The algorithm will move the operating point towards the MPP faster in the regions far from the MPP. When the operating point reaches the MPP region, the tuning becomes finer [5].

In order to calculate the gradient, a sine wave $(u_0 \times sin\,(w_o t))$clear is added to the input of the system; V_{ref}. The power output is multiplied by the same sine wave. The resultant signal is filtered via a low-pass filter. The output of the filter is then added to the reference voltage V_{ref}. Figure 1.26 shows the block diagram of ESC algorithm.

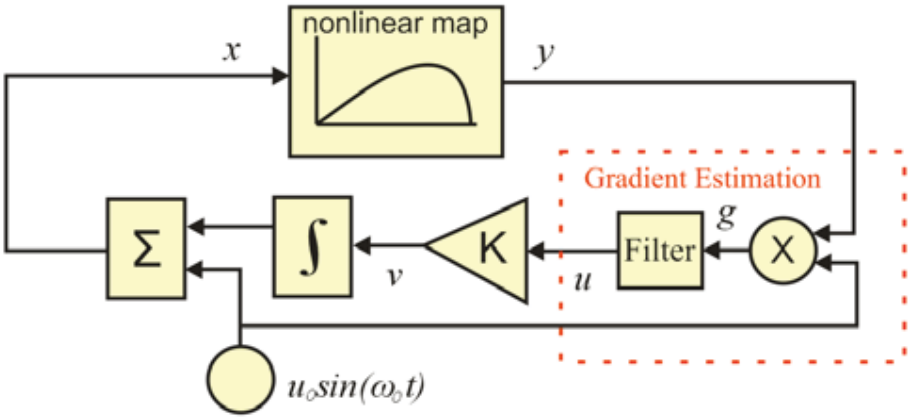

Figure 1.26: Block Diagram of ESC algorithm [5].

One variant of the method is developed in [5], the authors uses the hessian of the P-V curve in the calculation of the new reference voltage. The hessian or the second derivative gives also an information about the slope of the curve. The method is called NL-ESC (Newton Like Extremum Seeking Control).

Another variant of the method is developed in [30], the authors uses the ESC to track the global MPP. Their method shows effectiveness in cases where the power curve presents multiple maximums. The latter occurs during partial shading or mismatch faults. In order to leave a local maxima, the amplitude of the sine wave (u_0) is increased for a small period. This is called an amplitude modulation of the perturbation signal. This amplitude modulation leads to high oscillation at the operating point around the local MPP. The system can now leave the local MPP and catch another higher MPP.

Modified Enhanced PO algorithm The MEPO (Modified Enhanced Perturb and Observe) algorithm is an enhancement of the PO algorithm. In PO the step size of the variation of the reference voltage is constant. However, in the MEPO, the step size is adjusted proportionally to the variation of power caused by the last adjustment of the reference voltage. The reference voltage is given by formula 1.38, the flowchart is shown in figure 1.27.

$$V_{ref}(k+1) = V_{ref}(k) + K \times \alpha \times \triangle P \times sign(\triangle V) \tag{1.38}$$

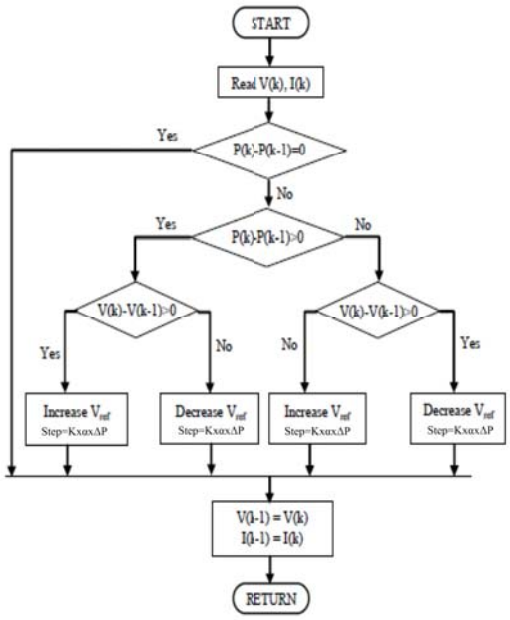

Figure 1.27: Flowchart of the MEPO algorithm.

Robust Sliding Mode Control Algorithm The RSMCA (Robust Sliding Mode Control Algorithm) uses the fact that the MPP is reached when $\frac{dP}{dV} = 0$. The RSMCA also takes into consideration the variation of irradiance and temperature as function of time; we can write $P(t) = f(V, I, t)$. In the RSMCA we define two control inputs: the variation of reference voltage $u1 = \triangle V_{ref}$ and the variation of the reference current $u2 = \triangle I_{ref}$. $u1$ and $u2$ can be used simultaneously, alternatively or one can be frozen to 0. The objective is to reach P_{max} the maximum power that can be extracted from the panel. A Lyapunov function can be defined by [4]:

$$W(t) = P_{max}^2 - P(t)^2 \tag{1.39}$$

$W(t)$ will always be negative unless at the MPP where it reaches 0. The objective becomes now to decrease $W(t)$ with time; otherwise try to keep $\dot{W} = \frac{dW}{dt} = -2 \times P(t) \times \frac{dP}{dt} < 0$. The sign of $\dot{W}$ is given by $-\frac{dP}{dt}$ because $P(t)$ is always positive.

$$-\frac{dP}{dt} = -\left(I\frac{dV}{dt} + V\frac{dI}{dt}\right) \tag{1.40}$$

In discrete mode the sign of $\dot{W}$ is given by:

$$Sg = -(I \times \triangle V + V \times \triangle I) \tag{1.41}$$

If $u2$ is frozen to zero and $u1$ is set to $u1 = K \times \alpha \times \triangle P \times sign(\triangle V)$.

$$\begin{aligned} Sg &= -\left(I \times K \times \alpha \times \triangle P \times sign(\triangle V) + V \times 0\right) \\ Sg &= -\left(I \times K \times \alpha \times (I \times \triangle V + V \times \triangle I) \times sign(\triangle V)\right) \\ Sg &= -\left(I^2 \times K \times \alpha \times \triangle V \times sign(\triangle V)\right) \end{aligned} \tag{1.42}$$

As K and α are positive constants, Sg will always be positive and the Lyapunov function will always decrease. The latter proves the conversion of the MEPO algorithm [4].

1.7.3 Comparison of MPPT algorithms

1.7.3.1 Qualitative comparison

In this paragraph, we present a qualitative comparison between MPPT algorithms. The open-loop methods present simple implementations. But they present inaccuracy when the PV panel is subject to degradation. The latter is shown in figure 1.21 where the voltage of the MPP (V_{MPP}) changes significantly for a PV panel as function of time. Some open-loop algorithms need additional sensors like solar irradiance and temperature. The latters need calibration and maintenance.

The closed-loop control algorithms present more accuracy, robustness, and less sensitivity. The PO algorithm presents the simplest implementation. However, the step size is constant which leads to oscillations around the MPP. The HC presents the same situation. When we look at the MEPO and the RSMCA we can see a more adaptive algorithm. The step size is increased when the operating point is far from the MPP. The step size is decreased when the operating point becomes close to the MPP. This adaptation will lead to a higher conversion speed and lower oscillation at the MPP. The ESC presents high complexity in implementation. However, it presents high conversion speed and capability to leave a local maximum and reach the global MPP.

1.7.3.2 Quantitative comparison

In this section we present a simulation based on a comparison between different MPPT algorithms. Five algorithms are compared: the classical PO, the MEPO, the IncCnd, the RSMCA, and the NL-ESC.

The simulation system built under Psim software is composed of a PV panel, a DC/DC converter, and a load. The physical model of PV panels is used in Psim. The PV panel is composed of 36 cells mounted in series. The panel can deliver a short circuit current of 5.5 A and can generate 140W in STC. The DC/DC converter is a boost (step up converter) mainly constituted of a capacitor, a self, a diode, and a switching device.

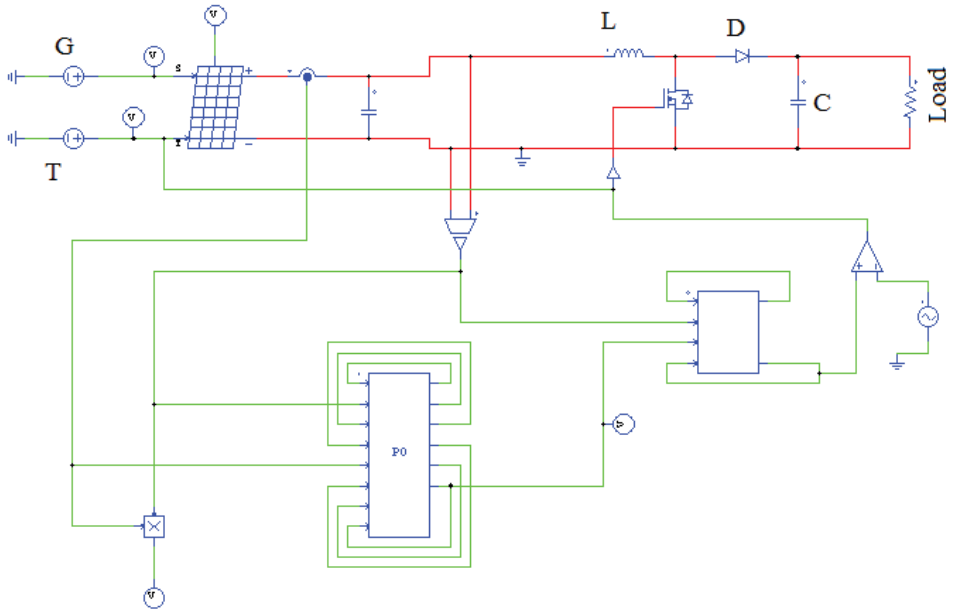

Figure 1.28: Circuit diagram of a PV panel and boost converter Controlled by a MPPT algorithm.

In order to compare the 5 algorithms we built 5 identical PV simulation systems (see figure 1.29). All PV panels are subject to the same irradiance and temperature inputs. The power generated by each system is monitored.

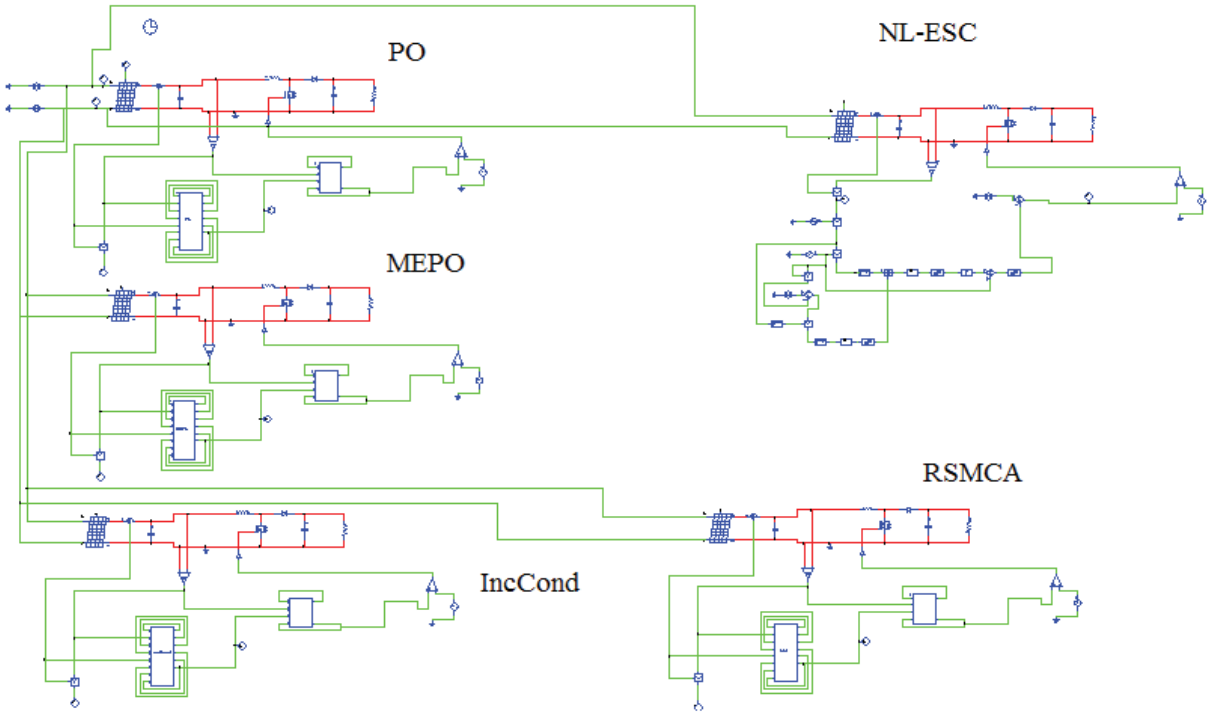

Figure 1.29: Circuit of all the MPPT algorithms.

Table 1.1: MPPT Simulation Parameters.

Parameter	Description	Value
L	Self of the DC/DC converter	$100\mu H$
C	Capacitor of the DC/DC converter	$1mF$
$Load$	Resistor	100Ω
α	Step of the PO	$0.1V$
k	Gain of MEPO	25
α	Step of the IncCond	$0.1V$
k	Gain of the RSMCA	25
K	Gain of the gradient of the NLESC	0.15
K_h	Gain of the hessian of the NLESC	3000
u_0	Amplitude of the sine wave of the NLESC	0.01
ω_0	Pulsation of the sine wave of the NLESC	$100 \times \pi$

Zero order hold interpolation We perform many simulations with varying irradiance and temperature. The values are not interpolated causing sudden variation in power output. This is called zero order hold interpolation.

For the first simulation, we consider an irradiance of $1000W.m^{-2}$ and a temperature of 25^oC (STC). The simulation result is presented in figure 1.30. We can see that all the algorithms reach the maximum power point in less than 0.5 seconds. The NL-ESC presents the less oscillations. The RSMCA is the fastest with decreasing oscillations. Also the MEPO present the same features. The IncCnd and PO present high oscillation and take time to reach the MPP.

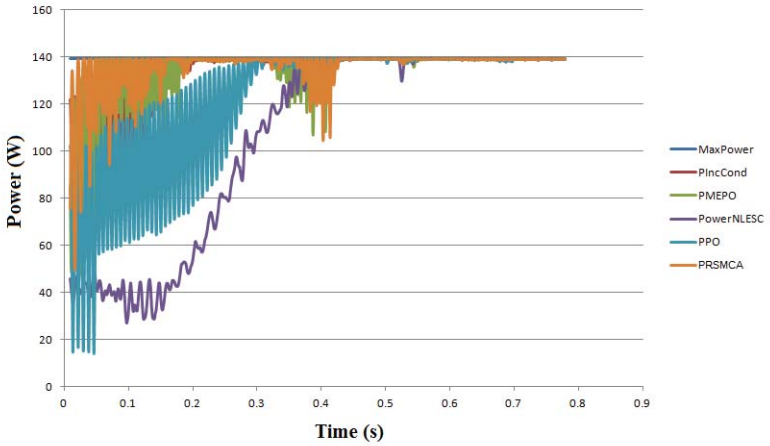

Figure 1.30: Comparison simulation for all MPPT algorithms in STC.

For the second simulation, we consider a zero order sample and hold for the irradiance and temperature that change. The irradiance and temperature rise and fall brutally as shown in figure 1.31. The simulation of figure 1.32 shows how all algorithms manage to reach the MPP after the brutal variation of environmental conditions. The NL-ESC presents the highest oscillation amplitude after the brutal change. The RUCA and MEPO presents oscillation before stabilizing in the MPP after the brutal

change. This is explained because these last algorithms use the power gradient to calculate the step, and after brutal change of environmental conditions, the power gradient is high.

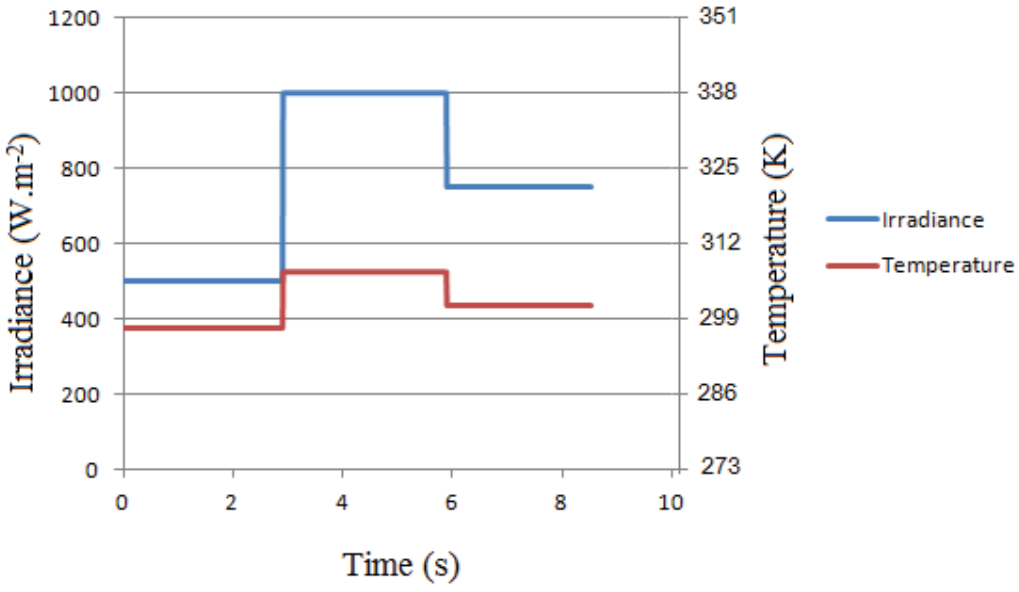

Figure 1.31: Brutal change in irradiance and temperature.

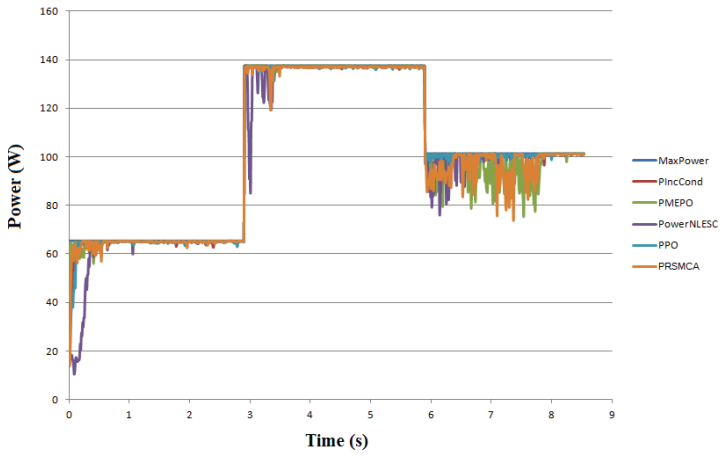

Figure 1.32: Comparison simulation for brutal change in irradiance and temperature.

In order to compare the MPPT algorithms we varied the frequency of the algorithms. We mean by the frequency of the algorithm how many times the reference voltage (V_{ref}) has been calculated per second. For high MPPT algorithm frequencies (25Hz, 50Hz, 100Hz) no difference in power output is noted between the four algorithms. We can see in figure 1.33 the variation of irradiance and temperature in the first upper graphs, the power is shown in the bottom graph. After a change in environmental conditions that make an increase in power output, MEPO algorithm may present an oscillation because it is based on the power gradient. At high irradiances, the RSMCA algorithm present oscillation caused by the gain in calculation of V_{ref}.

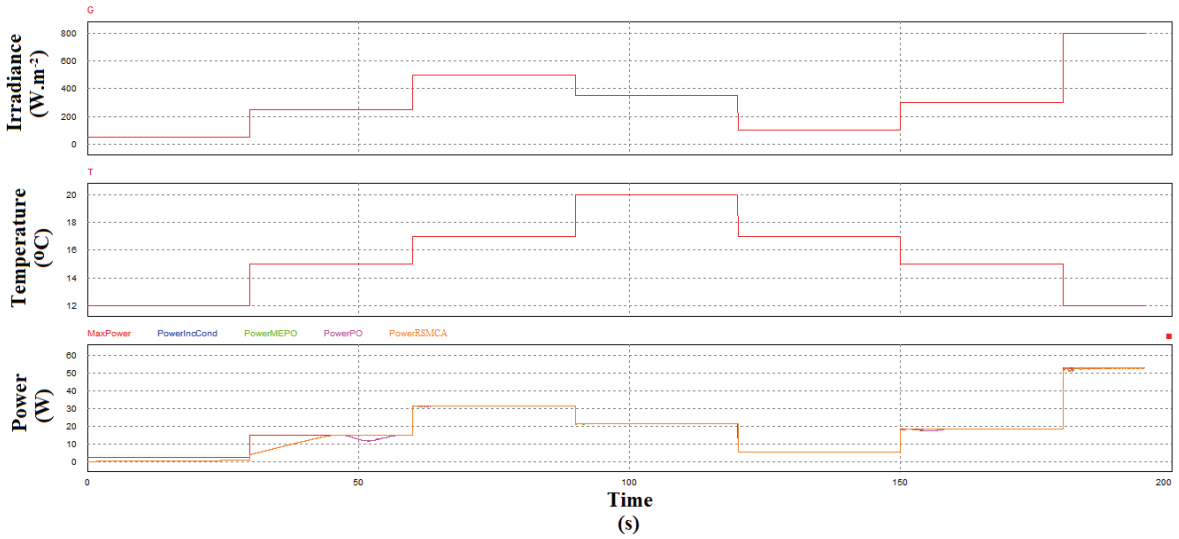

Figure 1.33: Comparison simulation of brutal change in irradiance and temperaure with high algorithm frequency (100Hz).

For low frequencies (5Hz, 10Hz, 12.5Hz), the MEPO and the RSMCA algorithms excel the PO and IncCond algorithms. We can see in figure 1.34 that the PO power and the IncCond power are too far from the maximum power that can be generated from the panel. This is due to the fixed or small step size of the V_{ref}. We must recall that the MEPO and the RSMCA algorithms also converge rapidly to the maximum power after the start of the simulation. The RSMCA being more rapid, less oscillating, and robust to brutal variation in irradiance and temperature.

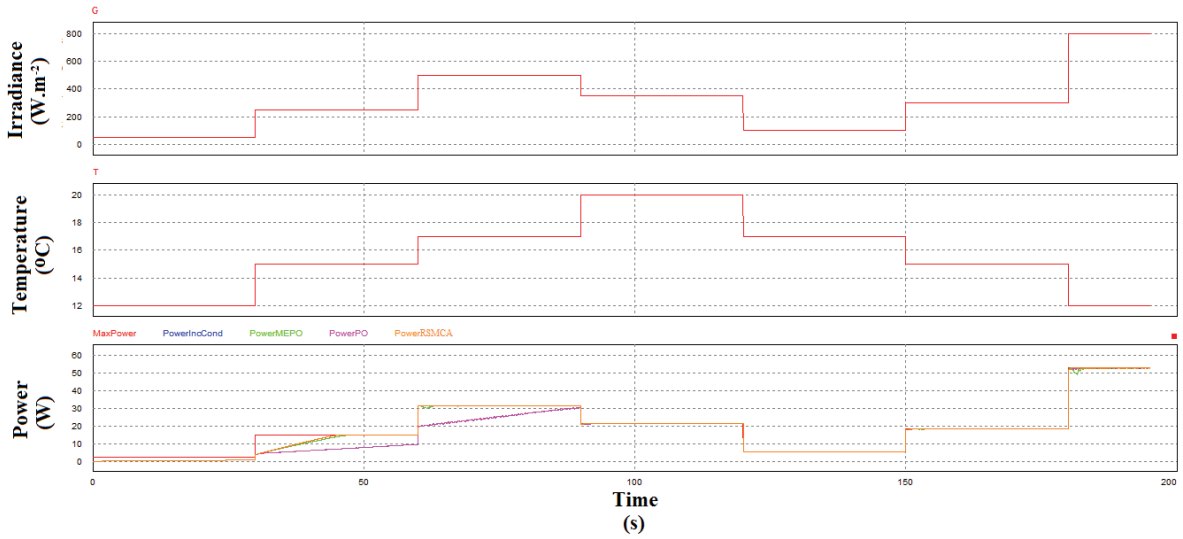

Figure 1.34: Comparison simulation of brutal change in irradiance and temperaure with low algorithm frequency (5Hz).

First order interpolation In order to approach a real situation, we performed a first order interpolation. The values of irradiance and temperature are interpolated in order to compare the algorithms in more realistic conditions.

In the first simulation we fix the algorithms' frequency to 10Hz. The interpolated irradiance and temperature are shown in figure 1.35 (upper graphs). We can see that that the difference between PO and IncCond algorithms from one hand and MEPO and RSMCA algorithms from the other hand is emphasized when we have high variation of environmental conditions and low algorithm frequency. The PO and MEPO algorithms did not reach the MPP even after 120 seconds. At the same time, the MEPO and the RMCA showed some disturbance during high power gradient, in fact these two algorithms are based on power gradient.

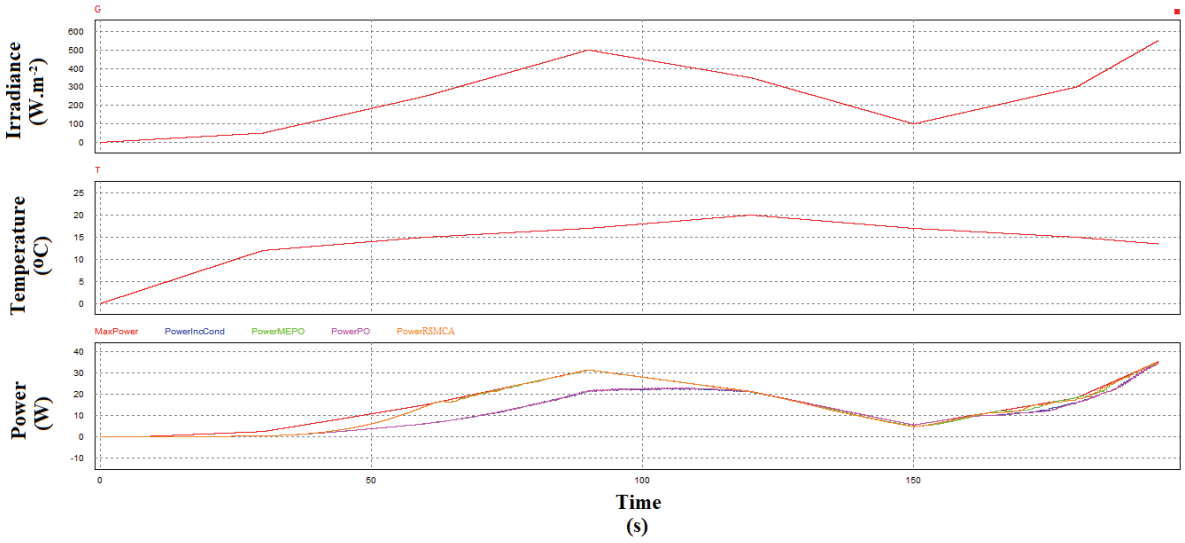

Figure 1.35: Comparative simulation result of Inerpolated variation of irradiance and temperature with low algorithm frequency (10Hz).

In the second simulation we take real data measured for one day. The record is done on 16/5/2012 at the University of Picardie Jules Verne Amiens, France. We choose 20 minutes that present high fluctuations of irradiation $\left(126W.m^{-2} - 878W.m^{-2}\right)$ and temperature $(14^oC - 26^oC)$. The data is available each 5 min which mitigates the high variation in environmental conditions (see figure 1.36). This is why the algorithms results are almost identical even for low frequency.

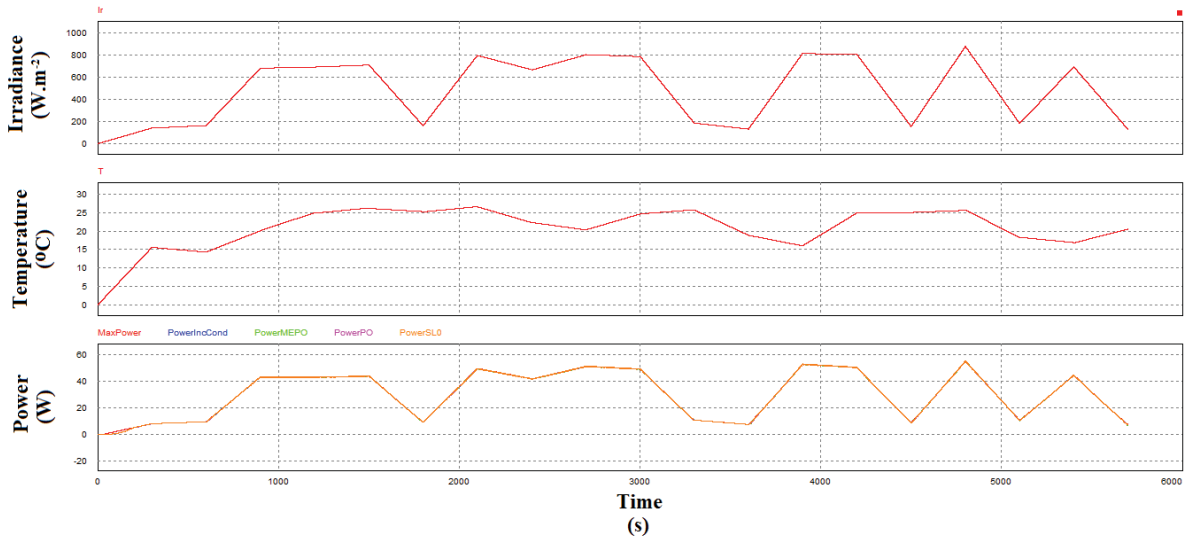

Figure 1.36: Comparative simulation result of Inerpolated variation of real irradiance and temperature with low algorithm frequency (10Hz).

1.7.3.3 Comparison summary

In this paragraph we recapitulate the comparison results between the 5 compared algorithms (PO, the MEPO, the IncCnd, the RSMCA, and the NL-ESC). The MEPO and RSMCA present more accuracy, speed, and less oscillation. The NL-ESC present the least oscillation, it is more robust in partial shading where we have multimodal power curves. When studying the algorithms' frequency we can see that MEPO and RSMCA present the highest robustness which makes them a better solution regarding hardware point of view. The controller clock frequency can be reduced, the additional loop error will be reduced, and the system will become less power consuming. Table 1.2 summarizes the key features of the MPPT algorithms.

Table 1.2: Summary table of MPPT algorithms comparison.

Algorithm	Reaching speed	Oscillation	Oscillation (Brutal change)	Algorithm frequency	Implementation
P&O	low	high	low	high	simple
IncCond	low	high	low	high	simple
MEPO	high	high	high	low	simple
RSMCA	high	high	high	low	simple
NL-ESC	low	low	high	high	complex

1.8 Conclusion

In this chapter we reviewed the physics and operating principles of solar cells. We recalled the physics of the PN junction including: doping, photogeneration, recombination, I-V characteristic, and equivalent circuit. We also looked at the engineering point of view of PV panels: operating, installing, and sizing. A survey on existing PV types has been presented where we can find special features of each technology. In addition, we conducted a study on MPPT algorithms. Where we compared different algorithms.

One of the important conclusions that we can grasp from this chapter is the selection of crystalline silicon panels on which we will apply our preventive control strategy on. In fact, crystalline PV panels present a good example that can be investigated in order to increase their lifespan. They have a high efficiency, terrestrial application, availability in raw materials, high knowledge; since a lot of research has been applied to crystalline PV panels. Another important electrical understanding of PV panels is their equivalent circuit. In fact, degradation process and faults will be affecting the equivalent circuit of PV panels.

In chapter 2 we survey degradation modes and faults affecting PV panels. We start to understand the physics behind each degradation mode and fault; what are the parameters affecting it and what is their effects on the equivalent circuit.

Chapter 2

Degradation and faults in PV panels

2.1 Introduction

PV panels convert the sun energy into electrical energy. Even though the primary energy (solar irradiation) is free, efficiency conversion of PV panels plays an important role in their development, market penetration, and share in total energy production. Many faults and failures leads to decreasing the conversion efficiency of PV panels. Efficiency loss is mainly noticed during the first two years of operation.

Although we are using PV panels as an energy source, and we take the role of operators, we must understand the degradation effects that happen to PV panels.

In this chapter, we survey all known degradation modes and faults that affect PV panels. We distinguish between degradation modes that continually reduce the efficiency during time and faults that suddenly occur and reduce sharply the power production.

2.2 Degradation Modes of PV panels

In this part we will focus on the mechanisms that decrease the efficiency of the PV panels with time. The PID (Potential Induced Degradation), the LID (Light Induced Degradation), UVD (UltraViolet light Degradation), MID (Moisture Induced Degradation), and Cell Cracks are the degradation modes that affect PV panels. Degradations generally affect PV panels during their life span. The latter is predicted to be between 25 and 30 years. Time compression is needed in order to study behavior of material during lifespan. Researchers apply accelerated life testing by increasing the stresses that PV panels are subject to; they increase the level of irradiance, temperature, or humidity [31]. This section is dedicated to describe and survey degradation modes of PV panels. Effect of environmental and operational conditions and modeling will be studied in the next chapter.

2.2.1 Potential Induced Degradation

PID increases the leakage current of a PV panel. The leakage current is defined to be the current that passes from the base to the emitter without traversing the load. The leakage current can be divided into four currents [2]. A current leaks through the soda-lime glass and through water molecules present on the surface (I1). A current leaks through electrons or ions present at the top surface of the cell (I2). A current leaks through the EVA (Ethylene Vinyl Acetate) encapsulation layer (I3). Finally, a current leaks in the back contact and closes the circuit (I4).

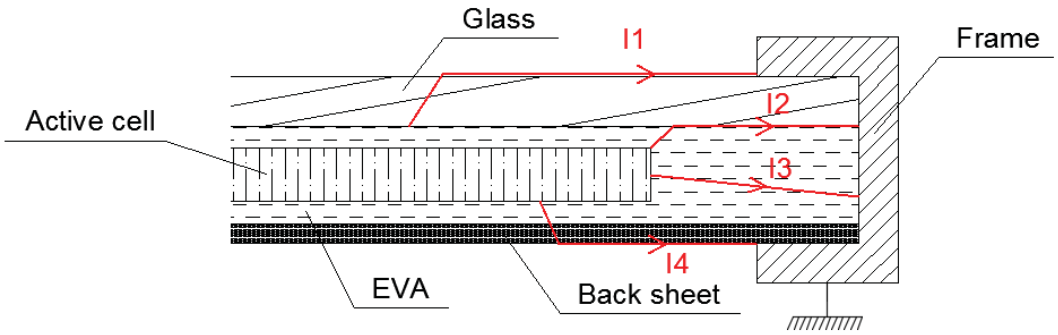

Figure 2.1: Cross section of a PV panel showing leakage current.

2.2.1.1 PID causes

Many causes lead to PID, they are divided into cell factors, module factors, system factors and environment factors. The cell factors are: the ARC, the emitter depth, and the base doping. Sodium ions present in the glass and in the ARC diffuse due to applied voltage into the front surface of the emitter. The sodium ions induce an electric field and cancel the passivation effect. This leads to an increased surface recombination current. Sodium may also diffuse into the n-doped emitter and acts as an electron acceptor and neutralize the n-doping. Tests showed that cells without ARC (SiN_x Layer) are not subject to PID [32]. Other tests prove that high resistivity (low doping rate) of the base increases immunity to PID [33]. The module factors are related to the resistivity and isolation of the encapsulation. Degradation of EVA and of the soda-lime glass results in a decrease of the module encapsulation resistivity. The system factor that affects PID is called surface polarization effect. All frames are grounded and the active cell is polarized. An array is made of series and parallel modules. The potential difference between the cell and the frame increases with the module position in the string. The voltage can reach 600V in US standards or 1500V in European standards. This high voltage will lead to accumulation of electrons on the front surface of the cell leading to an increased surface recombination current and leakage current. The environment factors are mainly the humidity and the temperature. In fact, water molecules at the surface of the module increase the conductivity between the cell front surface and the frame. The temperature also increases the conductivity of the EVA and the encapsulation.

To mitigate or to reverse the PID effect, we can invert the polarization of the module in correspondence to the ground. In this case, the high electric voltage between the cell and the frame will be inverted, thus reversing mobile charges (ions and electrons) diffusion. The cell surface will be clean thus decreasing the leakage current.

The installation of the panels can avoid PID. In a string of PV panels, the frames are grounded and one side of the active panels is grounded. If the positive side is grounded, the cells operate at negative voltage with respect to the frame. If the negative side is grounded, the cells operate at positive voltage with respect to the frame. In order to avoid PID, n-type front surface panels must be grounded from the positive side and p-type front surface panels must be grounded from the negative side. However, with new transformless inverters, the active panels must not be grounded to avoid ground fault current. In fact, the DC and the AC compartments are not isolated. In this case, the system operates at floating potential.

2.2.2 Light Induced Degradation

LID increases the recombination current in the base. LID occurs to n-type emitter crystalline silicon cells and to amorphous silicon cells. It affects c-Si cells for about 3% and affects a-Si cells for

about 30%.

2.2.2.1 LID in c-Si cells

In n-type emitter crystalline silicon cells, the base is doped with boron which is an acceptor. During Czochralski manufacturing process, oxygen atoms diffuse into silicon. When exposed to light, boron loses the hole and attracts the oxygen atom. A B-O complex is formed that forms a trap to electron and holes; thus increasing the recombination current. LID is proportional to the concentration of oxygen and boron in the base. Oxygen is present due to quartz crucible melting during hot silicon processing at 1412^oC. The concentration of oxygen is about $5 \times 10^{17}$to $1 \times 10^{18} cm^{-3}$. The concentration of boron affects the base resistivity and the total efficiency of the cell. That is why a tradeoff must be adopted and a base resistivity of 3-6 Ωcm is used [6]. The degradation takes about 72 hours of illumination. Several actions may be undertaken to recover from LID. First we may apply a forward bias current; this phenomenon is called "Current Induced Regeneration". Or we may anneal the bulk at a temperature of 200^oC [34]. Or we can wait for the B-O complex to regenerate with time under light [6]. To understand this mechanism, we define three states of the B-O complex. State 1 of the complex represents no activity toward electron hole recombination, this is the annealed state. State 2 of the complex represents high activity toward electron hole recombination, this is the degraded state. State 3 of the complex represents low activity toward electron hole recombination; this is the regenerated state [6]. The B-O complex can degrade under light from state 1 to state 2. The degradation follows an Arrhenius equation with an activation energy of 0.45 eV. The B-O complex can anneal from state 2 to state 1 under 200^oC for 30 min [34]. The B-O complex can regenerate from state 2 to state 3 under light soaking. The regeneration follows an Arrhenius equation with an activation energy of 1.4 eV. It is proved by experiments that the regenerated state (state 3) is stable at solar cell operating conditions; however the annealed state (state 1) is unstable.

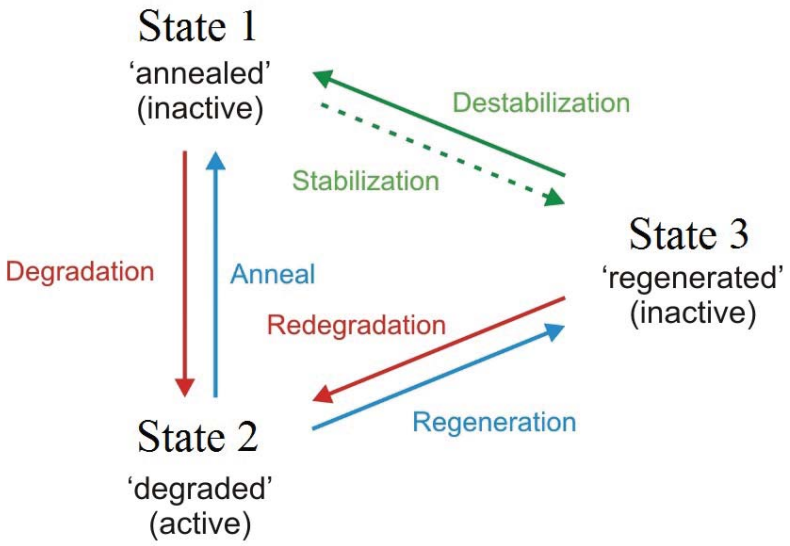

Figure 2.2: States of the B-O complex [6].

2.2.2.2 LID in a-Si:H cells

LID that occurs to amorphous silicon cells is called SWE. It was discovered by Staebler and Wronski in 1977. The excessive light soaking increases the dandling bonds which increase the recombination rate. This effect is noted in multi-junction micromorph solar cells. These cells are built by a μc-Si cell

in the bottom and an a-Si:H cell in the top. This structure is used because a-Si:H cell absorbs high energy photons.

Two possible ways exist for recovering from the SWE. The first is by annealing the bulk at a 160^oC for a few minutes [35]. And the other is by applying a bias voltage under illumination for 30 min. The above mentioned information proves the increase in efficiency of a-Si:H cells with high temperature. The bias voltage and the photo-generated electron will allow the reformation of the Si-H bond, which will recover the initial status of the cell.

2.2.3 Ultraviolet light Degradation

UV (UltraViolet) lights are electromagnetic radiations with a low wavelength (10nm-400nm). They carry high energy and are partially present in the terrestrial solar spectrum. Si represents low SR (Spectral Response) towards UV light and UV light is harmful to PV panels. In fact, PV panels are subject to yellowing after some years of operating under sun light. Precisely, the EVA encapsulation degrades under UV illumination and become light yellow, then yellow-brown, and dark brown. The latter is called EVA discoloration.

2.2.3.1 UV Degradation mechanism

The encapsulation is used for optical coupling, electrical isolation, physical isolation protection, mechanical support, and thermal conduction for the PV panel [36]. The EVA is constituted of 70% of gel content and 0.3 wt% (weight percentage) of Cyasorb UV 531. Cyasorb UV 531 absorbs UV light between 240 and 340nm. Its melting point is 49^oC. EVA degradation is calculated upon gel and Cyasorb UV 531 content. In fact, after UV light illumination, the gel content increases and the Cyasorb UV 531 content decreases. The latter is no more found in dark brown EVA. Acetic acid and volatile organic components are also produced by UV light exposure [37].

The effect of EVA discoloration on PV modules resides in the decrease of the EVA transmittance. In fact, with time the transmittance of the EVA encapsulation decreases for high energy photons; which reduces the PV panel efficiency.

2.2.4 Moisture Induced Degradation

PV panels are subject to moisture degradation. Water particles can enter the panel and cause degradation. This degradation mainly affects TCO based PV panels. Humidity causes delamination and mainly increases the series resistance of the equivalent circuit. In fact, it degrades the TCO layer. The TCO layer is used in thin film technologies because of its conductivity, transparency, and low cost. The TCO degrades under effect of humidity; its resistance increases. This is why PV panels undergo a Damp Heat test (DH). In the DH test, the panels or cells are exposed to an environment specified by an 85% RH (Relative Humidity) and an 85^oC. The test lasts for 1000h. According to IEC61646 standard, the efficiency of the panels must not decrease more than 5% [38].

2.2.5 Cell Cracks

PV panels are laminates generally formed by piling a glass superstrate, EVA encapsulation, cells, another EVA encapsulation, and the backsheet. The panel is then sealed with an aluminum frame. During manufacturing process and when exposed to mechanical loads (transportation, wind, snow...), cells suffer from cracks formation due to their plastic properties. We focus on crack formation in crystalline silicon based PV cells. The cells are connected using a silver printed grid on the surface of the cell. A copper bus-bar is soldered perpendicularly to the silver grid to connect adjacent cells. After formation a crack may not be harmful to a PV cell. We talk about cracks criticality. In fact, cracks divide the cell area into regions. A region becomes inactive if it is no more connected to the bus-bar. From the latter, if a crack is perpendicular to the bus-bars, it will not affect the cell. If a crack is parallel to the bus-bars and is situated between the two bus-bars, it will not affect the cell. If

a crack is parallel to the bus-bars and is situated in the external area, it will isolate an area of the cell making it inactive Fig 1.3 [7]. Dendritic cracks may also lead to some isolated areas of the cell.

A PV panel is mechanically modeled as a Navier plate; the frame is defined to have infinite stiffness and the laminate is considered to have the bending of a glass [7]. One of the most important environment effects on cell cracks is the snow. The latter is modeled by a uniform load on the Navier plate. Simulations and examinations of panels done by Schröder et al. give the following repartition and direction of cracks:

- Cracks are likely to happen on the diagonals and more on the center
- Cracks formation is negligible near the middle of edges
- Cracks orientation is parallel to diagonals in the diagonals
- Cracks orientation is parallel to the long edges in the center

It is clear that the most deteriorated cells are those located at the center and at the diagonals. In the center, strain is parallel to the small edges of the panel forming cracks parallel to the large edges of the panel or parallel to the bus-bars. In the diagonals, strain is perpendicular to the diagonals forming cracks parallel to the diagonals or making an angle with bus-bars [7]. Although orientation is important, it does not affect cells operation until it becomes deep and isolates cell areas. Based on experimental results, many cycles of humidity-freeze are needed to deepen the cracks and decrease the power output of the panel [39].

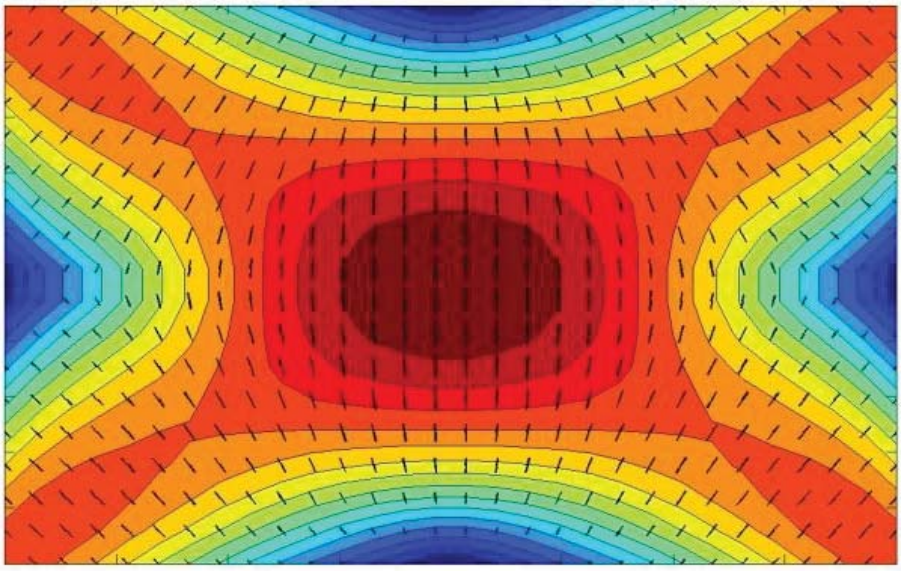

Figure 2.3: Strain distribution in a plate subject to uniform mechanical load [7].

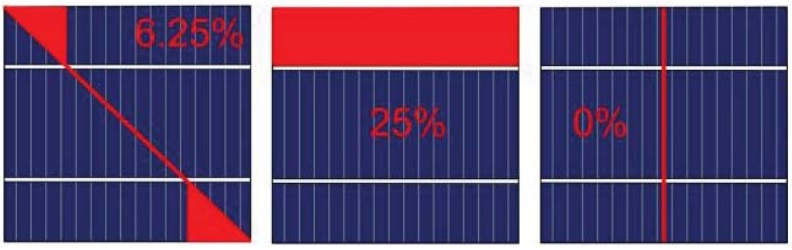

Figure 2.4: Cracks orientation from [7].

2.2.6 Salt mist and ammonia degradation

In some locations we may find other degradation agents that affect PV panels. Salt mist is found near coastlines or in sea applications or near roads that use salt for de-icing. Sodium chloride (NaCl) plays a catalyst role in the corrosion of metals. Salt mist mainly corrodes metallic parts of the panel and interconnects of the cells. PV panels are subject to salt mist and moisture corrosion test according to IEC 61701 standard. At the end of the test, the efficiency of the panel must not decrease more than 5% [40].

In other locations like agricultural areas, pig pens, and chicken farms ammonia gas is present. Nitrogen trihydride (NH_3) is also responsible of corrosion of metal parts of the module. After the ammonia IEC 62716 test, the efficiency must not decrease more than 5% [40].

2.3 Faults of PV panels

Faults can happen to all electrical equipments. They also attack all technological domains. Faults can decrease the efficiency of a production, they can present insecurity to operators, and can also wear the equipments. All the above can be seen in PV system especially efficiency decrease. In the previous section we discussed degradation modes that affect PV panels by reducing their efficiency across time. In this section we present faults that can happen to PV panels. We consider a fault any internal abnormal situation that leads to power decrease. From this we consider that partial shading, temperature mismatch, soiling, or dust accumulation are external, user reversible events that are not considered as faults. In this section we will discuss interconnect and connection faults, bridge and earth faults, and shunt path development.

2.3.1 Interconnect failure and connection faults

A single PV cell cannot generate a useful current or voltage. This is why cells are mounted in strings and in parallel to generate a useful level of voltage and current. Generally copper interconnect ribbons are used to connect cells to each others. A grid of Silver fingers is printed on the front surface of the cell, perpendicular interconnect bus-bars are soldered to the Silver fingers. The interconnects are then connected to the back of the adjacent cell. Solder joints that link copper interconnect to silver fingers represent the weakest point of the grid.

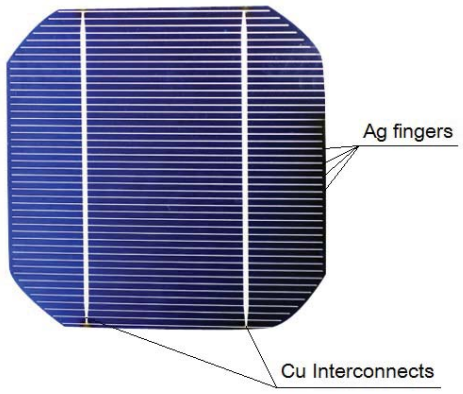

Figure 2.5: Ag fingers and Cu ribbons interconnects.

Solder joint failure is studied as an end-of-life event that limits the reliability of PV panels. Reliability is measured as the number of fatigue cycles during which solder joints can function before failure. In fact during accelerated tests, the resistance of solder joints increases slightly then rapidly reaches infinity when solder cracks completely. Three factors induce solder joint failure: humidity, salt mist, and temperature. Some tests showed that humidity leads only to some decrease in the number of cycles before failure. However, salt leads to a high decrease in the umber of cycles before failure [41].

We focus a lot on the effect of temperature on solder joints. In fact, PV panels are subject to thermal cycling; cold temperature during night and hot temperature during the day. Each day is considered a cycle. The solder is attached to two materials (Cu and Ag) having different CTE (Coefficient of Thermal Extension) this will cause shear strain. Shear strain is the deformation of a material perpendicularly to a given direction (see figure 2.6). It is given by the following formula [42]:

$$\Delta_\gamma = \Delta_\alpha \Delta T \times \frac{a}{h} \tag{2.1}$$

Where:
Δ_γ: shear strain.
Δ_α: difference of the thermal coefficient of expansion in $ppm.^\circ C^{-1}$.
ΔT: change in Temperature in$^\circ C$.
a : distance from neutral axis in m.
h : thickness of the solder in m.

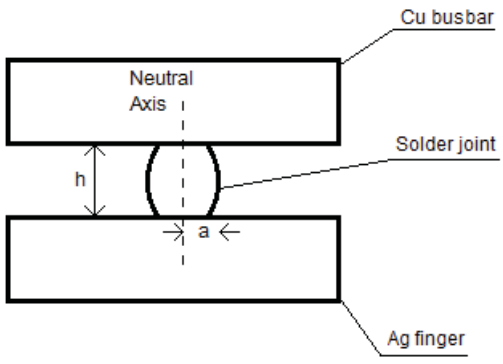

Figure 2.6: Solder joint between Ag and Cu.

We define global CTE mismatch the difference in CTE of the package materials like glass, backsheet, or solar cell. The latter will lead to global shearing. We define local CTE mismatch the difference in CTE of the materials to which the solder is attached like to copper and silver. During each thermal cycle, a shear strain is applied to the solder leading to stress, creep, and coarsening. The latter will lead to crack formation at the interface between solder and material. After a certain number of thermal cycles, the crack propagates and result in a full disconnection of solder and material. Which will lead to an infinite resistance. We are interested in the number of thermal cycles before the first failure occurs (failure free time). The failure free time decreases with the increase of the damage caused by each cycle. The damage is measured by the cyclic inelastic strain energy of each cycle. The number of free failure cycles is then given by [43, 44]:

$$N_0 = \frac{c}{A}\Delta\omega^{-0.925} \tag{2.2}$$

Where:
N_0: failure free time.
c : constant calibrating factor.
A : area of the interface between solder joint and material in in^2.
$\Delta\omega$: cyclic inelastic strain energy in psi.
For each thermal cycle we can plot the sheer stress against the sheer strain. We obtain a hysteresis loop which surface represent the cyclic inelastic strain energy. The latter corresponds to a work that coarsens the solder joint. the maximum sheer strain is proportional to the maximum temperature of the cycle [44]:

$$\gamma_{max} = \frac{L_D}{h}\Delta\alpha\,(T_{max} - T_{min}) \tag{2.3}$$

Where:
γ_{max}: maximum sheer strain.
L_D : half the diagonal dimension of the component in m.
$\Delta\alpha$: absolute difference in CTE of materials in$ppm.^{\circ}C^{-1}$.
T_{max} :maximum temperature of cycle in^oC.
T_{min} :minimum temperature of cycle in^oC.

Connection box, cables, and plugs may deteriorate or degrade. Their degradation may be induced by salt mist, ammonia, humidity, and temperature. Their resistance increases and causes power losses [45].

2.3.2 Bridge fault, earth fault

Bridge and earth faults occur when a connection happens between interconnects or between interconnects and earth. In other words, a connection happens between two points of different potential. The causes of ground faults and bridge faults may be resumed by deteriorating encapsulation, impact damage, or water corrosion in the PV module. By pass diodes being useful to panel lifetime, they present some failures like developing an internal resistor, disconnection, or becoming short circuited. The failures causes are ion migration, surface conduction, and metal corrosion [46]. The main parameters that affect by-pass diode lifespan are junction temperature and peak reverse voltage. Due to high temperature, the P and N dopants can diffuse and disable the diode. The failure rate of diodes follows an Arrhenius equation [46, 47]. The by pass diode short circuit failure can be modeled as a bridge fault.

2.3.3 Development of a shunt path

We consider a development of a path that links the positive and negative terminals of a PV panel. This is mainly due to connections or moisture forming a shunt path. Shunt path can occur due to

conductor insulation deterioration. High temperature occurring to connection box may lead to shunt path development. The path is modeled as a resistor in parallel with the panel.

2.4 Conclusion

In this chapter, we surveyed degradation modes and faults of PV panels. Degradation modes are Potential Induced Degradation, Light Induced Degradation, UltraViolet light Degradation, Moisture Induced Degradation, Cell Cracks, and Salt mist and ammonia degradation. The latters continually reduce the efficiency of the panel. We also surveyed faults that occur to PV panels. Faults are interconnect and connection faults, bridge and earth faults, and shunt path development. Faults occur to PV panels and lead to a sudden decrease in their power output.

The most important conclusion of this chapter is the fact that degradation modes and faults affect the packaging of the PV panel. The active area of the panel (the cell) remains intact and hardly presents any degradation.

In chapter 3 we will assess the effect of environmental conditions on the degradation rate of PV panels. We will also model the effect of degradation and faults on the equivalent circuit of the PV cell. We start by developping the model of an ideal PV panel, then we express the variation of the equivalent circuit of the cell as function of external meteorological conditions.

Chapter 3

Modeling of degradation and faults in PV panels

3.1 Introduction

In this chapter, we will develop a PV panel physical model that take into consideration degradations and faults. In the last chapter we surveyed the degradations modes and the fault that lead to aging of PV panels. In this chapter we explicit these degradations and faults into a mathematical model. After that the real time simulations problem will be considered with the models validation. We will start by developing a model of an ideal PV panel. Then we model degradations and their effect on the equivalent circuit. After that we model the effect of faults on the equivalent circuit. We will perform a model validation for each developed model using possible and available laboratory equipment.

3.2 Model of an ideal PV panel

3.2.1 Single cell modeling

Before starting the modeling of degradations and faults in PV panels, we present the mathematical model of a brand new PV panel. As developed in chapter 1, section 1.4.2, a PV cell is electrically modeled as a current source mounted in parrallel with two diodes and a shunt resistor. These above are mounted in series with a resistor. The output current of the cell is given by equation 1.14, and the equivalent circuit of the cell is recalled in figure 1.11.

The elements of the equivalent circuit are affected by temperature and irradiance as follows [48, 49]:
The effect of Irradiance and temperature on the short circuit current, I_{SC} is given by :

$$I_{SC} = I_{SC,STC} \times \frac{G}{G_{STC}} \times (1 + K_0 \times (T - T_{1,ref})) \tag{3.1}$$

Where:
$I_{SC,STC}$: Short ccircuit current in STC in A.
G: Irradiance in $W.m^{-2}$.
G_{STC}: Irradiance in STC $1000W.m^{-2}$.
K_0: temperature coefficient of I_{SC} in $A.K^{-1}$.
T: Temperature in K.
$T_{1,ref}$: reference temperature in STC in K.

The effect of temperature on the saturation current of the first diode, $I_{01}$is given by:

$$I_{01} = I_{01,STC} \times \left(\frac{T}{T_{1,ref}}\right)^3 \exp\left(\frac{q \times EG_{T_{1,ref}} \times \left(\frac{1}{T_{1,ref}} - \frac{1}{T}\right)}{K_B}\right) \tag{3.2}$$

Where:
$I_{01,STC}$: Diode saturation current of the first diode in STC in A.
q: electron charge $1.6 \times 10^{-19} C$.
$EG_{T_{1,ref}}$: Band gap energy in eV.

The effect of temperature on the saturation current of the second diode, $I_{02}$is given by:

$$I_{02} = I_{02,STC} \times \left(\frac{T}{T_{1,ref}}\right)^{3/2} \exp\left(\frac{q \times EG_{T_{1,ref}} \times \left(\frac{1}{T_{1,ref}} - \frac{1}{T}\right)}{K_B}\right) \tag{3.3}$$

Where:
$I_{02,STC}$: Diode saturation current of the second diode in STC in A.

The effect of temperature on the series resistor, $R_s$is given by:

$$R_s = R_{s,STC} \times \left(\frac{T}{T_{1,ref}}\right)^{TRs} \tag{3.4}$$

Where:
$R_{s,STC}$: series resistance in STC in Ω.
TRs: temperature coefficient of R_s.

The effect of temperature on the shunt resistor, $R_{sh}$is given by:

$$R_{sh} = R_{sh,STC} \times \left(\frac{T}{T_{1,ref}}\right)^{TRsh} \tag{3.5}$$

Where:
$R_{sh,STC}$: shunt resistance in STC in Ω.
$TRsh$: temperature coefficient of R_{sh}.

In order to calculate the output current given by equation 1.14 we need the elements of the equivalent circuit (equations 3.1-3.5), the operating temperature and the operating voltage. The Newton–Raphson method is used to calculate the output current.

3.2.2 PV panel modeling

A PV panel is generally composed of cells mounted in series. When working on the MPP the panel's generated current is limited by the cell generating the lowest current. Current mismatch my be caused by nonuniform temperature, nonuniform irradiance, or nonuniform cell degradation [50]. We consider all cells operating at the same voltage. N_s being the number of cell in series in the panel the voltage across each cell becomes [51]:

$$V = \frac{V_{pv}}{N_s} \tag{3.6}$$

Where:
V_{pv}: PV panel voltage.

We use a matrix representation for resuming equations 3.1-3.6

$$X = X_{stc} \times A \tag{3.7}$$

Where:

$$X = \begin{bmatrix} I_{SC} \\ I_{01} \\ I_{02} \\ R_s \\ R_{sh} \\ N_s \end{bmatrix} \tag{3.8}$$

$$X_{STC} = \begin{bmatrix} I_{SC<STC} & 0 & 0 & 0 & 0 & 0 \\ 0 & I_{01,STC} & 0 & 0 & 0 & 0 \\ 0 & 0 & I_{02,STC} & 0 & 0 & 0 \\ 0 & 0 & 0 & R_{s,STC} & 0 & 0 \\ 0 & 0 & 0 & 0 & R_{sh,STC} & 0 \\ 0 & 0 & 0 & 0 & 0 & N_{s,STC} \end{bmatrix} \tag{3.9}$$

$$A = \begin{bmatrix} \frac{G}{G_{STC}} \times (1 + K_0 \times (T - T_{1,ref})) \\ \left(\frac{T}{T_{1,ref}}\right)^3 \exp\left(\frac{q \times EG_{T_{1,ref}} \times \left(\frac{1}{T_{1,ref}} - \frac{1}{T}\right)}{K_B}\right) \\ \left(\frac{T}{T_{1,ref}}\right)^{3/2} \exp\left(\frac{q \times EG_{T_{1,ref}} \times \left(\frac{1}{T_{1,ref}} - \frac{1}{T}\right)}{K_B}\right) \\ \left(\frac{T}{T_{1,ref}}\right)^{TRs} \\ \left(\frac{T}{T_{1,ref}}\right)^{TRsh} \\ 1 \end{bmatrix} \tag{3.10}$$

The output current generated by the PV panel will be given by the following formula:

$$I = MIN_{i=1\ldots Ns}\left(I_{SC} - I_{01} \times \left(\exp\left(\frac{q \times \left(\frac{V_{pv}}{N_s} + R_s \times I\right)}{K_B \times T}\right) - 1\right) - I_{02} \times \left(\exp\left(\frac{q \times \left(\frac{V_{pv}}{N_s} + R_s \times I\right)}{2 \times K_B \times T}\right) - 1\right) - \frac{V_{pv} + I \times N_s \times R_s}{N_s \times R_{sh}}\right) \tag{3.11}$$

3.2.3 Ideal model validation

3.2.3.1 Experimentation apparatus

In this section we propose to validate the above developed model with real hardware experimentation. We build a PV system composed of a 100W PV panel (Monochrystalline, Solar Innova SI-ESF-M-M90-100W), halogen projectors, resistive load, DC/DC converter, back surface mounted thermocouples. Two thermocouples are used to measure the temperature of the panel. We use a pyranometer (Hukseflux-LP02) to measure the illumination. The PV panel is mounted on a two-axis rotating table. The table can rotate 180 degrees for each axis. The halogen projectors act as artificial lighting for the PV panel. One limitation in the laboratory testing is the limited illumination of artificial lighting. The DC/DC converter was developed in order to meet the requirements of the experimentation. The system is shown in figure 3.1.

Figure 3.1: Experimental apparatus of a PV panel.

The panel is constituted of a string of 36 cells. Two bypass diodes are implemented. Each one bypasses 18 cells in cases of partial shading. The panel visualization is represented in figure 3.2. The panel can deliver, at STC and at MPP, $18.4V$ and $5.43A$. Th open circuit voltage is $22.72V$ and the short circuit current is $5.64A$. The dimensions of the panel are $119.5cm \times 54.1cm \times 3.5cm$. The

panels' weight is $8kg$. The external frame is composed of aluminum ($AL6063-T5$). Each cell size is $12.5cm \times 12.5cm$. The panels' ingress protection rating is $IP-65$.

The halogen incandescent lamps ($3300K$) present an emulator towards of the sun. Even though they present low illumination ($529W.m^{-2}$ with 4 lamps) they present good conditions to test the operation of the panel towards its electrical and thermal properties. The installation of the halogen projectors is done as shown in figure 3.3 where the maximum uniform repartition of illumination is achieved. The projectors are mounted on a support and each halogen projector has three degrees of freedom. It can rotate over the Z-axis (Yaw), it can rotate over the X-axis (Roll), and its height can vary in order to increase or decrease the distance from the panel. The purpose of the three degrees of freedom is to position the projector in a way to get the best light uniform repartition on the surface of the PV panel.

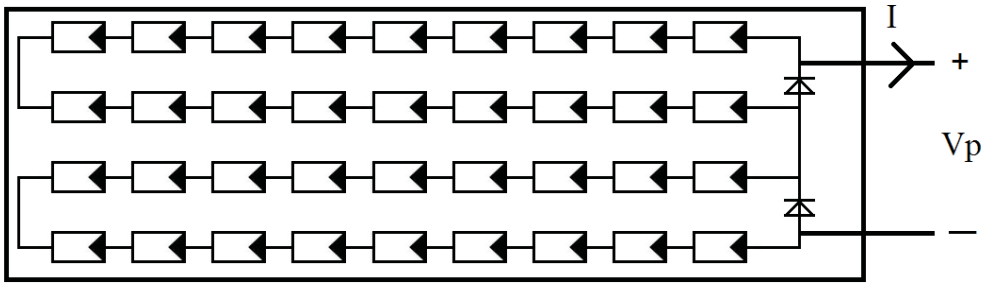

Figure 3.2: Visualization of the panel.

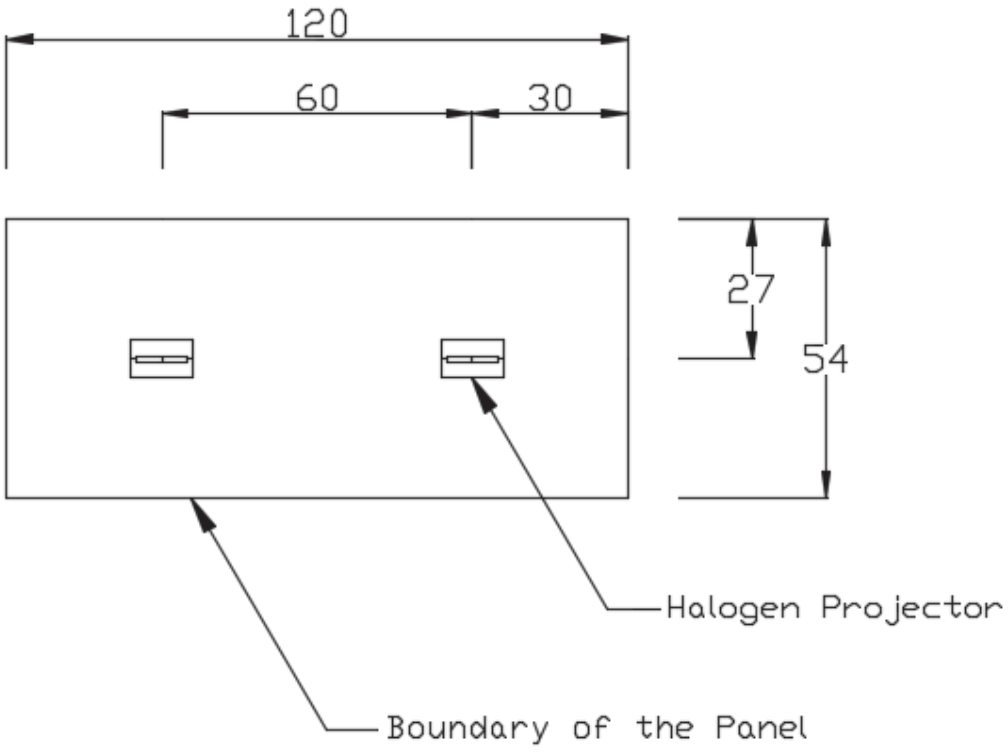

Figure 3.3: Upper projection view of the halogen projectors.

The two K type thermocouples are mounted on the back of the PV panel. One of them is mounted at the center of a cell and the other one is mounted in a region between two cells. The precision of the temperature sensor and the DAQ system is $0.1V$.

The DC/DC converter is constituted of a Buck-Boost converter. The control circuit is constituted of two NE555. The first one operates in the astable mode generating a clock reference PWM signal. The duty cycle of the signal must be high; it is fixed to 0.87. The second NE555 generates the PWM signal that is used to control the switch of the buck-boost converter. The reference voltage of the duty cycle is adjusted via a potentiometer or via an analog computer signal using a NI USB-6008 DAQ (Data Acquisition). A two-way switch is used to choose between the two operations. The DAQ is also used to measure the output current and output voltage of the PV panel. A shunt resistor (0.1Ω) is mounted in series with the panel. The voltage across the resistor represents an image of the current. A differential amplifier is used to measure the voltage across the panel. The switching devise is the IRFZ44N MOSFET (metal–oxide–semiconductor field-effect transistor). We present the values of the elements of the buck-boost converter in table 3.1.

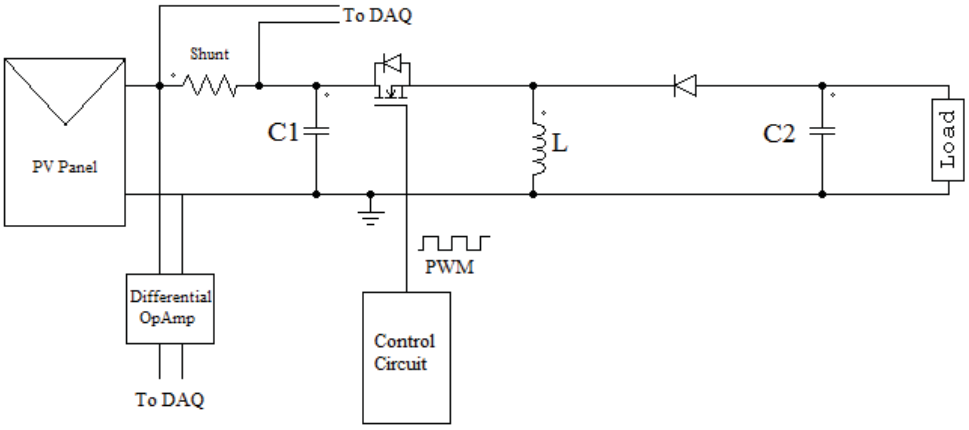

Figure 3.4: Block Diagram of the buck-boost converter.

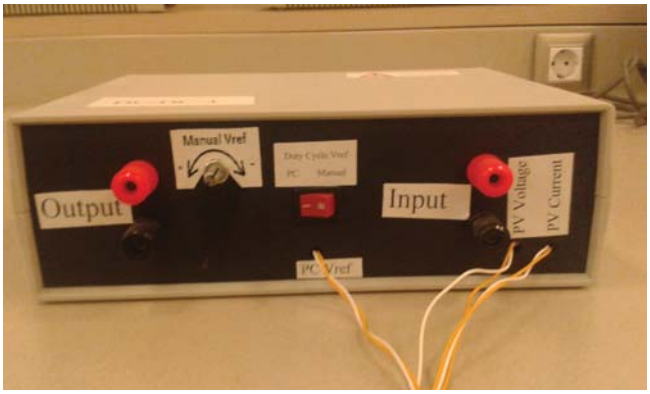

Figure 3.5: Photograph of the exterior of the of the DC/DC converter.

Table 3.1: Elements of the buck-boost converter.

Element	Value
Shunt	0.1Ω
C1	$470\mu F$
C2	$470\mu F$
L	$400\mu H$
Switching frequency	$5KHz$

3.2.3.2 Irradiance variation

In this experiment, we plotted the I-V characteristic of the real PV panel for three different illuminations (120 $W.m^{-2}$ (cyan), 190 $W.m^{-2}$(green), and 220 $W.m^{-2}$ (blue)) at fixed temperature (31.6^oC). We used the Levenberg–Marquardt algorithm to identify the elements of the equivalent circuit and the temperature coefficients ($I_{SC,STC}$, $I_{01,STC}$, $I_{02,STC}$, $R_{s,STC}$, $R_{sh,STC}$, N_s, K_0, TRs, $TRsh$). We can see that the model curve fits well the experimental data in figure 3.6 where the mean square error is 1.99×10^{-4}. The error between the model and the real experimental data is justified by the irradiance mismatch caused by the relative nonuniform light repartition on the surface of the PV panel. We present the elements of the equivalent circuit and temperature coefficient of the PV panel in table 3.2.

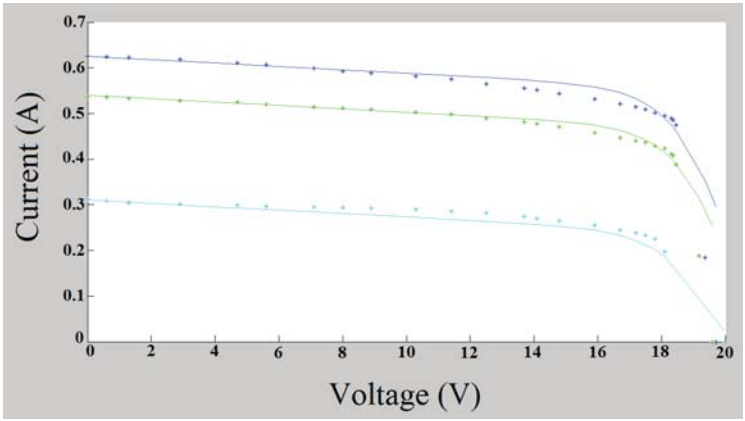

Figure 3.6: Experimental results in stars and mathematical model in continuous line for different irradiances.

3.2.3.3 Temperature variation

In this experiment, we plotted the I-V characteristic of the real PV panel for two different temperatures (35.7^oC (green) and 50.5^oC (blue)) at fixed illumination ($220W.m^{-2}$). We can see that the model curve fits well the experimental data in figure 3.7 where the mean square error is 4.9×10^{-3}. The latter relative high error may be caused by some mismatch error due to nonuniform irradiance.

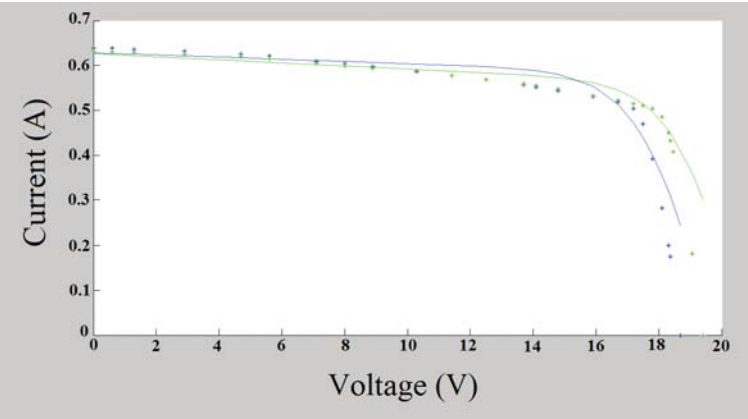

Figure 3.7: Experimental results in stars and mathematical model in continuous line for different temperatures.

Table 3.2: Elements of the equivalent circuit and temperature coefficient.

Element	Value
$I_{SC,STC}$	$2.8604A$
$I_{01,STC}$	$0.5A$
$I_{02,STC}$	$5.4759 \times 10^{-8}A$
$R_{s,STC}$	0.05Ω
$R_{sh,STC}$	226.088Ω
N_s	36
K_0	0.0006
TRs	0.0079
$TRsh$	0.0024

3.3 Modeling of degradation

3.3.1 Accelerated testing

In the literature, researchers apply accelerated tests to evaluate the effect of environmental and operational conditions on the degradation rate of PV panels. Accelerated testing is used to get an idea about products lifetime. It decreases testing time and testing cost. In this section we will develop an analytical model for the physical change of each of the elements of the equivalent circuit as function of time, environmental, and operational loading conditions. Going to the details of the equivalent circuit instead of developing a general efficiency equation of the panel is explained because each element composing the panel ages at different rates. In fact, elements are composed of different materials, and may encounter different stresses according to their position in the panel [52].

3.3.1.1 Arrhenius Equation

A reaction rate is exponentially dependent to the temperature. It is expressed by the Arrhenius Equation. The Equation was presented by Svante Arrhenius in 1889. The equation relates the reaction rate constant to the temperature as follows:

$$k = A \times \exp\left(\frac{-E_a}{R \times T}\right) \tag{3.12}$$

Where:
k: Constant rate.
A: Pre-exponent factor.
E_a: Activation energy in eV.
R: Gas constant $8.314 J.mol^{-1}.K^{-1}$.
T: Temperature in K.

3.3.2 PID Modeling

Many experiments were done to understand the PID. R. Swanson et al. explained the PID of PV panels. They showed how the system voltage operation affects PID. They started by doing a field observation. They noticed how the PID increases with the position of the panel in the string. Then they applied a set of laboratory tests to show he effect of module to ground voltage on PID [35]. Peter Hacke et al. showed the effect of temperature on PID. They also started by field observation and conducted experiments in test chambers to assess the temperature effect on the PID speed [53]. J. Berghold et al. showed the effect of relative humidity on PID. They also showed the effect of resistance and cell factors on the PID. They showed how to recover from PID by inverting the cell to frame potential [33].

The effect of PID on PV cells remains in increasing their leakage current. The latter corresponds to a decrease in the shunt resistance of the equivalent circuit. Studying the experiments done by researchers in literature we conclude that:

- The leakage current is proportional to the square of the panel voltage (panel to ground voltage) [53].
- The leakage current is proportional to the square of the panel lifetime [33].
- The leakage current is proportional to the square of the relative humidity [33].
- The leakage current follows an Arrhenius equation with an activation energy of 0.94 eV [53].

The variation of the shunt resistance is then given by the following equation:

$$R_{sh1,deg} = \frac{1}{7 \times 10^{-6} \times V_{PG}^2 \times RH^2 \times \exp\left(\frac{-90700}{R \times T}\right) \times t^2} \tag{3.13}$$

Where:
$R_{sh1,deg}$: is the value of the degraded shunt resistance in Ω.
V_{PG}: Panel to ground voltage in V.
RH: Relative Humidity.
t: Degradtion time in s.

The 7×10^{-6} factor depends from the cell factors, specially the resistivity of the base, it is used to tune the curve to the experiments.

3.3.3 LID modeling

As explained before in chapter 2, LID occurs to c-Si cells and to a-Si:H cells. LID increases the recombination current.

3.3.3.1 LID modeling in c-Si cells

Bhushan Sopori et al. explained LID in c-Si cells. They showed how LID affects the I-V characteristic and the equivalent circuit of the cell. They also showed how the system recovers by annealing [34]. A. Herguth et al. showed the effect of temperature on LID, they also defined new states of the Boron-Oxygen complex in c-Si cells. They showed how the FF, V_{OC}, I_{01}, I_{02} vary with time under LID [6].

Studying the experiments done by researchers in literature we conclude that:

- The recombination current change is proportional to the irradiance [6].
- The recombination current change follows an Arrhenius equation with an activation energy of 0.45eV [6].
- The recombination current change is proportional to the illumination time[6].

The saturation currents $I_{01}$and I_{02} in the equivalent circuit of the PV cell model recombination current. Their variation is fitted to the following equation:

$$I_{01,deg} = I_{01,STC} + 1.11 \times 10^{-10} \times \frac{G}{1000} \exp\left(\frac{-43268}{R \times T}\right) \times t \tag{3.14}$$

$$I_{02,deg} = I_{02,STC} + 1.11 \times 10^{-10} \times \frac{G}{1000} \exp\left(\frac{-43268}{R \times T}\right) \times t \tag{3.15}$$

Where:
$I_{01,STC}$: saturation current of D1 before degradation in STC in A.
$I_{02,STC}$: saturation current of D2 before degradation in STC in A.
G: irradiance in $W.m^{-2}$.

The 1.11×10^{-10} factor depends from the dimensions of the cell and from the born concentration, it is used to tune the curve to the experiments.

3.3.3.2 LID modeling in a-Si:H cells

A. Kolodziej explained the LID in a-Si solar cells which is called SWE. He also showed the effect of illumination intensity and temperature on SWE. A. Kolodziej explained how dandling bonds creates states in the band gap increasing the recombination current [22].

Studying the experiments done by researchers in literature we conclude that:

- The density of dandling bonds is proportional to the irradiance to the power of 2/3 [22].
- The density of dandling bonds is proportional to the illumination time to the power of 1/3 [22].
- The density of dandling bonds saturates at a level of 5×10^{16} cm^{-3} [22].
- The recombination current is proportional to the logarithm of the density of dandling bonds [2].
- The temperature does not affect the LID in a-Si solar cells [22].

The saturation currents $I_{01}$and I_{02} in the equivalent circuit of the PV cell model recombination current. Their variation is fitted to the following equation:

$$I_{01,deg} = I_{01,STC} + 1.9 \times 10^{-6} \times \log(6.52 \times 10^{-4} \times G^{2/3} \times t^{1/3}) \tag{3.16}$$

$$I_{02,deg} = I_{02,STC} + 1.9 \times 10^{-6} \times \log(6.52 \times 10^{-4} \times G^{2/3} \times t^{1/3}) \tag{3.17}$$

The 2.9×10^{-6} factor depends from the dimensions of the cell, it is used to tune the curve to the experiments.

3.3.4 UVD modeling

F. J. Pern explained UVD, he showed how the encapsulant discoloration occurs over time. He also showed how encapsulant transmittance vary as it degrades under UV light. In fact, as it degrades, the encapsulation will become more transparent to UV radiation and less transparent to useful radiations [54]. Jae-Seong Jeong et al. showed the effect of temperature on UVD. They also studied the Fourier transform infrared spectroscopy of EVA before and after exposure to UV light. The Fourier transform infrared spectroscopy analysis showed a transformation on the ethylene and vinyl acetate bonding [55]. F. J. Pern et al. showed the effect of UVD on the equivalent circuit of a PV cell; with encapsulant discoloration, the series resistor increases and the shunt resistor decreases. They also measured the quantum efficiency for different encapsulant discoloration levels, the quantum efficiency noticeably decreases with EVA discoloration [37].

We use the YI (Yellowness Index) to describe the encapsulation discoloration. We define the DYI (Delta YI) as a variable that changes in function of time to evaluate mathematically the degradation of EVA. Studying the experiments done by researchers in literature we conclude that:

- The DYI follows an Arrhenius equation with an activation energy of 0.93eV [55].
- The DYI is proportional to the irradiance intensity [54].
- The DYI is proportional to the logarithm of the illumination time [54].

The variation of the DYI is fitted to the following equation:

$$DYI = 5.68 \times 10^{11} \times \exp\left(\frac{-90000}{R \times T}\right) \times G \times \log\left(\frac{t}{3600}\right) \tag{3.18}$$

As EVA discoloration is a very long term process, the average temperature and irradiance are used. The 5.68×10^{11} factor is used to tune the curve to the experiments.

The variation of $R_s$and R_{sh} are fitted to the following equations [37]:

$$R_{s,deg} = R_{s,STC} + 9.9 \times 10^{-3} \times DYI \tag{3.19}$$

$$R_{sh2,deg} = R_{sh,STC} - 193 \times DYI \tag{3.20}$$

Where:
$R_{s,STC}$: series resistance before degradation in STC in Ω.
$R_{sh,STC}$: shunt resistance before degradation in STC in Ω.

3.3.5 MID modeling

Melissa A. Yaklin et al. showed the effect of humidity and temperature on TCO. They used a test chamber where they can change the humidity, and temperature artificial illumination is also used [56]. Michael D. Kempe showed the effect of temperature on moisture ingress into PV panels. He noted that different materials has different diffusivity towards water that varies by order of magnitudes. Using materials with low diffusivity means using high cost materials [57]. Jane Kapur et al. showed the geometrical repartition of water fraction in the PV panel after water ingress. They showed that water concentration in the panel is not uniform; water is more present at the edges of the panel. They also showed the effect of temperature on the diffusion of water for different types of materials [58].

Studying the experiments done by researchers in literature we conclude that:

- TCO degradation follows an Arrhenius equation with an activation energy of 0.91 eV [56].
- TCO degradation is proportional to the relative humidity [56].
- WVTR follows an Arrhenius equation with an activation energy of 0.38 eV [58].

- Moisture repartition in the panel follows a sine function having the lower value at the center of the panel and the higher value near the edges [58].

The variation of R_s is fitted to the following equation:

$$R_{s,deg} = R_{s,STC} + 1.11 \times 10^7 \times \exp\left(\frac{-87500}{R \times T}\right) \times \sin(Dist) \times \exp\left(\frac{-33678}{R \times T}\right) \times RH \times t \quad (3.21)$$

Where:
$Dist$: refers to the normalized distance from the center of the panel.

As WVTR is a very long term process, the average temperature is used. The factor 1.11×10^7 is used to tune the curve to the experiments.

3.3.6 Cells Cracks modeling

Sarah Kajari-Schröder et al. showed the geometrical and directional repartition of cracks in a PV panel. They simulated the panel as a Navier plate to identify the direction of strain and deduce the direction of cracks. They also analyzed real panels after mechanical stress [7]. They also explained how cracks become critical to PV cell. They applied freeze cycles to cracked cells to show when cracks become critical to cells [39]. M. Köntges et al. showed the effect of cracks on power production. They showed that the power loss is nearly proportional to the inactive cell area. They also showed that the number of defected cells in a string do not affect the power decrease [59].

Cracks are generally a recombination center for electron-hole pairs. However, when cell regions are isolated or inactive, the photo-generated current $I_{SC,deg}$ and the recombination currents ($I_{01,deg}$ and $I_{02,deg}$) will decrease respecting the following equations [59, 60]:

$$I_{SC,deg} = I_{SC,STC} \times \left(1 - \frac{A_{inacive}}{A_{total}}\right) \quad (3.22)$$

$$I_{01,deg} = I_{01,STC} \times \left(1 - \frac{A_{inacive}}{A_{total}}\right) \quad (3.23)$$

$$I_{02,deg} = I_{02,STC} \times \left(1 - \frac{A_{inacive}}{A_{total}}\right) \quad (3.24)$$

Where:
$A_{inacive}$: isolated area of the cell in m^2.
A_{total}: total area of the cell in m^2.

The fraction $\frac{A_{inacive}}{A_{total}}$ depends from the position of the cell in the panel. In fact, we recall that:

- Cracks are likely to happen on the diagonals and more on the center
- Cracks formation is negligible near the middle of edges
- Cracks orientation is parallel to diagonals in the diagonals
- Cracks orientation is parallel to the long edges in the center

We also recall that cracks need freeze cycles to create the isolated sheets.

As PV panels are generally expected to operate at MPP, the I_{MPP} is lower than the I_{SC}, no power decrease is noted if the following equation is respected [59]:

$$\frac{A_{inacive}}{A_{total}} < \frac{I_{SC} - I_{MPP}}{I_{SC}} \quad (3.25)$$

Where:

I_{MPP}: current at maximum power point in A.

However, when the isolated cell area increases (exceeding 8%), we start noticing power losses. The cell becomes reverse biased and the current of the string flows through it. If its breakdown voltage is high, the current flows in the bypass diode if present [59]. It must be noted that having one or more cracked cells in a string lead approximately to the same power loss. The power loss depends from the cell having the maximum isolated area.

3.4 Real-time simulation model

3.4.1 Model development

In the previous section the external conditions (temperature, irradiance, and relative humidity) were taken as average values. In this section, we present a more precise model; the model takes into consideration the variation of temperature, irradiance, and relative humidity along the day and the year. Thus the degradation equations are derived with respect to time. The proposed model will generate the elements of the equivalent circuit of the PV cell, that vary nonlinearly. The model is time varying.

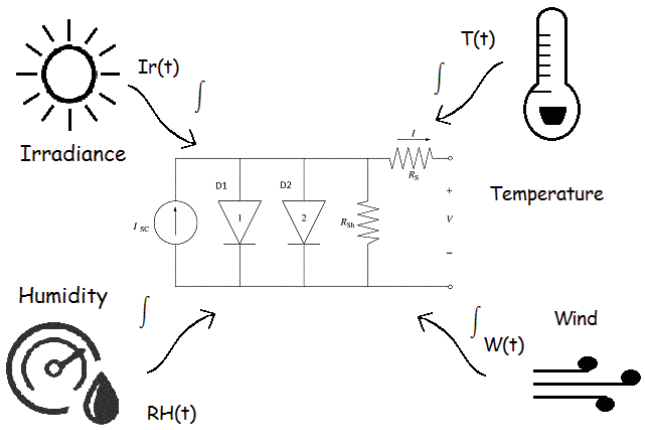

Figure 3.8: Summary representation of the real time simulation model.

We choose to apply the model for monocrystalline silicon cells. In fact, crystalline based panels are the most used in the market. They present the highest efficiency between commercial PV panels. Besides, tests and research is most applied to crystalline based PV panels. PID, LID, UVD, and cell cracks are the degradation modes that affect monocrystalline PV panels.

Equations 3.13 and 3.20 model two parallel resistances that represents PID and UVD. The equivalent shunt resistance is given by:

$$R_{sh,deg} = \frac{R_{sh,STC} - 193 \times DYI}{\left(7 \times 10^{-6} \times V_{PG}^2 \times RH^2 \times \exp\left(\frac{-90700}{R \times T}\right) \times t^2\right) \times (R_{sh,STC} - 193 \times DYI) + 1} \tag{3.26}$$

Deriving equation 3.26 with respect to time gives us the variation of R_{sh}:

$$\frac{dR_{sh,deg}}{dt} = \frac{\partial R_{sh,deg}}{\partial DYI} \times \frac{\partial DYI}{\partial t} + \frac{\partial R_{sh,deg}}{\partial RH} \times \frac{\partial RH}{\partial t} + \frac{\partial R_{sh,deg}}{\partial T} \times \frac{\partial T}{\partial t} + \frac{\partial R_{sh,deg}}{\partial t} \times \frac{\partial t}{\partial t}$$

$$\frac{dR_{sh,deg}}{dt} = \frac{-193 \times \left(\left(7 \times 10^{-6} \times V_{PG}^2 \times RH^2 \times \exp\left(\frac{-90700}{R \times T}\right) \times t^2\right) \times (R_{sh,STC} - 193 \times DYI) + 1\right)}{\left(\left(7 \times 10^{-6} \times V_{PG}^2 \times RH^2 \times \exp\left(\frac{-90700}{R \times T}\right) \times t^2\right) \times (R_{sh,STC} - 193 \times DYI) + 1\right)^2} \times \frac{\partial DYI}{\partial t} +$$

$$\frac{193 \times \left(7 \times 10^{-6} \times V_{PG}^2 \times RH^2 \times \exp\left(\frac{-90700}{R \times T}\right) \times t^2\right) \times \left(R_{sh,T_{1,ref}} - 193 \times DYI\right)}{\left(\left(7 \times 10^{-6} \times V_{PG}^2 \times RH^2 \times \exp\left(\frac{-90700}{R \times T}\right) \times t^2\right) \times (R_{sh,STC} - 193 \times DYI) + 1\right)^2} \times \frac{\partial DYI}{\partial t} +$$

$$\frac{-2 \times RH \times \left(7 \times 10^{-6} \times V_{PG}^2 \times \exp\left(\frac{-90700}{R \times T}\right) \times t^2\right) \times (R_{sh,STC} - 193 \times DYI)}{\left(\left(7 \times 10^{-6} \times V_{PG}^2 \times RH^2 \times \exp\left(\frac{-90700}{R \times T}\right) \times t^2\right) \times (R_{sh,STC} - 193 \times DYI) + 1\right)^2} \times \frac{\partial RH}{\partial t} +$$

$$\frac{-\frac{90700}{R \times T^2} \times \left(7 \times 10^{-6} \times V_{PG}^2 \times RH^2 \times \exp\left(\frac{-90700}{R \times T}\right) \times t^2\right) \times (R_{sh,STC} - 193 \times DYI)}{\left(\left(7 \times 10^{-6} \times V_{PG}^2 \times RH^2 \times \exp\left(\frac{-90700}{R \times T}\right) \times t^2\right) \times (R_{sh,STC} - 193 \times DYI) + 1\right)^2} \times \frac{\partial T}{\partial t} +$$

$$\frac{-2 \times t \times \left(7 \times 10^{-6} \times V_{PG}^2 \times RH^2 \times \exp\left(\frac{-90700}{R \times T}\right)\right) \times (R_{sh,STC} - 193 \times DYI)}{\left(\left(7 \times 10^{-6} \times V_{PG}^2 \times RH^2 \times \exp\left(\frac{-90700}{R \times T}\right) \times t^2\right) \times (R_{sh,STC} - 193 \times DYI) + 1\right)^2} \times \frac{\partial t}{\partial t} \quad (3.27)$$

Where:
t: Time in s.
The initial value before degradation of the variable R_{sh} will be set to:

$$R_{sh0} = R_{shs,STC} \quad (3.28)$$

Deriving equation 3.14 with respect to time gives us the variation of I_{01} :

$$\frac{dI_{01,deg}}{dt} = \frac{\partial I_{01,deg}}{\partial t} \times \frac{dt}{dt} + \frac{\partial I_{01,deg}}{\partial G} \times \frac{dG}{dt} + \frac{\partial I_{01,deg}}{\partial T} \times \frac{dT}{dt} + \frac{\partial I_{01,deg}}{\partial \frac{A_{inactive}}{A_{total}}} \times \frac{d\frac{A_{inactive}}{A_{total}}}{dt}$$

$$1.11 \times 10^{-10} \times \frac{G}{1000} \exp\left(\frac{-43268}{R \times T}\right) \times \left(1 - \frac{A_{inactive}}{A_{total}}\right) +$$

$$\left(1.11 \times 10^{-10} \times \frac{1}{1000} \exp\left(\frac{-43268}{R \times T}\right) \times t\right) \times \left(1 - \frac{A_{inactive}}{A_{total}}\right) \frac{dG}{dt} +$$

$$\left(1.11 \times 10^{-10} \times \frac{G}{1000} \times \frac{43268}{R \times T^2} \exp\left(\frac{-43268}{R \times T}\right) \times t\right) \times \left(1 - \frac{A_{inactive}}{A_{total}}\right) \times \frac{dT}{dt} -$$

$$\left(I_{01,T_{1,ref}} + 1.11 \times 10^{-10} \times \frac{G}{1000} \exp\left(\frac{-43268}{R \times T}\right) \times t\right) \times \frac{d\frac{A_{inactive}}{A_{total}}}{dt} \quad (3.29)$$

The initial value before degradation of the variable I_{01} will be set to:

$$I_{010} = I_{01,STC} \quad (3.30)$$

Deriving equation 3.15 with respect to time gives us the variation of I_{02} :

$$\frac{dI_{02,deg}}{dt} = \frac{\partial I_{02,deg}}{\partial t} \times \frac{dt}{dt} + \frac{\partial I_{02,deg}}{\partial G} \times \frac{dG}{dt} + \frac{\partial I_{02,deg}}{\partial T} \times \frac{dT}{dt} + \frac{\partial I_{02,deg}}{\partial \frac{A_{inactive}}{A_{total}}} \times \frac{d\frac{A_{inactive}}{A_{total}}}{dt}$$

$$\frac{dI_{02,deg}}{dt} = 1.11 \times 10^{-10} \times \frac{G}{G_{STC}} \exp\left(\frac{-43268}{R \times T}\right) \times \left(1 - \frac{A_{inactive}}{A_{total}}\right) +$$

$$\left(1.11 \times 10^{-10} \times \frac{1}{G_{STC}} \exp\left(\frac{-43268}{R \times T}\right) \times t\right) \times \left(1 - \frac{A_{inactive}}{A_{total}}\right) \frac{dG}{dt} +$$

$$\left(1.11 \times 10^{-10} \times \frac{G}{G_{STC}} \times \frac{43268}{R \times T^2} \exp\left(\frac{-43268}{R \times T}\right) \times t\right) \times \left(1 - \frac{A_{inactive}}{A_{total}}\right) \times \frac{dT}{dt} -$$

$$\left(I_{02,T_{1,ref}} + 1.11 \times 10^{-10} \times \frac{G}{G_{STC}} \exp\left(\frac{-43268}{R \times T}\right) \times t\right) \times \frac{d\frac{A_{inactive}}{A_{total}}}{dt} \quad (3.31)$$

The initial value before degradation of the variable I_{02} will be set to:

$$I_{020} = I_{02,STC} \tag{3.32}$$

Deriving equation 3.18 with respect to time gives us the variation of DYI :

$$\frac{dDYI}{dt} = \frac{\partial DYI}{\partial t} \times \frac{dt}{dt} + \frac{\partial DYI}{\partial Ir} \times \frac{dG}{dt} + \frac{\partial DYI}{\partial T} \times \frac{dT}{dt}$$

$$\frac{dDYI}{dt} = 5.68 \times 10^{11} \times \exp\left(\frac{-90000}{R \times T}\right) \times G \times \frac{1}{3600 \times t} \times \frac{dt}{dt} +$$

$$5.68 \times 10^{11} \times \exp\left(\frac{-90000}{R \times T}\right) \times \log\left(\frac{t}{3600}\right) \times \frac{dG}{dt} +$$

$$5.68 \times 10^{11} \times \frac{90000}{R \times T^2} \exp\left(\frac{-90000}{R \times T}\right) \times G \times \log\left(\frac{t}{3600}\right) \times \frac{dT}{dt} \tag{3.33}$$

The initial value before degradation of the variable DYI will be set to:

$$DYI_0 = 0 \tag{3.34}$$

Deriving equation 3.19 with respect to time gives us the variation of R_s :

$$\frac{dR_{s,deg}}{dt} = \frac{\partial R_{s,deg}}{\partial DYI} \times \frac{\partial DYI}{\partial t} = 9.9 \times 10^{-3} \times \frac{\partial DYI}{\partial t} \tag{3.35}$$

The initial value before degradation of the variable R_s will be set to:

$$R_{s0} = R_{s,STC} \tag{3.36}$$

Deriving equation 3.22 with respect of time gives us the variation of I_{SC} :

$$\frac{dI_{SC,deg}}{dt} = \frac{\partial I_{SC,deg}}{\partial \frac{A_{inactive}}{A_{total}}} \times \frac{d\frac{A_{inactive}}{A_{total}}}{dt}$$

$$\frac{dI_{SC,deg}}{dt} = -I_{SC,STC} \times \frac{A_{inacive}}{A_{total}} \tag{3.37}$$

The initial value before degradation of the variable I_{SC} will be set to:

$$I_{SC0} = I_{STC} \tag{3.38}$$

The system takes as input the Irradiane G, the cell temperature T, the relative humidity RH, and the operating voltage V_{PG}. The system will compute the derivative of the inputs, when needed, in order to calculate the values of equations 3.27, 3.29, 3.31, 3.33, 3.35, and 3.37. The initial values (I_{SC0}, R_{sh0}, I_{010}, I_{020}, and R_{s0}), the constants (G_{STC} and R) are internal values of the system. The outputs of equations 3.27, 3.29, 3.31, 3.35, and 3.37 are integrated to generate the elements of the equivalent circuit of the PV cell (I_{SC} , R_{sh} , I_{01} , I_{02} , and R_s).

The inputs of the system are set as follows. The irradiance varies following a sine function during the day [4]. In regions situated in the northern hemisphere, during June-September period, the irradiance increases. In regions situated in the southern hemisphere, during June-September period, the irradiance decreases. The temperature varies alongside the irradiance during the day. The relative humidity varies inversely to temperature [61].

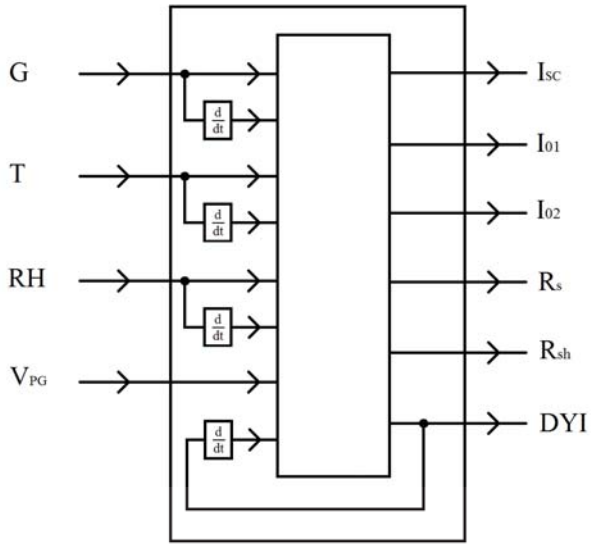

Figure 3.9: Degradation model of crystalline silicone cells.

The above ODE (Ordinary Differential Equation) were implemented in a DEE block (Differential Equation Editor) in Matlab/simulink software. The outputs of the DEE block are the elements of the equivalent circuit of a PV cell. The elements are then updated according to the conditions of temperature and irradiance. The current generated is calculated using the Newton-Raphson method. The state space modeling gives us the facility to express the equivalent circuit of the the PV cell as states. In fact, the system is non linear and time varying and we have expressed these states as function of inputs (Irradiance, Temperature, Relative Humidity...) and time. The degradation state at a certain time t results from the addition of degradations that took place before t.

3.4.2 Simulation results

In this section we present the simulation results using the developed model. The key performance index chosen is the normalized efficiency $NE(t)$. The normalized efficiency at an instant t is the efficiency at that instant divided by the efficiency at time t_0, where t_0 corresponds to the time before degradation.

$$NE(t) = \frac{Eff(t)}{Eff(t_0)} \tag{3.39}$$

Where:
$Eff(t)$: Efficiency of the panel at time t.
$Eff(t_0)$: Efficiency of the panel at time t_0.

In the first simulation, we present (figure 3.10) the normilised efficiency of a PV panel for 40 years. The location of the site has an average irradiance of $709W.m^{-2}$, an average Relative Humidity 50%, and the average panel temperature is 45^oC. We can see a fast decrease in efficiency for the first 4-5 years, then a slow decrease that is marked by a logarithmic shape. We can also see that the curve has a wave-like shape.

In fact, the rapid decrease in efficiency during the first operation years is caused by the PID and LID. The leakage current caused by the PID will saturate and the LID degradation is limited to the first days of operation. The UVD, which depends algorithmically as function of time still decreasing the panel efficiency for all the 40 years of operation. The wave-like shape is explained by the fact that

during summer, high temperature and high irradiance are noted which will cause severe decrease in efficiency during this period. During winter, lower temperature and irradiance are noted which will cause lower degradation rate.

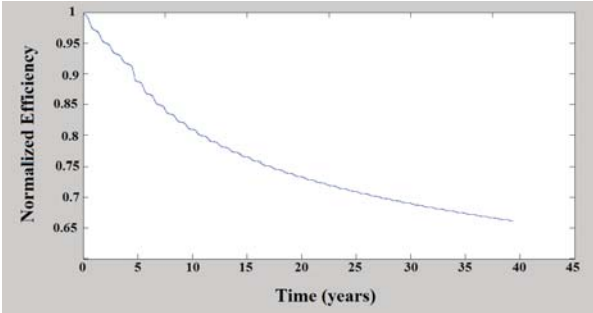

Figure 3.10: Normalized efficiency for 40 years (G=709$W.m^{-2}$, RH=50%, T=45^oC).

3.4.2.1 Irradiance variation

In the second simulation, we present (figure 3.11) the normalized efficiency of 3 PV panels for 40 years. The location of the sites of the 3 panels have different average irradiance; 550$W.m^{-2}$ in blue, 709$W.m^{-2}$ in green, and 850$W.m^{-2}$ in cyan. The average Relative Humidity is 50%, and the average panel temperature is 45^oC. We can see that the degradation rate of the panels increase with the irradiance. In fact, irradiance influence the LID increasing the recombination current (I_{010} and I_{020}) and the UVD by increasing the DYI.

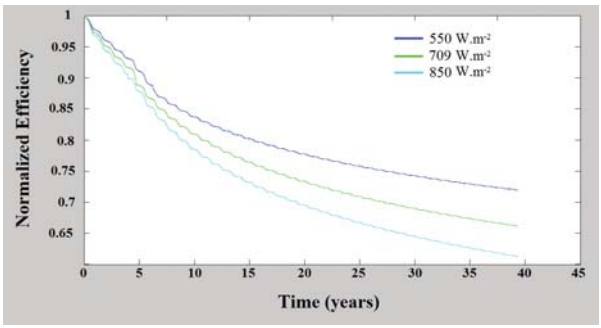

Figure 3.11: Normalized efficiency for 40 years (G=550$W.m^{-2}$ in blue, G=709$W.m^{-2}$ in green, G=850$W.m^{-2}$ in cyan).

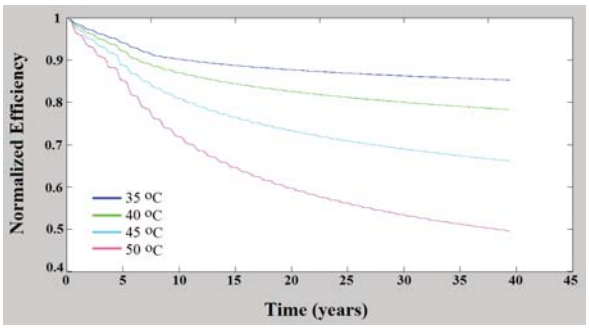

Figure 3.12: Normalized efficiency for 40 years (T=35^oC in blue, T=40^oC in green, T=45^oC in cyan, T=50^oC in magenta).

3.4.2.2 Temperature variation

In the fourth simulation, we present (figure 3.12) the normalized efficiency of 4 PV panels for 40 years. The location of the sites of the 4 panels imply different average temperatures of the 4 panels; 35^oC in blue, 40^oC in green, 45^oC in cyan, and 50^oC in magenta. The average Relative Humidity is 50%, and the average irradiance is 709$W.m^{-2}$. We can see that the degradation rate of the panels increase with the temperature. In fact, temperture influence the LID increasing the recombination current (I_{010} and I_{020}), the UVD by increasing the DYI, and the PID by decreasing the shunt resistance.

3.4.3 Real-time model validation

In this paragraph we try to validate our developed real time simulation model. It is literally impossible to use a panel for 40 years and measure its efficiency. We try to compare our results with gathered data from researchers who recorder the degradation rate of PV panels. Recoded degradation rates are nearly absent in literature since the related topic is new [62]. The rule-of-thumb of PV industry averages the degradation rate of PV panels to be $-1\%.year^{-1}$ [62].

Researchers measured power generated from PV panels, irradiance, and temperature. When these data are available, they can calculate the efficiency of PV panels [63]. Sometimes they may require analytical methods to determinate the efficiency of PV panels [64].

The degradation rates recorded over time showed the same result of our real time simulation model. In some references we see the average degradation rate to be close to $-0.8\%.year^{-1}$ which is close to our simulated result [63, 65]. The degradation rate started with high levels $-0.8\%.year^{-1}$ for c-Si PV panels, then the degradation rate decreased logarithmically with time which alines with our simulated results [64]. In other reported results, c-Si modules present degradation rates between $-0.5\%.year^{-1}$ and $-1\%.year^{-1}$, unfortunately no weather conditions has been reported [62] . The degradation rates reported for the fist years of installation is high compared to the average degradation a 10 years operation period [62].

In table 3.3 we can see a summary of recorded degradation rates of PV panels with their corresponding location. We can see a varying degradation rate between regions were hotter regions witness higher degradation rates witch alines with our developed model. In addition, high degradation rate is noted for the first operational years which alines with our developed model.

Table 3.3: Summary of recorded degradation rates in literature [8, 9].

Degradation rate $(\%.year^{-1})$	Years of Operation $(years)$	Location
-0.5	20	Utah, USA
-2.6	20	Riyadh, Saudi Arabia
-0.95	5	Tokyo, Japan
-0.62	10	Hamamatsu, Japan

3.5 Modeling of faults

In this section we model the effect of faults on the equivalent circuit of the PV panel. The three main faults are interconnect and connection faults, bridge and earth faults, and shunt path development. We also show the effect of each fault on the I-V characteristic. We validate the proposed model with real measured data done on the experimentation apparatus described in paragraph 3.2.3.1.

3.5.1 Model development

3.5.1.1 Modeling of interconnect and connection faults

Interconnect failures and external connections degradation can increase the series resistance which will lead to decrease in power generation. We model the new developed resistance with a resistance R_c connected in series with the panel. The equivalent system is visualized in figure 3.13 where we present the panel constituted of 36 cells with a resistor connected in series with it.

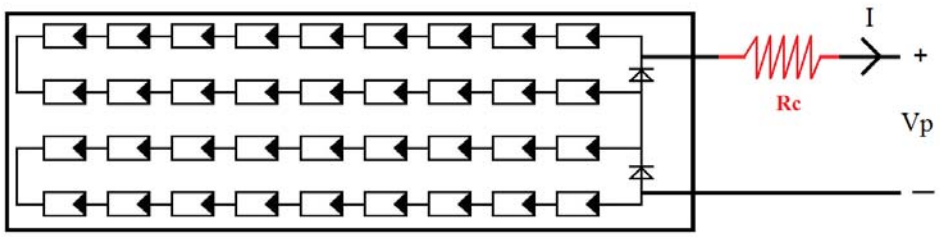

Figure 3.13: PV panel with connection resistance.

The output current generated by the PV panel will be given by the following formula:

$$I = MIN_{i=1\ldots Ns}\left(I_{SC} - I_{01}\times\left(\exp\left(\frac{q\times\left(\frac{V_{pv}}{N_s}+(R_s+R_c)\times I\right)}{K_B\times T}\right)-1\right) - I_{02}\times\left(\exp\left(\frac{q\times\left(\frac{V_{pv}}{N_s}+(R_s+R_c)\times I\right)}{2\times K_B\times T}\right)-1\right) - \frac{V_{pv}+I\times(N_s\times R_s+R_c)}{N_s\times R_{sh}}\right) \tag{3.40}$$

The effect of interconnect and connection faults on the I-V characteristic resides in decreasing the slope near the V_{oc} (open circuit voltage).

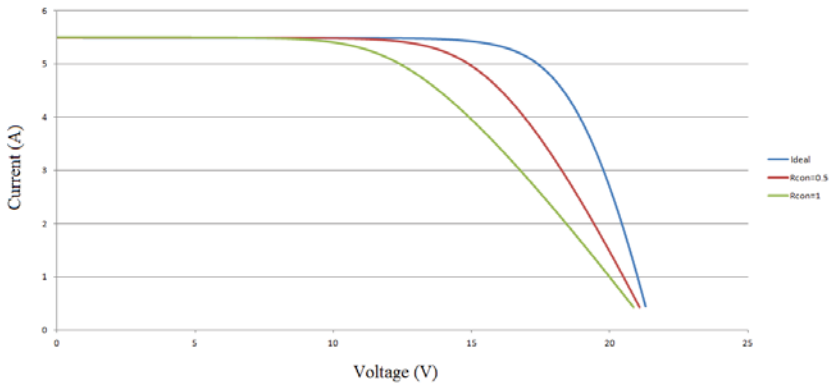

Figure 3.14: Effect of interconnect and connection fault on the I-V characteristic.

3.5.1.2 Modeling of bridge and earth

We consider that the NCC (NonCurrent Carrying) metals are grounded and the negative terminal of the panel is grounded [66]. We consider a bridge fault that shorts n adjacent cells ($n < N_s$). The voltage across the panel will be divided into the remaining ($N_s - n$) cells. The current will always be limited by the cell delivering the smallest current. The fault system is visualized in figure 3.15.

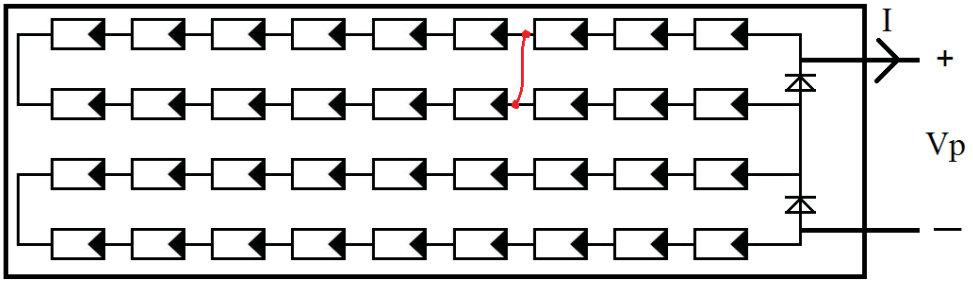

Figure 3.15: PV panel with bridge connection.

The output current generated by the PV panel will be given by the following formula:

$$I = MIN_{i=1\ldots Ns}\left(I_{SC} - I_{01}\times\left(\exp\left(\frac{q\times\left(\frac{V_{pv}}{N_s-n}+(R_s\times I)\right)}{K_B\times T}\right)-1\right) - I_{02}\times\left(\exp\left(\frac{q\times\left(\frac{V_{pv}}{N_s-n}+R_s\times I\right)}{2\times K_B\times T}\right)-1\right) - \frac{V_{pv}+I\times(N_s-n)\times R_s}{(N_s-n)\times R_{sh}}\right) \quad (3.41)$$

The effect of bridge and earth fault on the I-V characteristic resides in shifting the curve to the left proportionally to n, the number of shorted cells.

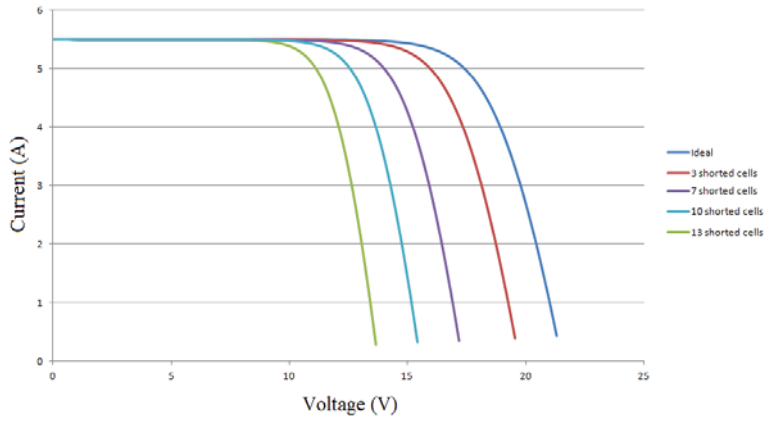

Figure 3.16: Effect of bridge and earth fault on the I-V characteristic.

3.5.1.3 Modeling of shunt path

The developed shunt path is represented by an external resistor of the panel R_{path}. The shunt path resistor is situated after the series resistor as shown in figure 3.17. The fault system is visualized in figure 3.18.

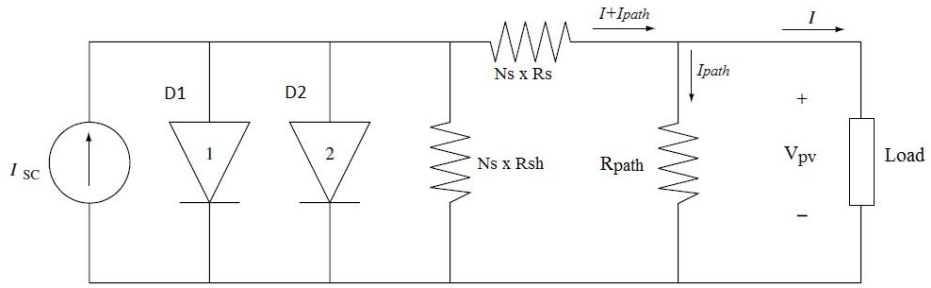

Figure 3.17: Equivalent circuit of the PV panel with a shunt path.

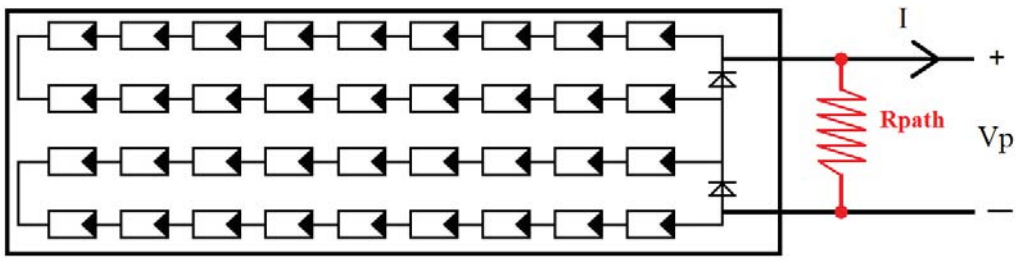

Figure 3.18: PV panel with shunt path.

The output current generated by the PV panel will be given by the following formula:

$$I = MIN_{i=1\ldots Ns}$$

$$I_{SC} - I_{01} \times \left(\exp\left(\frac{q \times \left(\frac{V_{pv}}{N_s} + R_s \times \left(I + \frac{V_{pv}}{R_{path}} \right) \right)}{K_B \times T} \right) - 1 \right) -$$

$$I_{02} \times \left(\exp\left(\frac{q \times \left(\frac{V_{pv}}{N_s} + R_s \times \left(I + \frac{V_{pv}}{R_{path}} \right) \right)}{2 \times K_B \times T} \right) - 1 \right) - \frac{V_{pv} + \left(I + \frac{V_p}{R_{path}} \right) \times N_s \times R_s}{N_s \times R_{sh}} - \frac{V_{pv}}{R_{path}} \quad (3.42)$$

The effect of shunt path fault on the I-V characteristic resides by increasing the slope near the I_{SC}.

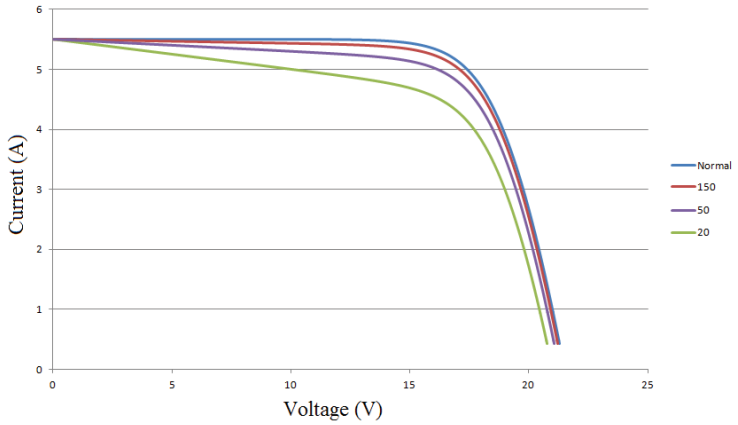

Figure 3.19: Effect of shunt path fault on the I-V characteristic.

3.5.2 Faults model validation

The experimental apparatus previously described in paragraph 3.2.3.1 is used to validate the faults model. A series of experiments is elaborated. For each fault the I-V characteristic is plotted according to measured data on the real hardware. The model fault is compared with the real data.

3.5.2.1 Validation of interconnect and connection faults model

We connect a resistor in series with the panel of the apparatus. And we plot the I-V characteristic from real measured data. The curve is plotted for an irradiance of $220W.m^{-2}$ and a temperature of 50.5^oC. The resistance in series R_c takes 6 values: 0Ω, 1Ω, 2Ω, 3Ω, 4Ω, 5Ω. The mean square error is 2.6×10^{-3}. The error between the model and the real experimental data is justified by the irradiance mismatch caused by the relative nonuniform light repartition on the surface of the PV panel. We can see that the real data and the model curves fit well in figure 3.20.

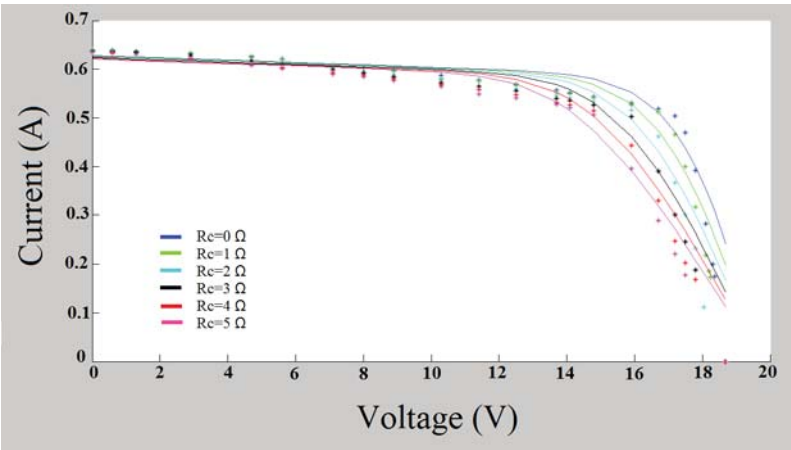

Figure 3.20: Experimental results in stars and mathematical model in continuous line for different connection resistances.

3.5.2.2 Validation of shunt path fault model

We connect a resistor in parallel with the panel of the apparatus. And we plot the I-V characteristic from real measured data. The curve is plotted for an irradiance of $220W.m^{-2}$ and a temperature of 50.5^oC. The resistance in parallel R_{path} takes 4 values: infinite value (no shut path), 850Ω, 300Ω, 150Ω. The mean square error is 1.8×10^{-3}. The latter relative high error may be caused by some mismatch error due to nonuniform irradiance. We can see that the real data and the model curves fit well in figure 3.21.

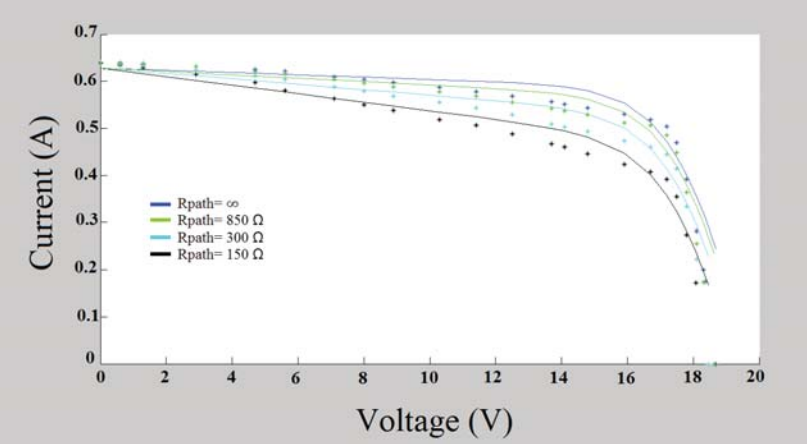

Figure 3.21: Experimental results in stars and mathematical model in continuous line for different shunt path resistances.

3.5.2.3 Validation of the bridge and earth fault model

In this section, we would like to short circuit a number of cells and test the previously developed fault model. It is impossible to perform this experience without damaging the PV panel of the experimental apparatus (Monochrystalline, Solar Innova SI-ESF-M-M90-100W). For that we bought 6 small PV cells assembly. Each assembly is composed of 16 cells mounted in series. The assembly can deliver $0.3W$, $3.8V$ at MPP during STC conditions (251 SOLAR CELL 3.8V 0.3Watt). We fixed the 6 cells assembly on a planar support. We connected them in series (see figure 3.22). The system is now constituted of 96 cells in series. We perform 3 tests where: in the first one no assembly is shorted, in the second one we short one assembly, and in the third one we short 3 assemblies (see figure 3.23). Shorting an assembly is equivalent to a bridge fault shorting a number of cells.

We plot the I-V characteristic from real measured data using artificial lighting. And using the Levenberg–Marquardt algorithm we identified the elements of the system. The mean square error is 2.4263×10^{-7}.

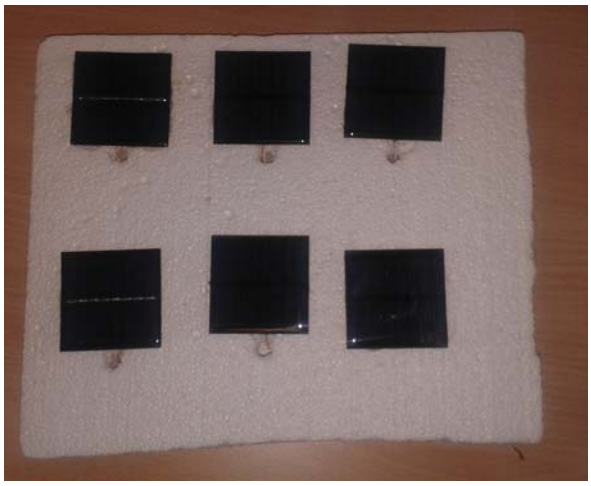

Figure 3.22: Photo of the 6 connected assemblies.

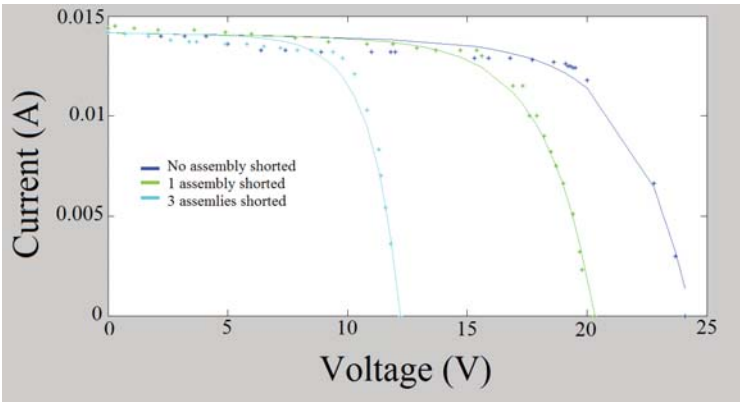

Figure 3.23: Experimental results in stars and mathematical model in continuous line for different numbers of shorted assemblies.

Table 3.4: Elements of the equivalent circuit of the PV asembly.

Element	Value
$I_{SC,STC}$	0.0407
$I_{01,STC}$	7.08×10^3
$I_{02,STC}$	73.24
$R_{s,STC}$	0.0017
$R_{sh,STC}$	4.48×10^4
N_S	96

3.6 Conclusion

In this chapter we developed a complete model that simulates the aging modes of PV panels. We started by developing a model of an ideal PV panel. Then we expressed how degradation modes affect the elements of the equivalent circuit of PV panels as function of time, operational, and environmental conditions. We derived the latter expressions in order to obtain a real time model. The model generates the equivalent circuit at each instant. The advantage of our approach is by taking into consideration the time varying external conditions; degradation rates varies with time. In addition we developed a model that describe faults that happens to PV panels. All developed models were validated using appropriate and available materials and data.

The most important conclusion of this chapter is that degradation rate is not constant during the year, the month and even during the day. The rate is affected by external environmental conditions. It is noted that during summer seasons, degradation rate is higher that winter seasons.

Temperature is a key parameter that affects the aging of PV panels. In fact, temperature affects PID, LID, MID, and UVD degradation modes. We propose in chapter 4 to develop a thermal model of PV panels. The model will simulate the thermal behavior of PV panels as function of environmental and operational conditions. This will lead to an understanding of thermal behavior and possible mitigation of degradation rate of PV panels.

Chapter 4

Thermal model of a PV panel

4.1 Introduction

As stated in Chapters 2 and 3, temperature plays an important factor in degrading and causing faults to PV panels. Besides, temperature increases the degradation rate of PV panels exponentially, following an Arrhenius equation. This emphasizes the need to develop a thermal model of a PV panel in order to understand its thermal behavior. In this chapter, we will present the heat fluxes that affect the temperature of the panel. We will present an equivalent electric model based on the analogy between electricity and thermal behavior. Then we will build the model under Comsol Multiphysics software. At the end, a validation of the thermal behavior is achieved with the experimentation apparatus.

4.2 Nominal Operating Cell Temperature

A PV panel can be seen, from a thermal view, as a flat plate that receives solar irradiance and evacuates thermal power to ambient air. Manufacturers describe the cells temperature by a simple expression based on the NOCT (Nominal Operating Cell Temperature). NOCT is the measured cell temperature for an ambient temperature of $20°C$, an irradiance of $800W.m^{-2}$ and a wind speed of $1m.s^{-1}$. The panel temperature is then calculated using the following formula [51]:

$$T_{cell} = T_{amb} + \frac{NOCT - 20}{800} \times G \tag{4.1}$$

Where:

T_{amb}: temperature of ambiant air in ^oC.

G: irradiance in $W.m^{-2}$.

T_{cell}: estimated temperature of the cell in ^oC.

This simple equation does not take into consideration the wind speed, the electrical operating point of the panel and the internal heat generation. In the next paragraph, we will be detailing the thermal model of a PV panel that gives more precise results.

4.3 Detailed thermal model of a PV panel

In this chapter we present a more detailed thermal model of PV panels where we take into consideration external heat sources, operating conditions, internal heat sources, and heat dissipation. The external heat source is represented by the sun. The operating conditions of the PV panel (operating voltage) directly affect the output power generated by the PV panel. The internal heat sources are due to the internal series and shunt resistors that generate heat due to Joule effect. Heat is being dissipated to the outside of the panel via convection and radiation.

4.3.1 Heat transfer model

A PV panel resembles a flat plate that receives solar irradiation and generates electrical power. In literature, many researchers developed thermal models of PV panel. A. D. Jones et al. developed a thermal model of PV panels based on energy balance. They considered the panel as a uniform flat plate that receives irradiation, generates electrical power, and dissipates heat to the exterior [67]. G.M. Tina et al. added the effect of the operating voltage or the extracted power on the thermal energy balance of a PV panel. They divided the panel into three layers consisting of glass, cells, and backsheet. They also developed an electrical model of the PV panel [51]. Ruhi Bharti et al. conducted experiences that showed the effect of the electrical load on the NOCT. They noticed the effect of internal heat generation of PV cells [68]. M. Rosa-Clot et al. studied a hybrid thermal-photovoltaic panel; the TEPSI (Thermal Electric Solar Panel Integration). They showed how solar energy can be transformed into thermal and electrical energy [69]. S. Armstrong et al. developed the equivalent RC thermal circuit of a PV model. They also investigated the time constant of the thermal behavior of PV panels [70].

The incident irradiation is the main heat source that contributes to heating the panel. This source is reduced by a factor of 5% due to reflection.

$$\dot{Q}_{sun} = 0.95 \times A \times G \tag{4.2}$$

Where:
A: Total area of the panel in m^2.

The electrical output power generated by the PV panel depends on its operating voltage. In fact, the P-V characteristic is non linear and presents a mountain shape. The electric output power represents a sink to the thermal system model and is given by:

$$P_{ele} = V_{pv} \times I \tag{4.3}$$

The conversion efficiency of conventional PV panels is limited to 18%. The remaining input power will generate heat to the panel. This heat will be dissipated to exterior via convection and radiation [71]. The conduction is neglected because the panel nearly presents no contact to solids. The convection occurs on the front, back, and edge surfaces. The thermal convection flux to ambient air is expressed by the following formula:

$$\dot{Q}_{conv} = h \times A \times (T_{amb} - T_{pv}) \tag{4.4}$$

Where:
h: heat transfer coefficient in $W.m^{-2}.K^{-1}$.

The heat transfer coefficient depends on many parameters as the wind velocity, the air density, the tilt angle of the panel, and the dimensions of the panel. Using some approximations we can correlate the heat transfer coefficient to the wind velocity by the following formula [72]:

$$h = 5.67 + 3.86 \times Wv \tag{4.5}$$

Where
Wv: Wind velocity in $m.s^{-1}$.

The radiation occurs from the front and the back surfaces. The thermal radiation flux is expressed by the following formula:

$$\dot{Q}_{rad} = \epsilon \times \sigma \times A \times \left(T_{amb}^4 - T_{pvs}^4\right) \tag{4.6}$$

Where:
ϵ: Emissivity.
σ: Stephan-Boltzmann constant $5.67 \times 10^{-8} W.m^{-2}.K^{-4}$.

T_{pvs}: Temperature of PV panel surface in K.
The front surface emissivity is taken 0.9 [70, 67] the back surface emissivity is taken 0.84 [70].

The internal heat sources of the panel are due to the Joule effect of the series and shunt resistors. In fact, current passing through the printed Ag fingers and through the Cu bus-bars will lead to a localized heat generation modeled by the series resistor R_s. Besides, current passing through a path around the cell will lead to a localized heat generation modeled by the series resistor R_{sh}. The joule heat generated is given by the following formula:

$$P_j = n \times R_s \times I^2 + n \times \frac{(V + R_s \times I)^2}{R_{sh}} \tag{4.7}$$

Where:
n: number of cells.
R_s: series resistance of the cell in Ω.
R_{sh}: shunt resistance of the cell in Ω.

In summary, a PV panel is a flat plate that heats due to the difference between incident irradiance and generated electrical power. The panel also heats because of to internal heat generation due to Joule effect. Because of temperature difference between panel and ambient air, heat dissipates from the panel to exterior via convection and radiation (see figure 4.1).

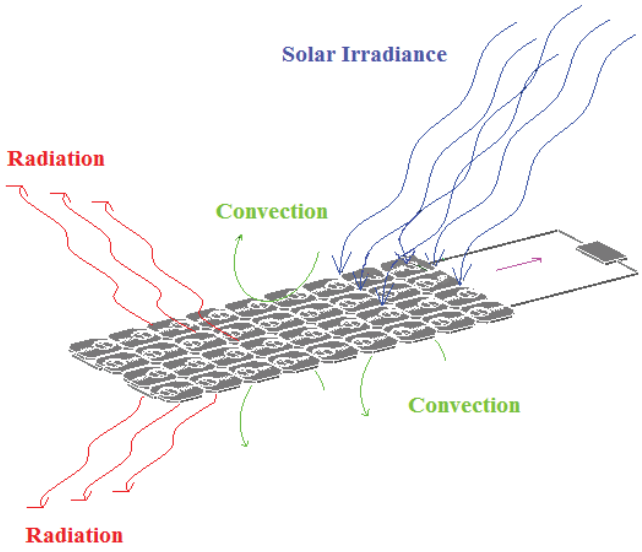

Figure 4.1: Thermal behavior of a PV panel.

4.3.2 Equivalent thermal circuit model of PV panels

In this section we build an equivalent electric circuit of the thermal behavior of a PV panel. This circuit is based on the analogy between Fourier's law $\dot{Q} = \frac{\Delta T}{R_t}$ and Ohm's law $I = \frac{\Delta V}{R_e}$. Where $\dot{Q}$ is the rate of heat conduction, ΔT is the temperature difference across the slab, R_t is the thermal resistance of the slab, I is the current, ΔV temperature difference across the resistor, and R_e is the electrical resistance. The thermal capacitance (or heat capacity) of an element is equal to the amount of heat needed to increase its temperature by 1K. The following table shows analogy between thermal and electrical elements:

Table 4.1: Analogy between thermal and electrical elements.

Thermal		Electrical	
Temperature	T (K)	Voltage	V (V)
Heat	$\dot{Q}$(W)	Current	I (A)
Thermal Resistance	$R_t(K.W^{-1})$	Resistance	$R_e(\Omega)$
Thermal Capacitance	$C_t(W.s.K^{-1})$	Capacitance	$C_e(A.s.V^{-1})$

From the above we can derive the equivalent thermal circuit of a PV panel:
According to equation 4.4 the front and back convection resistance is given by:

$$R_{tconv} = \frac{(T_{amb} - T_{pv})}{\dot{Q}_{conv}} = \frac{1}{h \times A} \tag{4.8}$$

According to equation 4.6 the front and back radiative resistance are given by:

$$R_{trad} = \frac{1}{\epsilon \times \sigma \times A \times \left(T_{amb}^2 + T_{pvs}^2\right) \times (T_{amb} + T_{pvs})} \tag{4.9}$$

We can see clearly that the radiative resistance depends on the surface and ambient temperatures.

Heat propagates into the PV panel by conduction. We divide the panel into three layers: the glass, the PV material, and the backsheet. The conduction resistance of the glass, the PV material, and the backsheet are given by:

$$R_{tcond} = \frac{d}{k \times A} \tag{4.10}$$

Where:
d : thickness of the layer in m.
k: thermal conductivity of the material in $W.m^{-1}.K^{-1}$.
For the materials listed, k=1.8 $W.m^{-1}.K^{-1}$ for glass, k=93 $W.m^{-1}.K^{-1}$ for PV, and k=0.2 $W.m^{-1}.K^{-1}$ for backsheet (Tedlar) [70].

The thermal capacitance of each layer is given by:

$$C_t = \rho \times Cp \times A \times d \tag{4.11}$$

Where:
ρ: density of the material in $kg.m^{-3}$.
Cp: specific heat capacity in $J.kg^{-1}.K^{-1}$.
For the materials listed Cp=500$J.kg^{-1}.K^{-1}$, ρ=3000$kg.m^{-3}$ for glass, Cp=840$J.kg^{-1}.K^{-1}$, ρ=2000$kg.m^{-3}$ for PV, and Cp=1250$J.kg^{-1}.K^{-1}$, ρ=1200$kg.m^{-3}$ for backsheet [70].
The irradiance heat source is modeled as a current source:

$$I_G = G \times A$$

The internal heat sources and the output electrical power are modeled by another current source:

$$I_{int} = P_j - Pele$$

The complete equivalent thermal circuit is presented in figure 4.2.

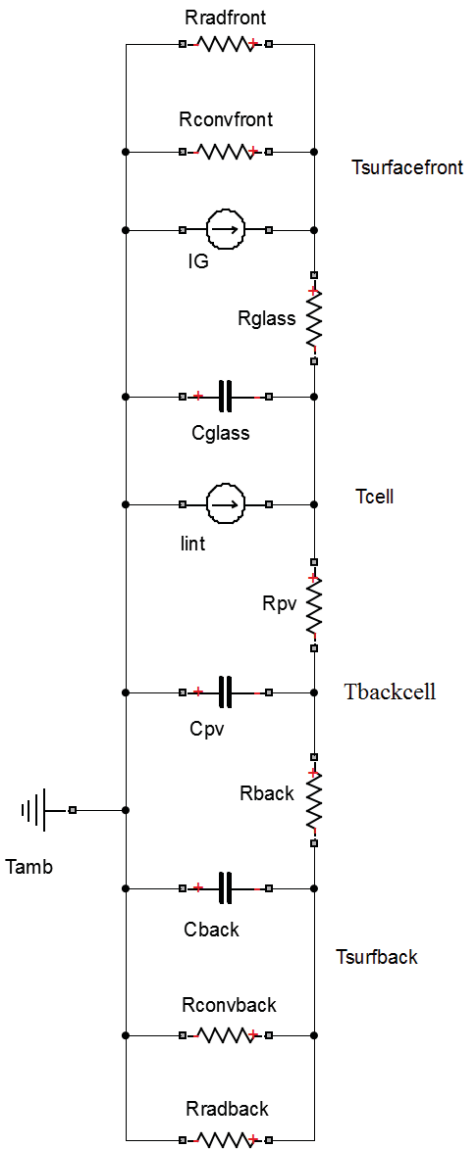

Figure 4.2: Thermal Circuit of a PV panel.

4.3.3 Model under Comsol Multiphysics

4.3.3.1 Building the model

In this section we would like to assess the effect of the operating voltage on PV panels temperature. We use a finite element analysis software: COMSOL Multiphysics. We build a panel consisting of 36 (4×9) cells. Each cell is $12.5cm \times 12.5cm$. A distance of 2 cm separates two adjacent cells (see figure 4.3). The panel is constituted of three layers: the glass 0.3cm, the PV cell (cell, ARC, and EVA) 0.2cm, and the backsheet 0.2cm. Under STC the panel can deliver 5.5A.

The heat transfer (The Heat Transfer with Surface-to-Surface Radiation) physic module is used. A

heat flux on the front surface models the incident irradiance. Convective heat flux is added to the front, back, and edge surfaces. Surface-to-Ambient Radiation is added to the front and back surfaces with their corresponding emissivity. A negative heat source is added, localized in each cell and modeling the generated electrical energy. Another heat source is added, localized in each cell and modeling the internal generated heat.

A tetrahedral mesh is used. The front surface mesh is shown in figure 4.4; and the internal mesh of the cells layer is shown in figure 4.5. We can see clearly that the mesh is refined near the edges of the cells. It is coarser in the center of the cells.

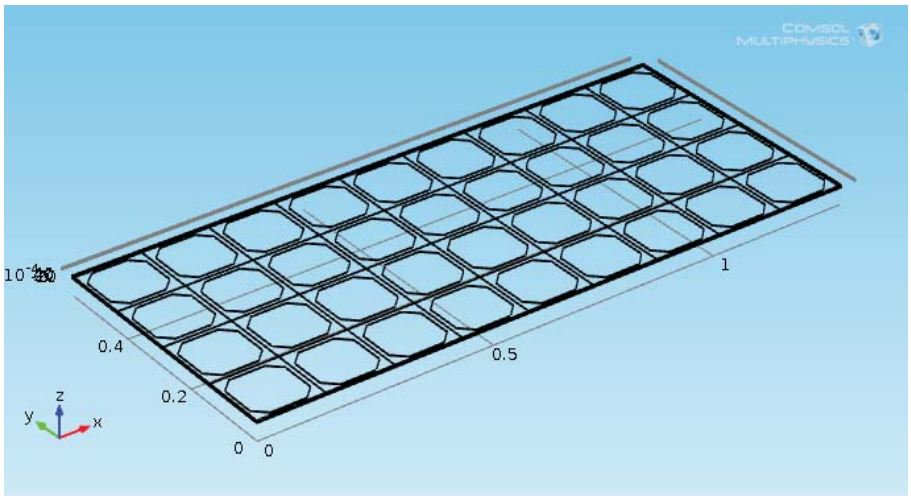

Figure 4.3: Schema of the panel under study.

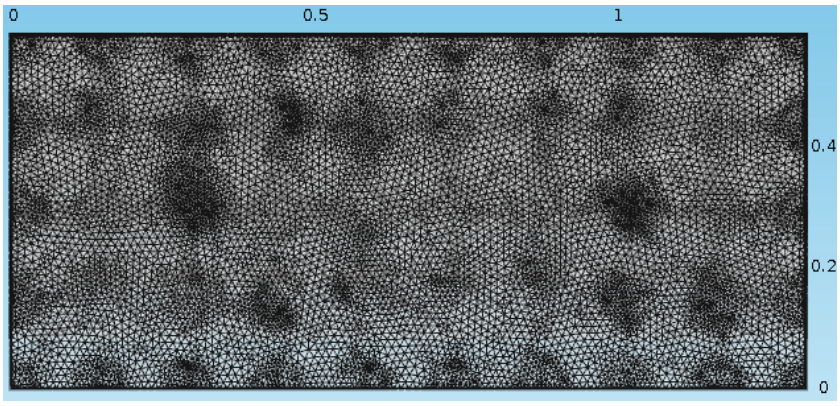

Figure 4.4: Mesh of the thermal model for the front surface.

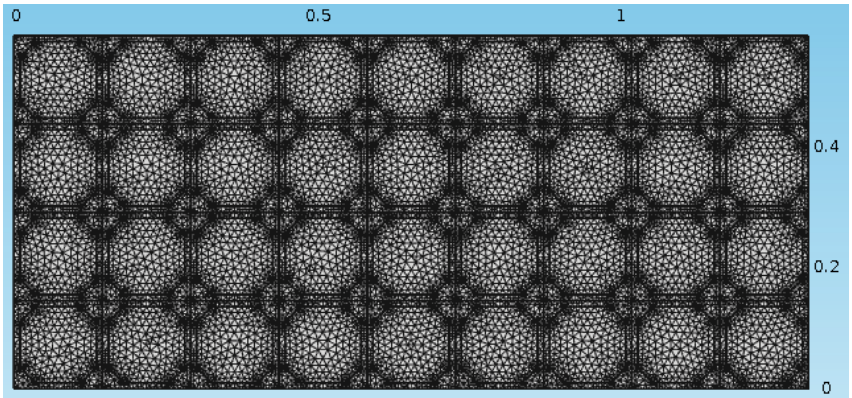

Figure 4.5: Mesh of the thermal model for the cell layer.

Table 4.2: Modeling parameters.

Parameter	Description	Value
d	Dimension of the cell	$0.125m$
dx	Thickness of the cell	$0.002m$
R_{SSTC}	Series resistance in STC	0.075Ω
R_{ShSTC}	Shunt resistance in STC	50000Ω
d_{glass}	Thickness of the glass	$0.003m$
d_{back}	Thickness of the backsheet	$0.002m$
k_{PV}	Thermal conductivity of the cell	$93W.m^{-1}.K^{-1}$
ρ_{PV}	Density of the cell	$2000Kg.m^{-3}$
Cp_{pv}	Heat capacity at constant pressure of the cell	$840J.Kg^{-1}.K^{-1}$
k_{glass}	Thermal conductivity of the glass	$1.4W.m^{-1}.K^{-1}$
ρ_{glass}	Density of the glass	$3000Kg.m^{-3}$
Cp_{glass}	Heat capacity at constant pressure of the glass	$500J.Kg^{-1}.K^{-1}$
$k_{backsheet}$	Thermal conductivity of the backsheet	$0.2W.m^{-1}.K^{-1}$
$\rho_{backsheet}$	Density of the backsheet	$1200Kg.m^{-3}$
$Cp_{backsheet}$	Heat capacity at constant pressure of the backsheet	$1250J.Kg^{-1}.K^{-1}$
k_{copper}	Thermal conductivity of copper	$400W.m^{-1}.K^{-1}$
ρ_{copper}	Density of copper	$8700Kg.m^{-3}$
Cp_{copper}	Heat capacity at constant pressure of copper	$385J.Kg^{-1}.K^{-1}$
$\epsilon_{FrontSurface}$	Emissivity of the front surface	0.9
$\epsilon_{BackSurface}$	Emissivity of the back surface	0.84

4.3.3.2 Simulation results

In the first simulation we consider an irradiance of $1000W.m^{-2}$, an external temperature of 20^oC and a wind speed of $1m.s^{-1}$. The panel is operating at a voltage of $18V$. We show the temperature at the surface of the panel in figure 4.6 . We can see a slight difference in color between the core of the cells and the space between the cells. The cells are hotter than the space between them. This is explained by the fact that cells are a thermal source due to the Joule effect of the series resistance.

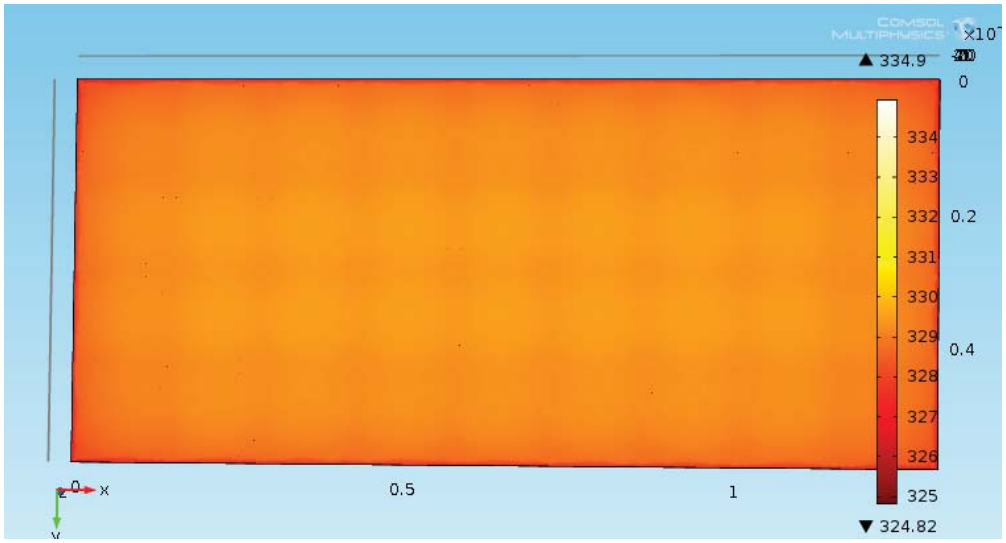

Figure 4.6: Temperature at the surface of the PV panel.

In the second simulation we consider variant environmental conditions. The irradiance is swept from $200W.m^{-2}$ to $1200W.m^{-2}$ and the ambient temperature is swept from 10^oC to 42^oC. The wind speed is fixed to $1m.s^{-1}$ with a pressure of 1 atm. The panel is operating at a voltage of $18.2V$. The cell temperature at the center of the panel is shown in figure 4.7. It is clear that the cell panel temperature increases with the intensity of irradiance and with the ambient temperature. In fact, the irradiance affect the primary or external heat source. And with the increase of ambient temperature, heat dissipation or heat transfer from the panel to the external medium will decrease. The convection heat flux decrease is proportional to the ambient temperature and the radiation heat flux decrease is proportional the ambient temperature at the 4^{th} power.

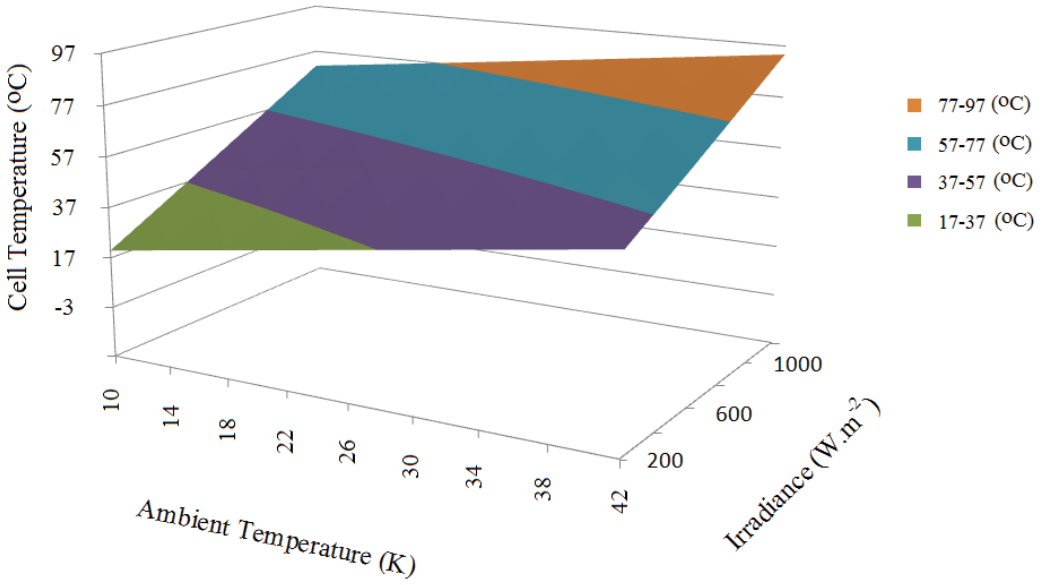

Figure 4.7: Cell temperature with irradiance and ambient temperature variations.

In the third simulation, the ambient temperature is fixed to 20^oC with a pressure of 1 atm. The wind speed is fixed to $1m.s^{-1}$ [70]. The operating voltage is swept from $3V$ to $32V$. The irradiance is fixed to $1000W.m^{-2}$. The temperature is shown for the different points (front surface, cell, and back surface) in figure 4.8. The back temperature is plotted in green, the cell temperature is plotted in blue, and the front temperature is plotted in red. The violet curve represents the electric power generated by the panel.

We can see a difference of about 5^oC between the front and the back surfaces. The temperature of the cell is about 1^oC lower than the temperature of the front surface. We can see clearly that the temperature has a global minimum around $33V$ which is close to the MPP. In reality the minimum temperature occurs when the power driven from panel and the joule effect reaches together a minimum.

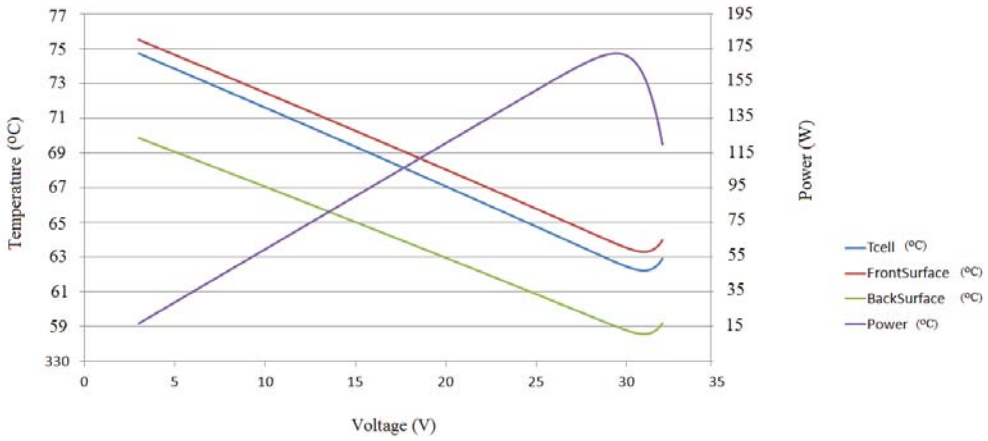

Figure 4.8: Panel temperature for different points with output power as a function of operating voltage.

In figure 4.9 we can see a vertical section of the panel showing the repartition of temperature in the layers of the panels.

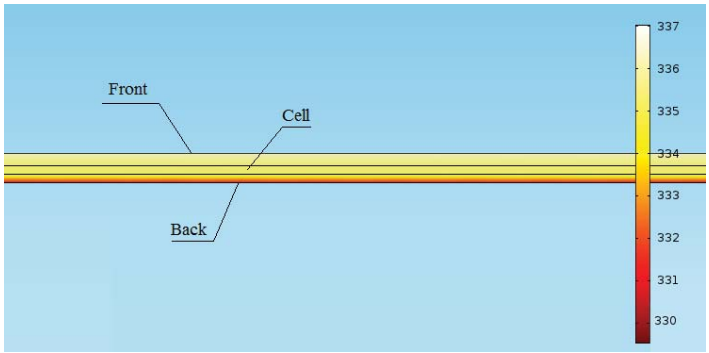

Figure 4.9: Vertical cross section of the panel showing temperature gradient in the panel.

In figure 4.10 we can see the front surface temperature of the panel. We can see a high temperature at the center of the panel and a low temperature near the edges.

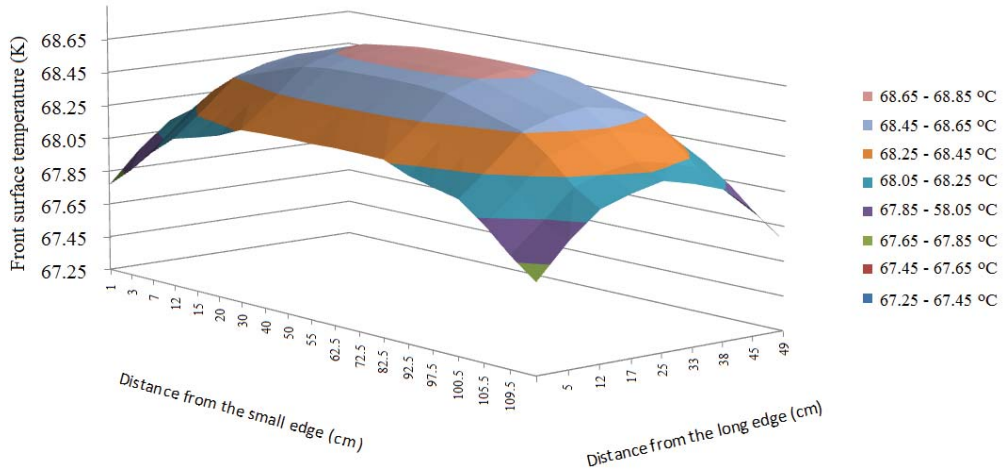

Figure 4.10: Front surface temperature of the PV panel.

In the fourth simulation, we repeat the third simulation with a variant irradiance from $100W.m^{-2}$ to $1100W.m^{-2}$. The temperature of the cell is shown in figure 4.11.

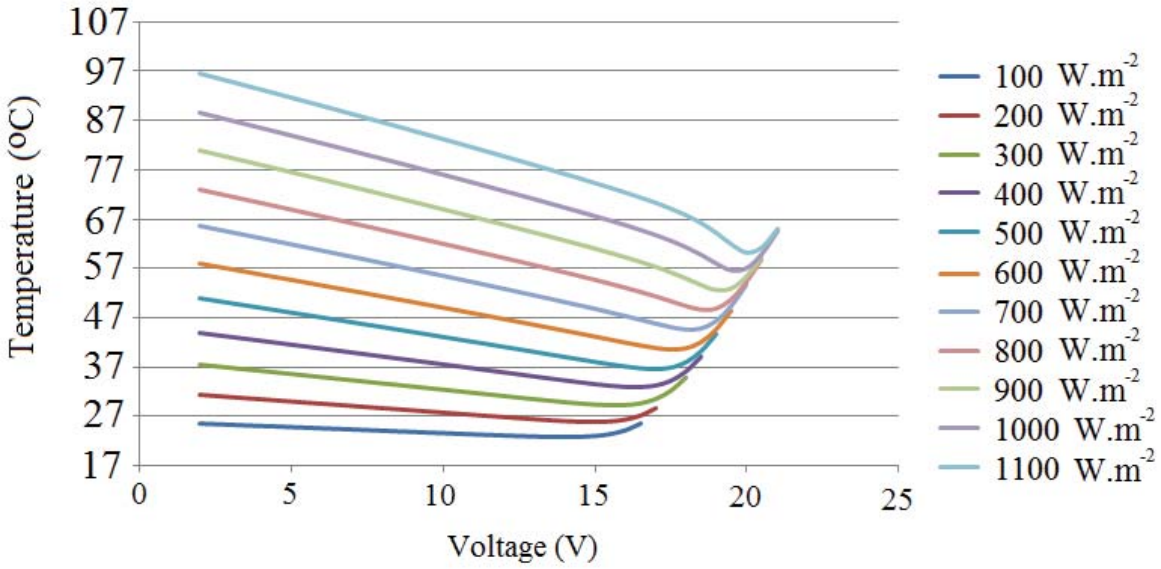

Figure 4.11: Temperature of the cell for as a function of operating voltage for different irradiance levels.

4.3.4 Experimentation

4.3.4.1 In lab experiment

Experimental apparatus: In order to validate the simulation results we built an experimental apparatus that was described in paragraph 3.2.3.1.

Experimental results: The experimentation was conducted in the laboratory room. Where the wind speed is null, the ambient temperature is 21^oC, the pressure is 1 atm, and the relative humidity is 92%. We illuminate the panel with the halogen projectors. The short circuit current is $I_{SC} = 1.6A$. We start varying the operating voltage (From short circuit to open circuit) from 0 to 19.37V and we note the temperature. The results are shown in figure 4.12. They align well with the simulation results. We can see that the minimum temperature occurs at a voltage slightly higher than the MPP.

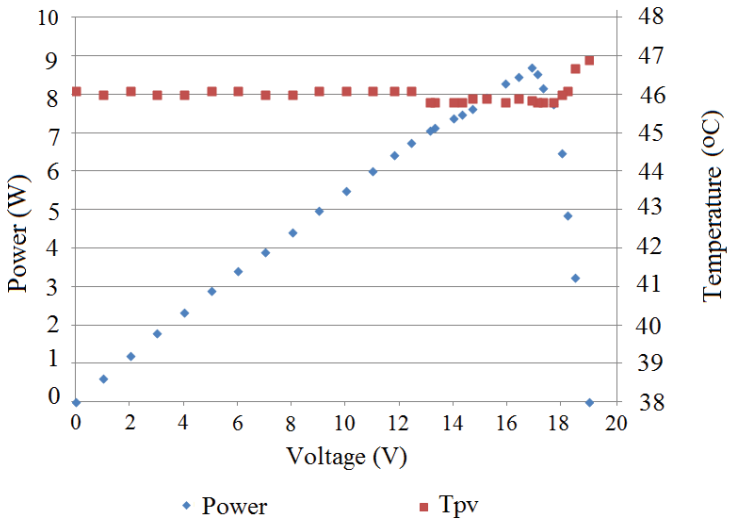

Figure 4.12: Thermal behavior of the PV panel as a function of operating voltage.

A second experimentation was performed with variable wind speed. Two fans were implemented. The ambient temperature is 27^oC, and the relative humidity is 92%. The results show the same thermal behavior. Figures 4.13, 4.14, and 4.15 present the simulation results with low, medium, and high wind speeds respectively. We can see that the temperature of the back of the cell (points in red) is higher than the temperature of the back of the spaces between the cells (points in green). The latter aligns with the simulation results shown in figure 4.6.

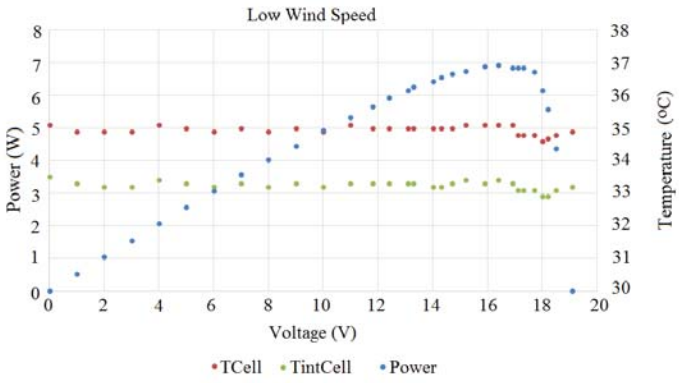

Figure 4.13: Thermal behavior of the PV panel as a function of operating voltage with low wind speed.

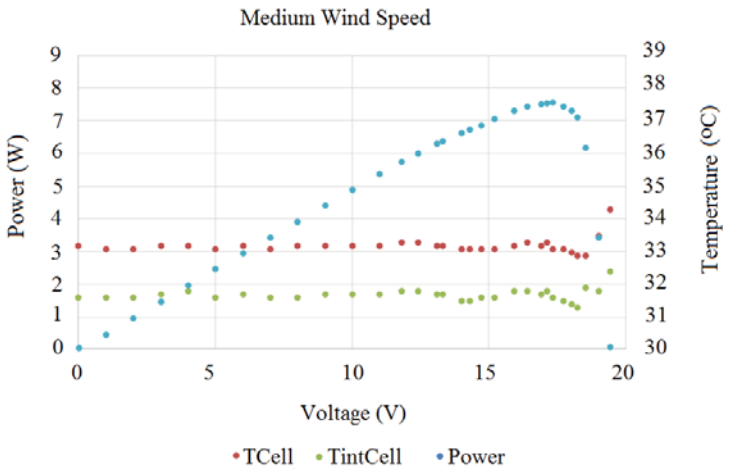

Figure 4.14: Thermal behavior of the PV panel as a function of operating voltage with medium wind speed.

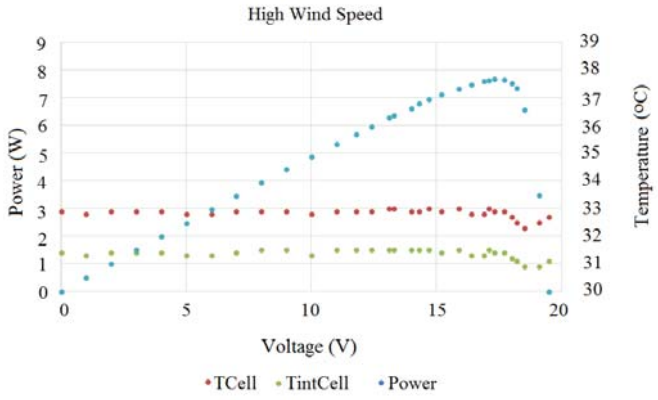

Figure 4.15: Thermal behavior of the PV panel as a function of operating voltage with high wind speed.

4.3.4.2 In Situ

We would like now to test the PV panel under real solar illumination. We mounted the PV panel on a balcony in USEK Kaslik campus, Jounieh Lebanon figure 4.16. In situ and under real external meteorological conditions many issues were encountered. In fact, no weather condition is constant. The wind speed, the solar irradiance, the external temperature, and the relative humidity are all varying parameters that cannot be controlled.

Figure 4.16: PV panel under real solar irradiance.

The temperature of the panel is monitored via a thermal imaging camera. A thermal imaging camera forms an image based on the infrared radiation emitted by a body. A body will generate infrared rays proportionally to the 4^{th} power of its temperature (equation 4.6). A thermography is the resulting thermal image where each temperature is assigned a color. The thermal imaging camera used is the Testo 875 - Thermal imager. It has a temperature range from -20^oC to 280^oC.

In order to record a thermography we must wait around 20 min in order for the temperature to settle up [70]. Many thermographies have been recorded, we present here two relevant ones:

In the first thermography (figure 4.17) we can see the panel under an illumination of $717W.m^{-2}$, an ambient temperature of 30^oC, and a relative humidity of 92%. The panel operates in open circuit conditions. The thermography was recorded on 19-8-2015 at 11:13 AM. It is clear that the temperature of cells regions is higher than the temperature of the inter-cells regions. Figure 4.18 shows the temperature profile of the line P1 drawn on figure 4.17. We can see that the cells temperature is around 1.2^oC higher than the inter-cell temperature.

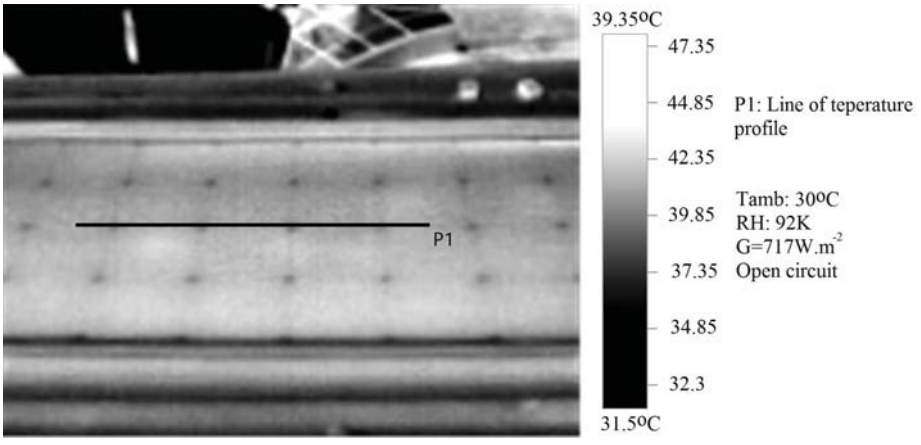

Figure 4.17: Thermography of the PV panel in open circuit conditions.

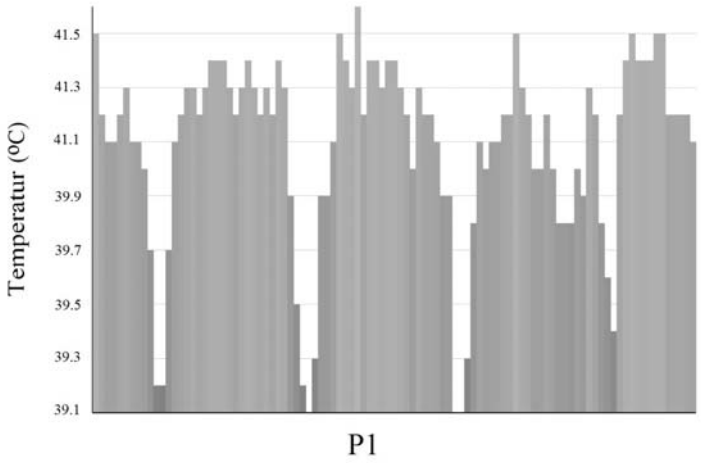

Figure 4.18: Temperature profile of the P1 line.

In the second thermography (figure 4.19), we can see the panel under an illumination of $803W.m^{-2}$, an ambient temperature of 30^oC, and a relative humidity of 92%. The panel operates in MPP condition; We are driving $60W$ from the panel. The thermography was recorded on 19-8-2015 at 11:44. We show the temperature of two points M1 at the center of a cell and M2 at the inte-cell. The same result is recorded.

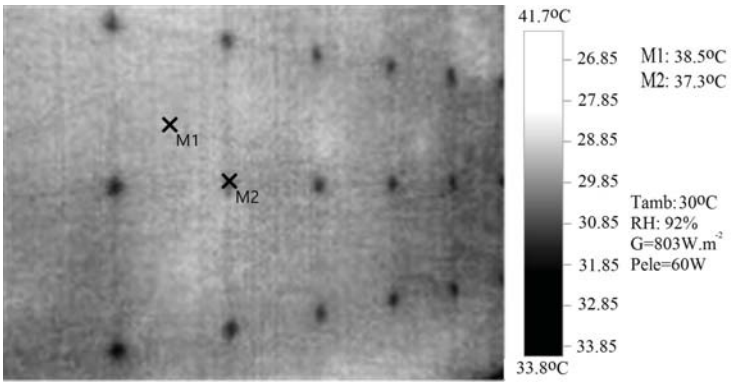

Figure 4.19: Thermography of the PV panel in MPP condition.

The two thermographies (figures 4.17 and 4.19) could not be compared because each one is taken at different irradiance level. But we can see that the MPP thermography presents lower temperature than the open circuit thermography. Knowing that the irradiance is higher during MPP condition, the latter is explained by the fact that $60W$ are being driven from the incoming irradiance and transformed to electrical energy in MPP condition. However, all irradiance power is transformed into heat in the open circuit condition.

4.4 Conclusion

In this chapter we presented a detailed thermal model of PV panels. The model takes into consideration all external and internal heat sources. The model also considers heat dissipation physics that

occur. In this chapter, we also showed that the operating point affects the temperature of the panel. The developed model was validated using the experimental apparatus. The validation was performed in the lab and under real sun in exterior operating conditions.

The most important conclusion of this chapter is the effect of the operational condition on the thermal behavior of PV panels. In addition, we found that the minimum temperature of the panel is observed for a point which voltage is slightly higher than the MPP voltage. The thermal model and the related thermal behavior will be used towards investigating a control algorithm which objective will be to increase the lifespan of the panel.

In chapter 5, we will use knowledge gained from MPPT algorithms (section 1.7) in order to control PV panels in an optimum way striving high energy production and mitigating degradations of PV panels. The utility of MPPT control will be shown in the next chapter.

Chapter 5

Analysis and characterization of faults and degradation mitigation

5.1 Introduction

In this chapter we present our diagnosis and action methods to be used in order to increase the lifespan of PV panels. We start first by presenting the analysis and characterization of faults occurring to PV panels. Then we develop a diagnosis algorithm based on the obtained characterization. The method is based on the aspect ratio of the rectangle formed by the points $(0, 0)$ and (V_{MPP}, I_{MPP}). A clear clustering has been made to detect the fault. In the second part we take knowledge from the thermal model previously developed and from MPPT algorithms in order to develop a method of utilizing PV panels to reduce their degradation effect. We strive to operate the panel at a point where we can get a lower temperature. Lower temperature means less degradation speed and thus an increase in the panel lifespan.

5.2 Characterization of faults

Diagnosis of PV panels is a raising field of interest nowadays. A photovoltaic system does not have moving elements as traditional power generation units, it also does not operate at high temperature. But recent observations showed that PV faults and defaults may lead to undesirable conditions like fire [66]. Faults in PV systems must be determined in order to take actions and limit power loss. In addition, faults may lead to increase fault effects or lead to other faults formation. In previous works, researchers presented basically model-based diagnosis methods in which a residue is generated upon comparing the real value measured from the system and a simulated value generated from the system model [73]. The model will take the same inputs as the real system. According to the residue amplitude a decision, can be made to alert the possible losses. In [74] Chouder et al. analyzed the ratio between the simulated and the measured values of current and voltage. If the ratio is larger than 1, a fault alarm is generated. The faults are faulty modules in a string, faulty string, partial shading, aging, or MPPT error. In [75] Bonsignore et al. studied 6 symptoms of the I-V characteristic to classify the faults between diode short circuit, lower earth fault, upper earth fault, or partial shading. An ANN can be used to determine the type of fault in PV system. The input of the ANN are temperature, V_{MPP}, and I_{MPP}. The ANN outputs one of the fault cases: normal, degraded, short circuited, or shaded. Other methods use a tree-based decision algorithm to determine fault in a PV panel. The two above methods need training and a big amount of data related to normal and faulty conditions [76].

Three main faults studied are the interconnect and connection faults, bridge and earth, and shunt path. We try in this section to develop a detection algorithm that will detect the occurrence of these faults. The algorithm used is based on the variation of the aspect ratio of the rectangle defined by the points $(0, 0)$ and (V_{MPP}, I_{MPP}). The rectangle drawn on the I-V characteristic by the points $(0, 0)$, $(0, I_{MPP})$, (V_{MPP}, I_{MPP}), and $(V_{MPP}, 0)$ represents important data about the operation of the panel (see figure 5.1). In fact, the area of this rectangle represents the maximum electric power that can be

derived from the panel. In addition, the sides of this rectangle represents the current and the voltage derived from the panel. The proposed method will study the difference between the actual PV panel output and a fault free model. The inputs of the model are irradiance and temperature figure (see figure 5.2).

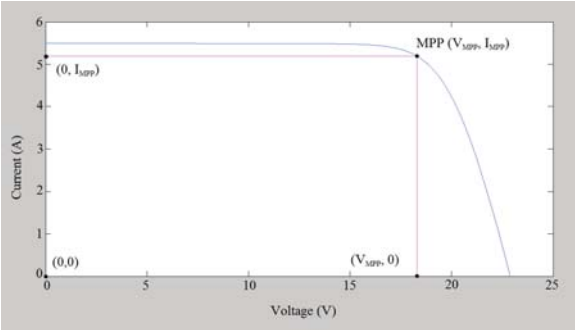

Figure 5.1: Maximum power rectangle.

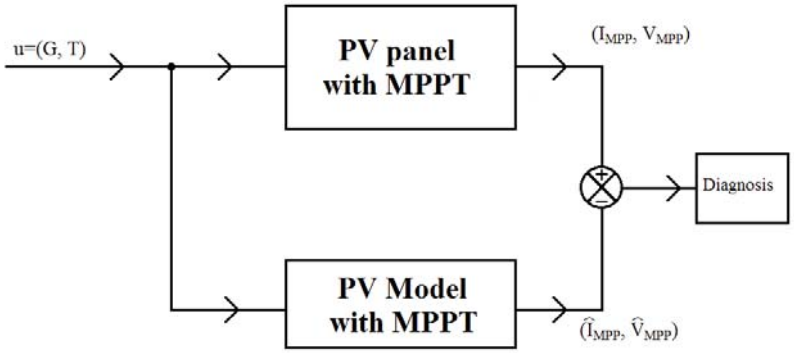

Figure 5.2: Comparison of MPP between PV panel and PV model.

5.2.1 Effect of faults on PV panel

In this paragraph we recall the effect of each fault on the equivalent circuit of the panel and on the I-V characteristic. The interconnect and connection faults affect the equivalent circuit by increasing the series resistance. They also decrease the slope near V_{OC}. The bridge and earth fault decrease the number of the cells in series. They also shift the I-V characteristic to the left proportionally to the number of shorted cells. The shunt path development decreases the shunt resistance of the equivalent circuit. It also increases the slope near I_{SC}.

The common main effect of faults on PV panels resides in decreasing their power output. Faults will also aggravate the situation by increasing the connection resistance due to joule effect. Table 5.1 summarizes the faults and their effects:

Table 5.1: Effect of faults on the equivalent circuit and on the I-V characteristic.

Fault	Effect on I-V curve	Effect on Equivalent circuit
Interconnect and connection faults	Decrease of the slope near V_{oc}, Power decrease	Increase in R_s
Bridge and earth fault	Voltage decrease	Decreases in N_s
Shunt path development	Increase of the slope near I_{sc}	Decrease in R_{sh}

5.2.1.1 Effect of faults on the MPP

As PV panels operate at MPP, we present in this paragraph the effect of PV faults on the MPP. We are interested in understanding how does each fault affect the power reduction of PV panels. More precisely if power loss is caused by a current or a voltage decrease.

Effect of interconnect and connection faults on the MPP: The effect of interconnect and connection faults on the MPP is by decreasing the voltage of MPP more than decreasing its current. The latter is shown in figure 5.3 for different irradiances and different values of the connection resistance R_c. The irradiance ranges from 300 to 1200 $W.m^{-2}$. The connection resistance ranges from 0 to 0.8 Ω, 0 Ω or the fault free panel corresponds to the left most curve.

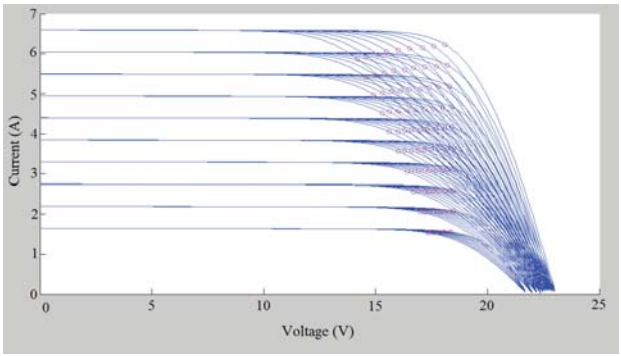

Figure 5.3: Effect of the interconnect and connection resistance on the MPP.

Justification: In order to understand the effect of interconnect and connection faults on the MPP we consider that when we operate at MPP the maximum power is extracted from the panel. In fact, the DC/DC converter is mounted between the load and the panel with the connection resistance (see figure 5.4). When the DC/DC converter works to extract the maximum power to the load (MPPL), the PV panel operates closely to the ideal MPP. We can approximate that $V_{MPP} \approx V_{Rc} + V_{MPPL}$. It means that the measured value of the voltage (V_{MPPL}) that is delivered to the load will be less than the real value of the MPP voltage (V_{MPP}). This is caused by the voltage drop across the connection resistance (R_c). The measured value of the current remains the same, more precisely, it decreases with a lower rate.

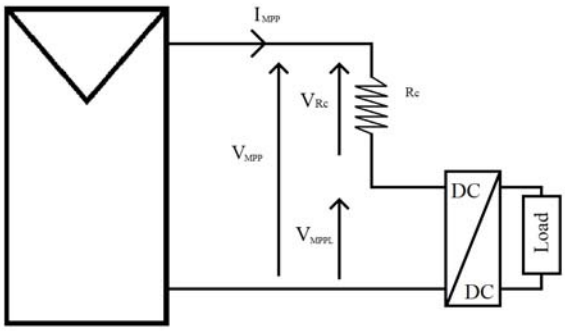

Figure 5.4: Mounting of the PV panel and the DC/DC converter in presence of the connection resistance.

Effect of bridge and earth fault on the MPP: The effect of bridge and earth fault on the MPP is by sharply decreasing the voltage of MPP. The decrease in voltage is proportional to the number of shorted cells. The latter is shown in figure 5.5 for different irradiances and different numbers of shorted cells. The irradiance ranges from 300 to 1200 $W.m^{-2}$. The number of shorted cells ranges from 0 to 26 cells, absence of shorting or the fault free panel corresponds to the left most curve.

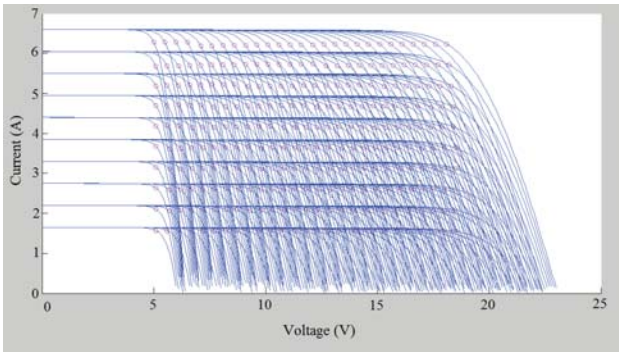

Figure 5.5: Effect of the bridge and earth fault on the MPP.

Justification: In order to understand the effect of bridge and earth fault on the MPP we consider that when we operate at MPP the maximum power is extracted from the remaining panel (see figure 5.6). Which is totally true in this case. In typical cases, when all cells are identical and no mismatch exist, the MPP voltage (V_{MPP}) is equally divided on cells and the same current (I_{MPP}) passes through all cells. When some of the cells are shorted, the voltage decreases proportionally to the number of cells, the current remains the same. In real cases, the voltage decreases and the current may witness some fluctuations. In summary a bridge or earth fault causes a hard decrease in voltage with a little fluctuation in current.

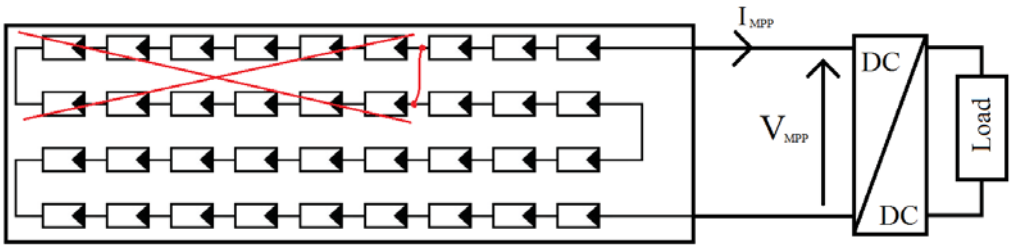

Figure 5.6: Mounting of the PV panel and the DC/DC converter in presence of the bridge fault.

Effect of shunt path development on the MPP: The effect of shunt path development on the MPP is by decreasing the current of MPP more than decreasing its voltage. The latter is shown in figure 5.7 for different irradiances and different values of the shunt resistance R_{path}. The irradiance ranges from 300 to 1200 $W.m^{-2}$. The shunt path resistance ranges from 90 to 1000 Ω, absence of shunt path or the fault free panel corresponds to the left most curve.

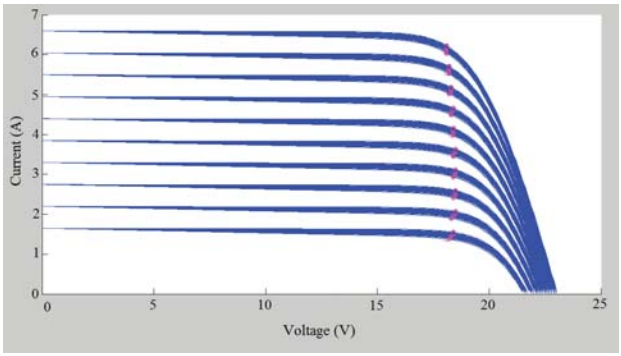

Figure 5.7: Effect of shunt path development on the MPP.

Justification: In order to understand the effect of shunt path development on the MPP we consider that when we operate at MPP the maximum power is extracted from the panel. In fact, the DC/DC converter is mounted between the load and the panel with the shunt path resistance (see figure 5.8). When the DC/DC converter works to extract the maximum power to the load (MPPL), the panel operates closely to the ideal MPP. We can approximate that $I_{MPP} \approx I_{R_{path}} + I_{MPPL}$. It means that the measured value of the current (I_{MPPL}) will be less than the real value of the MPP current (I_{MPP}). However, the voltage remains the same.

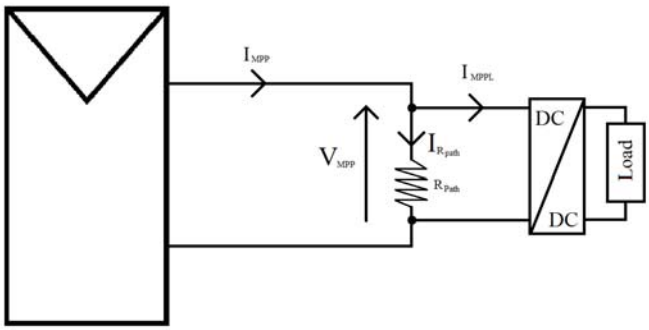

Figure 5.8: Mounting of the PV panel and the DC/DC converter in presence of the shunt path.

5.2.2 Proposed method

The purpose of our method is to identify the faults occurring in PV panels; we try to classify the faults between interconnect and connection faults, bridge and earth fault, or shunt path development. As previously developed, each fault marks the decrease of power with a specified signature: decrease in current or decrease in voltage. Our decision will be based on the variation of the aspect ratio of the rectangle defined by the points $(0, 0)$ and (V_{MPP}, I_{MPP}). The area of this rectangle represents the maximum power extracted from the panel when operating at MPP. We suppose that the panel always operates at MPP; the DC/DC converter is always extracting the maximum power from the panel.

5.2.2.1 Faults signature

In this part we try to obtain each fault signature. We would like to visualize the relative variation in current and in voltage of the MPP in the faulty condition taking the fault free condition as reference. We define two indicators: the relative decrease in current $\%\Delta I$ and the relative decrease in voltage $\%\Delta V$:

$$\%\Delta I = \frac{\hat{I_{MPP}} - I_{MPPL}}{\hat{I_{MPP}}} \tag{5.1}$$

Where:
I_{MPPL}: Real measured MPP current on the load in A.
$\hat{I_{MPP}}$: Estimated MPP current from the PV model in A.

$$\%\Delta V = \frac{\hat{V_{MPP}} - V_{MPPL}}{\hat{V_{MPP}}} \tag{5.2}$$

Where:
V_{MPPL}: Real measured MPP voltage on the load in V.
$\hat{V_{MPP}}$: Estimated MPP voltage from the PV model in V.

The two indicators reflect the early studied approach. Interconnect and connection faults affect the MPP by decreasing the voltage more than decreasing its current. However, bridge and earth fault affects the MPP by sharply decreasing its voltage. Finally, shunt path development affects the MPP by decreasing the current more than decreasing its voltage. In order to visualize the faults' signatures we plot the curves $\%\Delta V = f(\%\Delta I)$ corresponding to the three studied faults figure (see5.9).

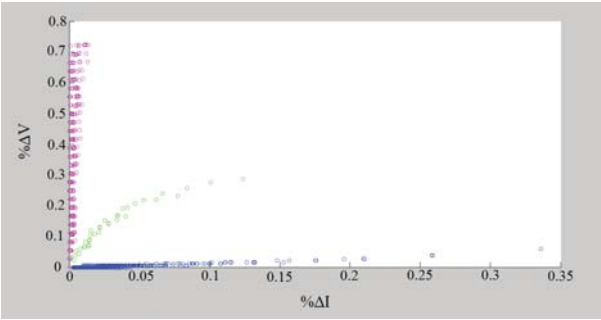

Figure 5.9: $\%\Delta V = f(\%\Delta I)$ curves corresponding to the three studied faults .

We can see clearly in figure 5.9 that the signature of the three faults is clustered in three main regions. The green circles correspond to the interconnect and connection faults where the decrease in voltage is higher than the decrease in current for irradiances ranging from 300 to 1200 $W.m^{-2}$ and connection resistances ranging from 0 to 0.8Ω. The magenta circles corresponds to the bridge and earth faults where the decrease in voltage is highly noted comparing the small or even absence in current decrease. The latter is noted for irradiances ranging from 300 to 1200 $W.m^{-2}$ and the number of shorted cells ranges from 0 to 26 cells. The blue circles correspond to the shunt path development fault where a relative decrease in current is noted comparing to a small or even absence in voltage decrease.

5.2.2.2 Validation

In this paragraph, we intend to validate the faults signatures using real PV panels. We performed multiple experiments with the PV panel in ideal state and in states where we add a series resistor, or a shunt resistor, or we short-circuit some cells. We operate the panel always at MPP. The series and shunt resistor test were performed on the experimental apparatus described in paragraph 3.2.3.1. The bridge test was performed on the experimental apparatus described in paragraph 3.5.2.3.

For each test we measured the current and voltage at MPP ($V_{mppideal}, I_{mppideal}$). When we add the fault resistance we measure the current and voltage at MPP ($V_{mppfault}, I_{mppfault}$). We then calculate $\%\Delta I$ and $\%\Delta V$ according to the following equations:

$$\%\Delta I = \frac{I_{mppideal} - I_{mppfault}}{I_{mppideal}} \tag{5.3}$$

$$\%\Delta V = \frac{V_{mppideal} - V_{mppfault}}{V_{mppideal}} \tag{5.4}$$

The series test was performed for different irradiances ($325W.m^{-2}$, $405W.m^{-2}$, $529W.m^{-2}$) and for different values of the series resistance ranging from 6Ω to 22Ω. We start by measuring the voltage and current at the MPP ($V_{mppideal}, I_{mppideal}$) before applying any fault. Then we add the series resistor with the panel and we operate at MPP. The values of voltage and current ($V_{mppfault}, I_{mppfault}$) are recorded. All values are summarized in table 5.2.

Table 5.2: Summary results of series resistor experiment..

Series Resistance (Ω)	$I_{mppideal}$	$V_{mppideal}$	$I_{mppfault}$	$V_{mppfault}$	$\%\Delta I$	$\%\Delta V$
6	1.064	16.5	1.036	10.87	0.026	0.341
8.5	1.038	16.8	0.909	9.61	0.124	0.427
9	1.005	17	0.893	9.53	0.111	0.439
10	1.005	17	0.834	9.31	0.17	0.452
11	1.005	17	0.756	9.49	0.247	0.441
12	1.005	17	0.719	9.17	0.284	0.460
13	1.005	17	0.641	9.6	0.362	0.435
12	0.726	17.1	0.659	9.68	0.0922	0.433
13	0.726	17.1	0.644	9.32	0.112	0.454
14	0.726	17.1	0.586	9.61	0.192	0.438
15	0.726	17.1	0.536	9.81	0.261	0.426
16	0.726	17.1	0.529	9.48	0.271	0.445
17	0.726	17.1	0.496	9.42	0.316	0.449
14	0.541	16.92	0.507	10.47	0.062	0.381
15	0.54	16.88	0.504	10.07	0.066	0.403
18	0.54	16.88	0.464	9.5	0.140	0.437
19	0.54	16.88	0.434	9.57	0.196	0.433
20	0.54	16.88	0.4	9.95	0.259	0.410
21	0.54	16.88	0.403	9.55	0.253	0.434
22	0.54	16.88	0.392	9.48	0.274	0.438
22.7	0.532	17.19	0.39	9.24	0.462	0.266

The shunt resistor test was performed for different irradiances ($194W.m^{-2}$, $300W.m^{-2}$, $359W.m^{-2}$) and for different values of the shunt resistance (175Ω, 287Ω, 789Ω). We start by measuring the voltage and current at the MPP ($V_{mppideal}, I_{mppideal}$) before applying any fault. Then we add the series resistor with the panel and we operate at MPP. The values of voltage and current ($V_{mppfault}, I_{mppfault}$) are recorded. All values are summarized in table 5.3.

Table 5.3: Summary results of shunt resistor experiment.

Shunt Resistance (Ω)	$I_{mppideal}$	$V_{mppideal}$	$I_{mppfault}$	$V_{mppfault}$	$\%\Delta I$	$\%\Delta V$
287	0.482	17.1	0.429	17	0.109	0.0058
789	0.355	17.3	0.319	17.3	0.101	0
287	0.355	17.3	0.304	17.1	0.143	0.011
175	0.355	17.3	0.284	17.3	0.2	0
789	0.205	17.1	0.182	17.1	0.112	0
287	0.205	17.1	0.156	16.3	0.239	0.046
175	0.205	17.1	0.138	16.7	0.326	0.023

The bridge test was performed for different irradiances ($198W.m^{-2}$, $285W.m^{-2}$, $355W.m^{-2}$) and for different shorted cell assembly (1shorted cell, 2 shorted cells, 3 shorted cells). We start by measuring the voltage and current at the MPP ($V_{mppideal}, I_{mppideal}$) before applying any fault. Then we short some cells and we operate at MPP. The values of voltage and current ($V_{mppfault}, I_{mppfault}$) are recorded. All values are summarized in table 5.4.

Table 5.4: Summary results of bridge experiment.

Number of shorted assemblies	$I_{mppideal}$	$V_{mppideal}$	$I_{mppfault}$	$V_{mppfault}$	$\%\Delta I$	$\%\Delta V$
5	0.0125	19.3	0.0125	16.4	0	0.150
5	0.0095	19.2	0.0094	16.2	0.010	0.156
4	0.0095	19.2	0.0095	12.9	0	0.328
3	0.0095	19.2	0.0095	9.8	0	0.489
5	0.0052	19.4	0.0051	16.2	0.019	0.164
3	0.0052	19.4	0.0051	9.9	0.01	0.489

The calculated $\%\Delta I$ and $\%\Delta V$ of tables 5.2, 5.3, and 5.4 are then plotted in figure 5.10.

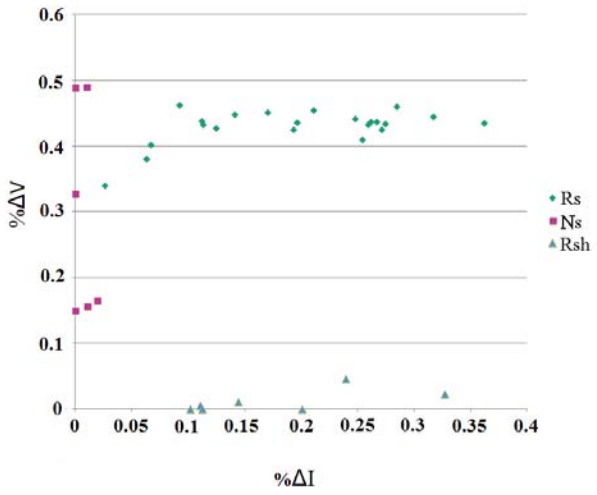

Figure 5.10: Plot of $\%\Delta I$ and $\%\Delta V$ for the three faults.

We can see how the points are clustered in figure 5.10. The green points correspond to measurements done for a series resistor added to the panel. The magenta points correspond to measurements done for shorted cells assembly. And the blue points correspond to measurements done for a shunt resistor added to the panel. The experimental results align well with the simulation results.

5.2.2.3 Diagnosis Algorithm

In order to diagnose the PV panel that presents a decrease in power production we use the above stated deductions. We explicit the three regions of figure 5.9 by fitting three curves. The green region represents a logarithmic shape. The magenta and the blue regions represent linear shapes. Figure 5.11 represents the three regions with their corresponding curves and fitting.

We start by checking if the MPPT algorithm has reached the MPP (relatively stabilized operating voltage). Then we measure the values of G, T, V_{MPPL}, and I_{MPPL}. V_{MPPL} and I_{MPPL} being the actual MPP voltage and current delivered to the load by the DC/DC converter. Using the fault free model of the PV panel we calculate the estimated values of the MPP voltage ($\hat{V_{MPP}}$) and current $\left(\hat{I_{MPP}}\right)$. Then we calculate the faults signatures $\%\Delta I$ and $\%\Delta V$ according to equations 5.1 and 5.2.

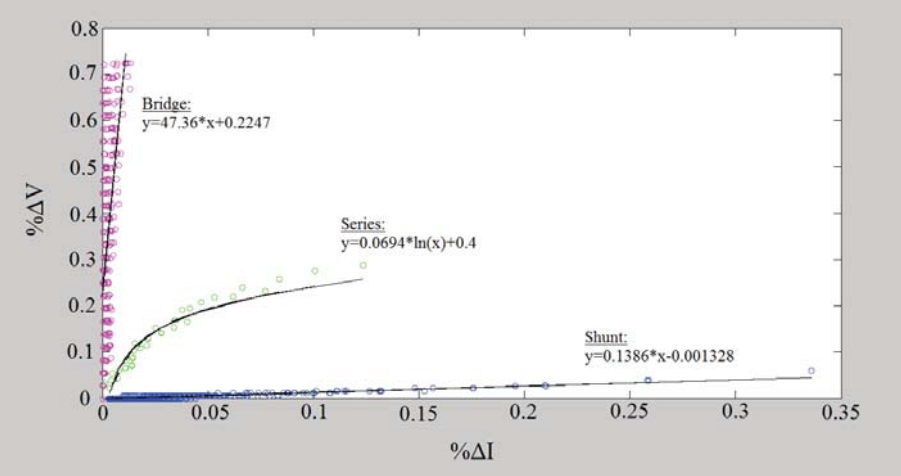

Figure 5.11: Curve fitted regions for diagnosis algorithm.

If the faults signals are low ($\%\Delta I < 0.025$ and $\%\Delta V < 0.07$) we consider that the panel is fault free. Otherwise, we calculate the distance of the point ($\%\Delta I$, $\%\Delta V$) to the three curves. The smallest distance define the belonging of the point to the one of the three regions. An alarm can be generated to indicate the fault occurring to the panel (see figure 5.12).

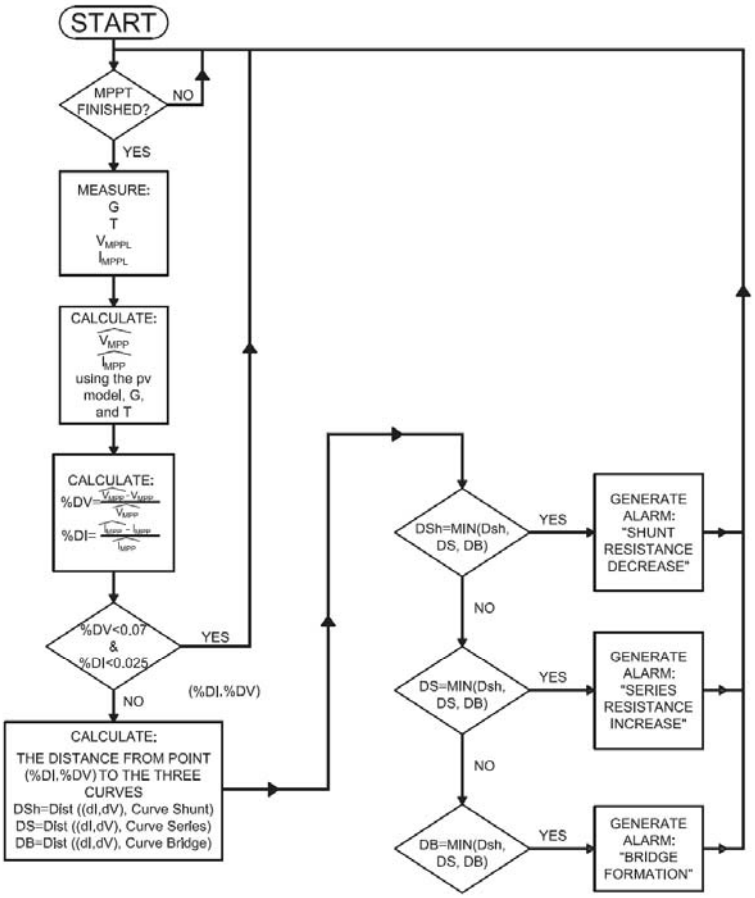

Figure 5.12: Diagnosis Algorithm.

5.2.2.4 Discussion

The proposed algorithm presents simplicity and does not require complex operations as frequency analysis. However, the algorithm presents low performance during low irradiance and when two faults occur at the same time. Note that the latter presents low probability of occurrence.

5.3 Degradation mitigation

In this section we present our preventive actions that must be undertaken in order to increase the lifespan of PV panels via control.

5.3.1 Recall of the effect of temperature on the aging process of PV panels

As previously stated, the degradation modes of PV panels follow Arrhenius equations where the constant rate of degradation is proportional to the exponential of the temperature. The PID follows an Arrhenius equation with an activation energy of 0.94 eV. The LID follows an Arrhenius equation with an activation energy of 0.45 eV. The UVD follows an Arrhenius equation with an activation energy of 0.93 eV. The above encourage us to operate the panel at a lower temperature.

5.3.2 Literature cooling solutions

As known, decreasing the PV panel temperature results in increasing the power output [77] and decreasing the degradation rate [78]. In literature researchers have used several ways to decrease the operating temperature of PV panels. Teo et al. used forced air convection into an air duct installed at the back of the PV panel. They used two blowers to force air into the duct. They reached a decrease in temperature of 11^oC at $1000W.m^{-2}$ and an increase in efficiency of efficiency of $4-5\%$ [79]. Chen et al. used small PV cells embedded in vacuum tubes where R134a refrigerant was used to cool the cells. An increase of 1.9% in efficiency was recorded [80]. Yang et al. used back mounted water tubes to extract heat from PV panels. Functionally graded material was used to connect the tubes to the back of the panel. The authors recorded an increase of 1.5% in efficiency and a decrease of 10^oC in operating temperature [81]. Rosa-Clot et al. developed the TEPSI panel, where water can flow on the top of the PV panel. In this case, infrared light is absorbed by water and useful photons are transmitted to the cell [69]. These traditional PVT (Photovoltaic Thermal hybrid collector) require additional hardware (tubes, pumps, glass...). They also produce heat than can sometimes be unuseful (in the desert for example). They also need a cooling fluid that sometimes may be hard to elaborate in rural and deserted regions. In our approach we propose a control algorithm that can be applied to the system needing only a temperature sensor. The approach will be presented later in this chapter.

5.3.3 Real-Time simulation model with thermal behavior

In this part, we include the thermal model of PV panels in the previously developed real-time model (Paragraph 3.4). The general dynamic equation of heat transfer is given by equation 5.5:

$$\sum \dot{Q} = m \times C \times \Delta T \tag{5.5}$$

Where:
$\sum \dot{Q}$: Sum of all heat fluxes in W.
m: Mass in kg.
C: Thermal capacity in $J.Kg^{-1}.K^{-1}$.
T: Temperature in K.

$$\sum \dot{Q} = \dot{Q_{sun}} + P_j - P_{ele} - \dot{Q_{conv}} - \dot{Q_{rad}}$$

$$\sum \dot{Q} = G \times A \times 0.95 + n \times R_s \times I^2 + n \times \frac{\left(\frac{V}{n} + R_s \times I\right)^2}{R_{sh}} - V \times I$$
$$- h \times A \times (T_{amb} - T_{pv}) - \epsilon_f \times \sigma \times A \times \left(T_{amb}^4 - T_{pvs}^4\right) - \epsilon_b \times \sigma \times A \times \left(T_{amb}^4 - T_{pvs}^4\right) \quad (5.6)$$

Where:
ϵ_f: Emissivity of the front surface.
ϵ_b: Emissivity of the back surface.
ΔT in equation 5.5 represent the temperature change. Using 5.6 it can be expressed as a function of external and operational conditions. The real-time simulation model can now represent a real PV panel which degradation rate can be changed by change in operational conditions. Moreover, a change in operational conditions will lead to a change in temperature.

5.3.4 Maximum Lifetime Point

We define the MLP (Maximum Lifetime Point) as the point where the PV panel operates at its minimum temperature. Recalling the thermal model previously developed, the MLP can be found at the right side of MPP. It corresponds to higher voltage. Figure 5.13 shows the power curve with its corresponding MPP and the temperature curve with its corresponding MLP.

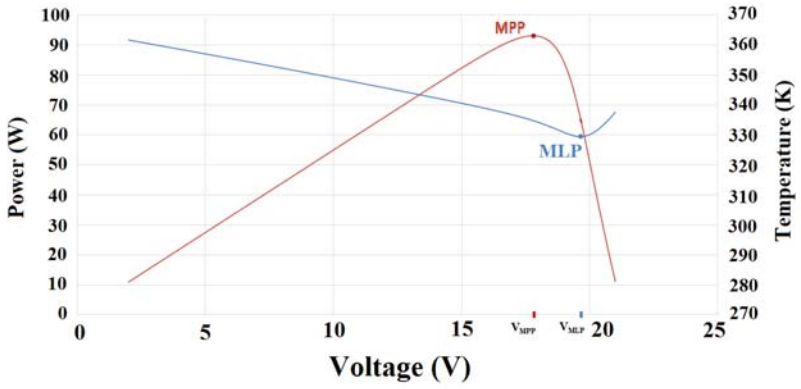

Figure 5.13: Power and temperature curves with MPP and MLP.

5.3.5 Tracking the MLP

We start first by understanding the thermodynamic physic behind the MLP. The dynamic equation of heat transfer given by 5.6 can be divided into the following:

$$\sum \dot{Q} = \dot{Q_{sun}} + P_j - P_{ele} - \dot{Q_{conv}} - \dot{Q_{rad}}$$

$$\sum \dot{Q} = G \times A \times 0.95 + n \times R_s \times I^2 + n \times \frac{\left(\frac{V}{n} + R_s \times I\right)^2}{R_{sh}} - V \times I$$
$$- h \times A \times (T_{amb} - T_{pv}) - \epsilon_f \times \sigma \times A \times \left(T_{amb}^4 - T_{pvs}^4\right) - \epsilon_b \times \sigma \times A \times \left(T_{amb}^4 - T_{pvs}^4\right)$$
$$\sum \dot{Q} = \dot{Q}_1 + \dot{Q}_2 + \dot{Q}_3 \quad (5.7)$$

$$\dot{Q_1} = \dot{Q_{sun}} = G \times A \times 0.95 \tag{5.8}$$

is the incident irradiation that cannot be controlled.

$$\dot{Q_2} = -\dot{Q_{conv}} - \dot{Q_{rad}} = -h \times A \times (T_{amb} - T_{pv}) - \epsilon \times \sigma \times A \times \left(T_{amb}^4 - T_{pvs}^4\right) \tag{5.9}$$

is the convection and radiation heat fluxes that depend directly on the temperature of the panel. These fluxes depend indirectly on the operation point of the panel but present complexity and low effect.

$$\dot{Q_3} = P_j - P_{ele} = n \times R_s \times I^2 + n \times \frac{\left(\frac{V}{n} + R_s \times I\right)^2}{R_{sh}} - V \times I \tag{5.10}$$

is the internal heat sources and the converted electrical power. These fluxes depend directly from the operation point, as they depend on V and I. Our approach is to operate at the point where $\dot{Q_3}$ is at its minimum value every time.

We start by plotting the flux $\dot{Q_3}$ as a function of the operating voltage. In the same graph we plot the generated power. We can see in figure 5.14 the MPP and the MLP. The latter corresponds to the minimum value of the heat flux $\dot{Q_3}$. Our goal is to operate the panel at the MLP in order to decrease its temperature. $\dot{Q_3}$ presents a nonlinear behavior. In figure 5.15 we present the breakdown $\dot{Q}3$ flux. We can see separately the heat generated by R_s and R_{sh} and the extracted electrical power. The heat caused by R_{sh} presents low variation and negligible value. The heat caused by R_s presents high values for low voltages and decreases with voltage. The electrical power generated (that acts as a heat sink to the thermal model) presents a minimum point that corresponds to the MPP. When adding the three curves, we obtain the nonlinear blue curve of figure 5.14.

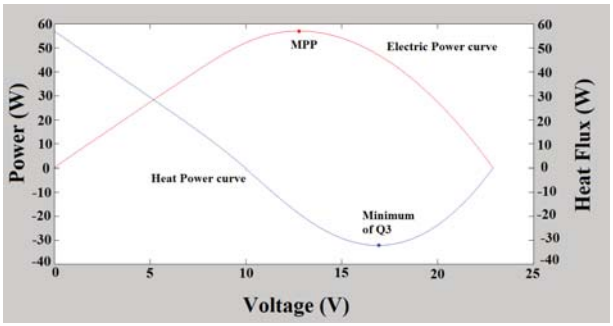

Figure 5.14: Electric power and $\dot{Q}3$ heat flux.

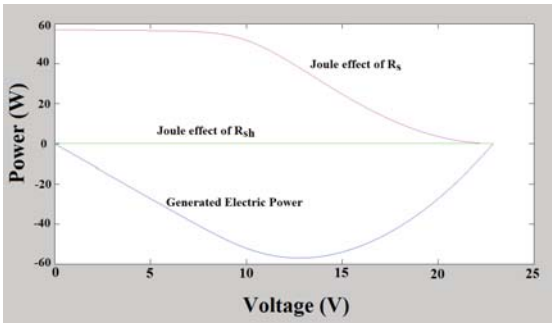

Figure 5.15: $\dot{Q}3$ heat flux breakdown.

5.3.5.1 Applying MPPT technique to track the MLP

In this paragraph, we would like to operate our panel on the MLP. The task is similar to operating the panel at the MPP. We would like to fix our operating point at the point where the temperature becomes minimal in another meaning where $\dot{Q_3}$ becomes minimal. $\dot{Q_3}$ has a one global minimum (MLP) that is defined by:

$$\frac{d\dot{Q_{3MLP}}}{dV} = 0 \tag{5.11}$$

At the left of the MLP, $\frac{d\dot{Q_3}}{dV} < 0$ at the right of the MLP $\frac{d\dot{Q_3}}{dV} > 0$. A PO algorithm can be used. If the value of the $\dot{Q_3}$ slope has a negative value, we must increase the operating voltage. If the value of the $\dot{Q_3}$ slope has a positive value, we must decrease the operating voltage. Figure 5.16 shows the MLPT algorithm.

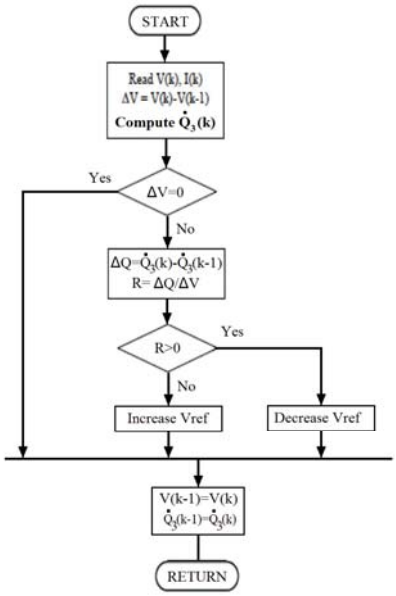

Figure 5.16: Flowchart of the PO algorithm applied for MLPT.

5.3.5.2 High Level control

When tracking the MLP, the panel generates less power than the maximum power. The latter represents a major drawback. We must gain the importance of the MPPT to extract the maximum power from the PV panel and we must gain the importance of the MLPT to increase the lifespan of the PV panels. Reviewing the Arrhenius equations that define the degradation speed of PID, LID, and UVD we plot the reaction rate of PID, LID, and UVD with only their dependency on temperature in figures 5.17, 5.18, and 5.19. We can see clearly that the average slope of the curve between 60^oC and 85^oC is one order of magnitude higher than the average slope between 17^oC and 60^oC.

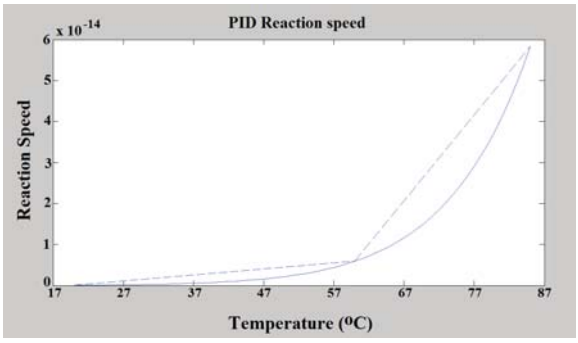

Figure 5.17: Reaction speed dependance on temperature for PID.

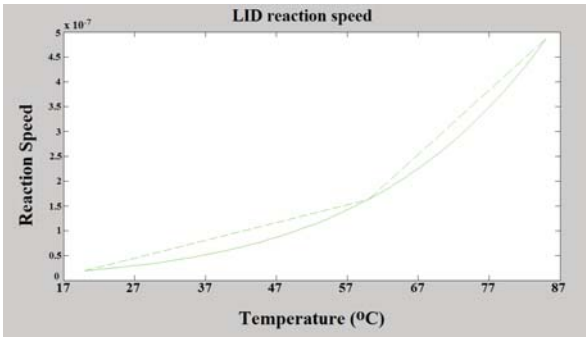

Figure 5.18: Reaction speed dependance on temperature for LID.

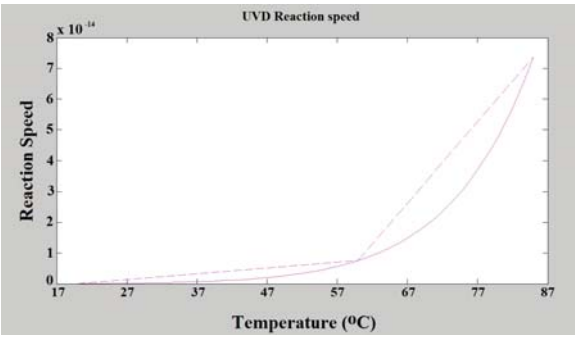

Figure 5.19: Reaction speed dependance on temperature for UVD.

Table 5.5: Average slope of degradation speeds.

Degradation mode	Average slope [17, 60]	Average slope [60, 85]
PID	$1.4627e-16$	$2.0958e-15$
LID	$3.5967e-09$	$1.2914e-08$
UVD	$1.8828e-16$	$2.6462e-15$

The above leads to the following statement: reducing the temperature for one degree in the [60, 85] range will mitigate the degradation process 10 times (more or less) than reducing the temperature for one degree in the [17, 60] range. In order to perform our algorithm, we need to monitor the temperature (T_{pv}) which becomes an input to the control system. The applied algorithm is shown in figure 5.20. In order to reduce the oscillation between MLPT and MPPT, a toggling is defined by a hysteresis function. MLPT starts when the panel's temperature reaches 60^oC. Switching back to the MPPT requires that the temperature falls lower than 59.5^oC (see figure 5.21).

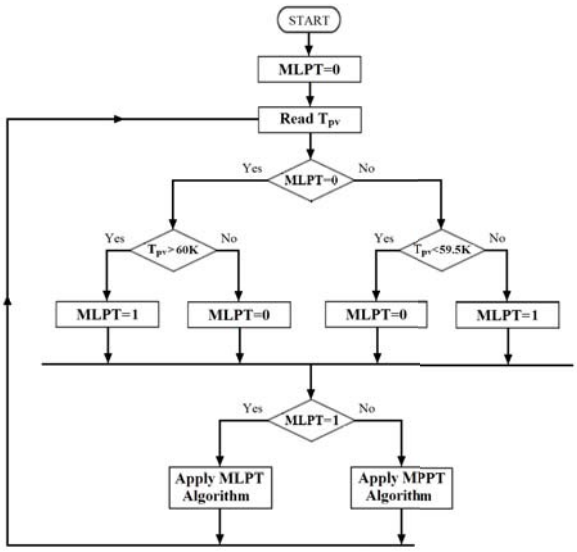

Figure 5.20: Flowchart of the high level control.

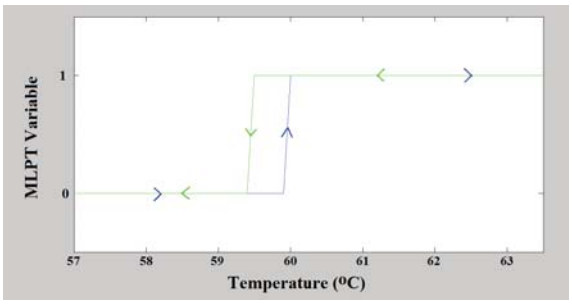

Figure 5.21: Hysteresis toggling between MLPT and MPPT.

5.3.6 Simulation results

We applied our MLP algorithm for the previous modeled monocrystalline $100W$ PV panel. The panel model takes into account all the degradation modes with all the environmental and operational parameters affecting their magnitude. We choose an average irradiance of $709W.m^{-2}$, an average ambient temperature of 28^oC, and an average relative humidity of 50%. We start by showing the temperature of the panel T_{pv} for the 10^{th} day of operation in figure 5.22. Then we show the temperature of the panel T_{pv} for the 1000^{th} day of operation in figure 5.23. After, we show the power produced for the 1000^{th} day of operation in figure 5.24. Then we show the normalized efficiency for all the 40 years of operation of the panel in figure 5.25. We also plot the operating voltage of the panel for the 10th day in figure 5.26. At the end, we show the energy production for the 40 years of operation in figure 5.27. For all the simulation results, the curves in blue represent the simulation using the MPPT algorithm and the curves in magenta represent the simulation using the MLPT algorithm.

In figure 5.22, the temperature of the panel is shown for all the 10^{th} day of operation. The temperature rises and falls down, it lags the ambient temperature due to the thermal capacitance of the panel. We can see in the left magnification that a small decrease of temperature is achieved when applying the MLPT algorithm. We can see also in the right magnification that the temperature starts differing between the blue and the magenta curves when the temperature of the panel reaches $60K$.

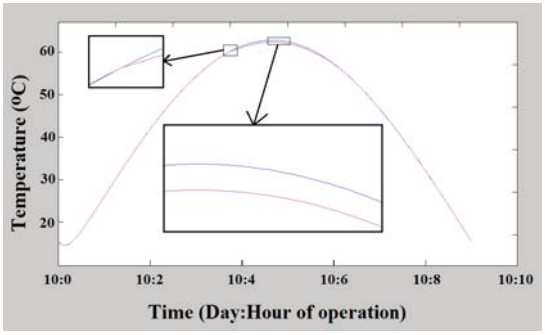

Figure 5.22: Temperature of the panel for the 10^{th} day.

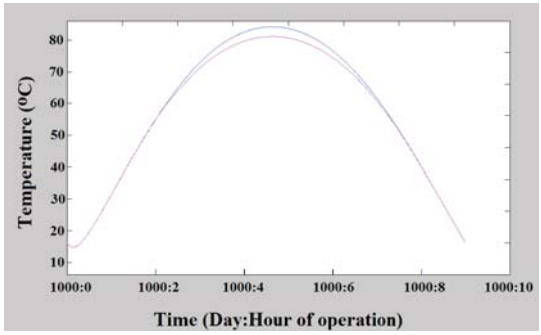

Figure 5.23: Temperature of the panel for the 1000^{th} day.

In figure 5.23, the temperature of the panel is shown for all the 1000^{th} day of operation. We can see the high temperature decrease when we apply MLPT algorithm. This is due to the fact that the degraded panel (in blue) will heat up more than the less degraded panel (in magenta).

During the operation for the 40 years, a maximum temperature of 85^oC has been recorded for the degraded panel. And a maximum temperature of 82^oC has been recorded for the less degraded panel.

In figure 5.24, we can see the power produced during the 1000^{th} day. The power produced by the degraded panel (in blue) is $4W$ lower than the power produced by the less degraded panel (in magenta). Two reasons are behind this fact. First is that the degraded panel has a lower efficiency (in STC) than the less degraded panel; it has been working on higher temperatures for the past 999 days. Second, the actual operating temperature at of the degraded panel is higher than the actual operating temperature of the less degraded panel and temperature decreases the efficiency of the panel.

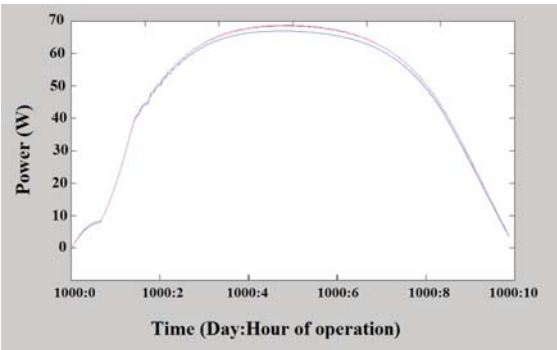

Figure 5.24: Power of the panel for the 1000^{th} day.

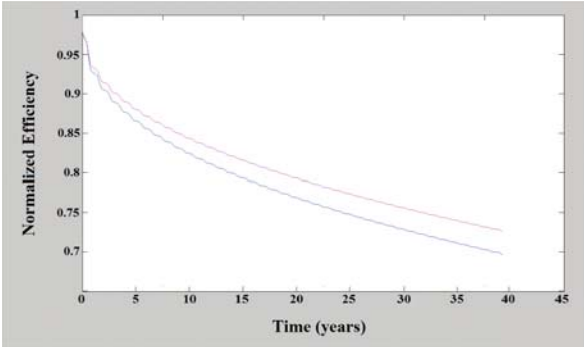

Figure 5.25: Normalized efficiency over 40 years.

In figure 5.25, we can see the normalized efficiency of the two panels. The degraded panel (in blue) and the less degraded panel (in magenta). We can clearly observe that when applying our control strategy, the efficiency of the panel is maintained higher. We also see that the efficiency of the less degraded panel at 40 years is almost the same of the degraded panel at around 25 years. The latter proves that we achieved to increase the lifespan of PV panels up to 40 years.

In figure 5.26 we show the operating voltage of the panel for the MPPT and the MLPT algorithms for the 10^{th} day. When the temperature of the panel reaches 60^oC the algorithm of the less degraded panel switches to the MLP operation. And we see a higher operation voltage. When the temperature reaches back 59.5^oC the control goes back to the MPP.

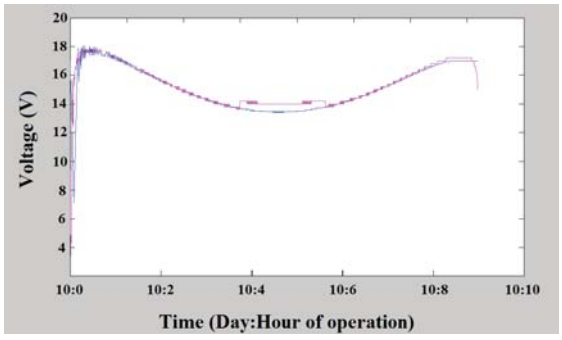

Figure 5.26: Operating voltage of the panel for the 10th day.

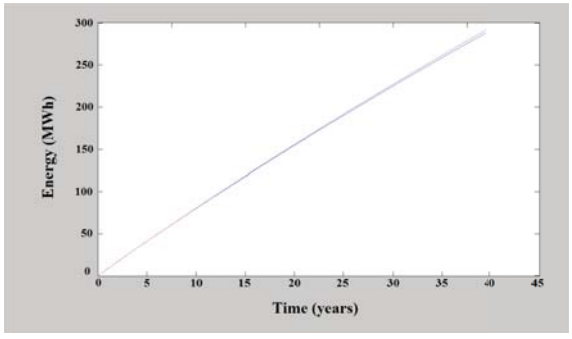

Figure 5.27: Energy produced for around 40 years of operation.

In figure 5.27, the energy produced by the two panels is shown for 40 years of operation. The degraded panel (in blue) produced $287MWh$ in 40 years. The less degraded panel (in magenta) produced $291MWh$ in 40 years. We can see an increase in energy production due to our control

MLPT algorithm. By looking at the energy curve, we see a wavelet shape specially at the first 4 years of operation. This shape is due to the fact that summer seasons produce more power that winter seasons. We can also see that the slope of the first years is higher than the slope of the later years. This is due to the degradation process of PV panels that decreases power production with time.

We know apply our approach for different irradiances and different ambient temperatures. The simulation results are shown in table 5.6. When the control approach is Yes it means that we are applying our algorithm to decrease the degradation rate of PV panels. When the control approach is No it means that old MPPT algorithm is used all the time. We can see that for the same weather conditions the efficiency of the system is increased when applying our control approach. The efficiency at 40 years of the panels with our control approach is nearly equal to the efficiency at 25+ years of the panels without our control approach. The latter proves that we succeeded in reaching our objective. In addition, we can see the difference in energy production between the panels with the control approach and the panels without the control approach. This difference in energy production increases with the increase of ambient temperature.

Table 5.6: Simulation result for different irradiances and temperatures.

Irradiance ($W.m^{-2}$)	Temperature (^oC)	Relative Humidity (%)	Control approach	Energy at 40 years	Efficiency at 25+ years	Efficiency at 40 years
709	28	50	No	2.8798×10^8	0.73	0.69
709	28	50	Yes	2.9124×10^8	0.76	0.72
709	30	50	No	2.8002×10^8	0.71	0.67
709	30	50	Yes	2.8400×10^8	0.74	0.7
709	32	50	No	2.7126×10^8	0.68	0.64
709	32	50	Yes	2.7626×10^8	0.71	0.67
800	35	50	No	2.5821×10^8	0.63	0.6
800	35	50	Yes	2.6381×10^8	0.67	0.64

5.3.7 Discussion

By applying our control algorithm, we succeeded in generating more energy from the same panel. Although the MLPT algorithm strives the panel to operate at a point generating less power than the MPP the degradation process of the panel has been reduced. As the panel operates at a lower temperature, the degradation speed is reduced. We also noticed that the more the panel degrades the more it heats up. This is explained by the fact that the series resistance R_s increases, generating more heat with the current passing through. Besides, the shunt resistance R_{sh} decreases, increasing the shunt current and the heat generated.

5.4 Conclusion

In this chapter, we presented our proposed diagnosis and actions used to increase the lifespan of PV panels. The diagnosis algorithm analyzes the decrease in power. It can classify the faults by studying the source of power decrease, whether this decrease comes from a decrease in voltage or a decrease in current. Three clusters are created for the interconnect and connection faults, bridge and earth, and shunt path development faults. The diagnosis algorithm is based on the change of the aspect ratio of the rectangle formed by the points $(0, 0)$ and (V_{MPP}, I_{MPP}).

In order to mitigate the degradation of PV panels, we defined a new operating point of PV panels; the MLP. This point is characterized by operating the panel at a minimum temperature. As temperature is the major parameter affecting the degradation speed and as temperature affect the degradation rate following an Arrhenius equation, choosing to reduce the operating temperature is a key solution

towards increase in the PV lifespan. By operating the panel at the MLP during temperature higher than $60K$ we ended by increasing the power production of the panel over a 40-years operation duration.

General Conclusion

In this report we presented our PhD research between the Ecole Polytechnique de l'Université d'Aix-Marseille (AMU) and the Faculty of Engineering of the Holy Spirit University of Kaslik (USEK). Our main interest is to increase the lifespan of PV panels. The latter is achieved by an appropriate control of PV panels defining a way of use to always be in good operation.

Context

The thesis was held in co-direction between l'Ecole Polytechnique of the Aix-Marseille Université (AMU) and the Faculty of Engineering of the Holy Spirit University of Kaslik (USEK). The thesis was supervised at Polytech Marseille by Professor Nacer K. M'SIRDI, head of SASV project at LSIS UMR CNRS 7296. It was also supervised at the Faculty of Engineering (USEK) by Dr. Eng. Tilda Karkour Akiki, head of the Electrical and Electronics Engineering Department. This thesis is included in the HyRES Lab and the RMEI network. This PhD project carried many benefits on the research and development relations levels between the two institutions. Indeed, this partnership initiated research in the axis of renewable energy within USEK.

This thesis was also conducted in parallel to other thesis at the SASV project team. We enumerate the thesis of Miss Mouna Abarkan, the thesis of Mr. Motaz Amer, and the thesis of Mrs. Rana Ahmed. The cooperation between the SASV project team of the LSIS and the Faculty of Engineering of USEK led to a Mobility Scholarship granted by the AUF (Agence Universitaire de la Francophonie). In addition, a research grant has been given to the project by the HCR (Higher Center for Research) of USEK.

The works on the MPPT (Maximum Power Point Tracking) algorithms, reported in chapter 1, were in cooperation between USEK, LSIS, and MIS (Modélisation, Information & Systèmes) laboratory of the Université de Picardie Jules Verne.

Summary

We started first by defining and describing degradation modes and faults that occur to PV panels. We realized that temperature is a common parameter to degradation modes and faults. The developed thermal model of PV panels showed a critical operational point where the temperature of the panel reaches a minimum. This point has been defined as the MLP. It is situated at the right of the MPP on the I-V characteristic. A good control algorithm has been developed where we operate at the MPP and we switch to the MLP when the temperature of the panel increases. Positive results have been noticed via an increase in power production and a mitigation in degradation process.

In chapter 1 we presented general information concerning PV panels. We also surveyed existing types of PV panels, their operation principles, utility, features, efficiency, and applications. In addition, we presented the work done on MPPT algorithms that were conducted alongside to the PhD work. This chapter helps to understand the operation of PV panels and presents a solid base that has been used in chapter 5.

In chapter 2 we surveyed the degradation modes and faults of PV panels. Degradation modes lead to a continuous decrease in efficiency, and faults occurring to panels lead to a sudden decrease in power production.

In Chapter 3 we showed our main contribution in this project. We developed a PV model that takes into consideration its degradation modes and a real-time simulation model that presents the variation of the equivalent circuit of the PV panel as a function of time. In addition, faults modeling is also presented. Model validation using real hardware is presented to ensure a good representation of the real panel.

In chapter 4 we developed a thermal model of PV panels. Thermal behavior of PV panels is explained and modeled giving new findings. The model is validated with real hardware.

In chapter 5 we presented our faults characterization and control actions necessary to increase the lifespan of PV panels. The diagnosis algorithm identifies faults occurring to PV panels and helps maintaining the system. Our actions mitigate the degradation process of PV panels and increase their energy production.

Perspectives and future works

We are living now in the rising edge of RES. RES can and must present serious solutions to the world increasing need of energy and the depletion of fossil resources. The achieved work in this research project can open the floor to many projects related to control engineering applied to RES. Future works are being carried with the participation of different teams from different countries (France, Spain, Italy, Greece, Lebanon, Egypt, Morocco). All teams are gathered within the HyRES lab and the RMEI. In addition, a collaboration for delivering a double diploma in master of electrical engineering is being prepared between AMU and USEK. We project our future works on short-term perspectives and long-term perspectives.

Short-term perspectives

The simulation comparison of MPPT algorithms, conducted in chapter 1, can be expanded to using real hardware. In this way, we can validate the result where MEPO and RSMCA present the best robustness. In addition, our developed algorithm that increases the lifespan of PV panels must be tested to ensure its validation. This task needs a lot of time. In addition, the developed apparatus can be enhanced where the irradiance repartition can be homogenized and the number of temperature sensors can be increased. In adition, we can extend this approach to hybrid PVT solar systems.

Long-term perspectives

Our control approach can be expanded to increase the lifespan of other RES like wind turbines, fuel cells, and even batteries. In addition we can expand our fault analysis and diagnosis to other faults and test our approach using real hardware. Furthermore, we can develop a testing platform for new polymer systems PVT solar modules. It is also important that the developed work on MLP be integrated into EMS (Energy Management Systems).

Bibliography

[1] K. Zweibel and P. Hersch, *Basic photovoltaic principles and methods*. Van Nostrand Reinhold Company, 1984.

[2] A. Luqueand and S. Hegedus, *Handbook of Photovoltaic Science and Engineering*. John Wiley & Sons, 2003.

[3] W. Shockley and H. J. Queisser, "Detailed balance limit of efficiency of p-n junction solar cells," *Journal of applied physics*, vol. 32, no. 3, pp. 510–519, 1961.

[4] N. K. M'Sirdi, B. Nehme, M. Abarkan, and A. Rabbi, "The best mppt algorithms by vsas approach for renewable energy sources (res)," in *Environmental Friendly Energies and Applications (EFEA), 2014 3rd International Symposium on*, pp. 1–7, IEEE, 2014.

[5] H. Zazo, R. Leyva, and E. Castillo, "Analysis of newton-like extremum seeking control in photovoltaic panels," in *International Conference on Renewable Energies and Power Quality (ICREPQ Ś12), Santiago de Compostela, Spain*, 2012.

[6] A. Herguth, G. Schubert, M. Kaes, and G. Hahn, "Avoiding boron-oxygen related degradation in highly boron doped cz silicon," in *Proceedings of the 21st European Photovoltaic Solar Energy Conference*, pp. 530–537, 2006.

[7] S. Kajari-Schröder, I. Kunze, U. Eitner, and M. Köntges, "Spatial and directional distribution of cracks in silicon pv modules after uniform mechanical loads," in *Photovoltaic Specialists Conference (PVSC), 2011 37th IEEE*, pp. 000833–000837, IEEE, 2011.

[8] F. De Lia, S. Castello, and L. Abenante, "Efficiency degradation of c-silicon photovoltaic modules after 22-year continuous field exposure," in *Photovoltaic Energy Conversion, 2003. Proceedings of 3rd World Conference on*, vol. 2, pp. 2105–2108, IEEE, 2003.

[9] N. Zlatov, I. Iliev, A. Terziev, and V. Kamburova, "Influence of climatic data and degradation factor on the efficiency of the photovoltaic modules," in *Research and Education in Mechatronics (REM), 2014 15th International Workshop on*, pp. 1–5, IEEE, 2014.

[10] N. A. of Sciences, "Nae grand chaleenges for engineering web-site," 05 2015. Retrieved on 26/05/2014 from `http://www.zf-laser.com`.

[11] "Study on photovoltaic panels supplementing the impact assessment for a recast of the weee directive.," tech. rep., BIO INTELLIGENCE SERVICE, 2011.

[12] M. Abarkan, N. K. M'Sirdi, and F. Errahimi, "Analysis and simulation of the energy behavior of a building equipped with res in simscape," *Energy Procedia*, vol. 62, pp. 522–531, 2014.

[13] M. Abarkan, F. Errahimi, N. K. M'Sirdi, and A. Naamane, "Analysis of energy consumption for a building using wind and solar energy sources," *Energy Procedia*, vol. 42, pp. 567–576, 2013.

[14] M. Amer, A. Namaane, and N. M'Sirdi, "Optimization of hybrid renewable energy systems (hres) using pso for cost reduction," *Energy Procedia*, vol. 42, pp. 318–327, 2013.

[15] R. Ahmed, A. Namaane, and N. M'Sirdi, "Improvement in perturb and observe method using state flow approach," *Energy Procedia*, vol. 42, pp. 614–623, 2013.

[16] R. Ahmed, A. Naaman, N. M'Sirdi, A. Abdelsalam, and Y. Dessouky, "Sensorless mppt technique for pmsg micro wind turbines based on state-flow," in *Renewable Energies for Developing Countries (REDEC), 2014 International Conference on*, pp. 161–166, IEEE, 2014.

[17] S. Bernard and H. Claudine, *Physique des semi-conducteurs.* Ellipses, 1991.

[18] D. Mezghanni, R. Andoulsi, A. Mami, and G. Dauphin-Tanguy, "Bond graph modelling of a photovoltaic system feeding an induction motor-pump," *Simulation Modelling Practice and Theory*, vol. 15, no. 10, pp. 1224–1238, 2007.

[19] I. Yahyaoui, M. Chaabene, and F. Tadeo, "An algorithm for sizing photovoltaic pumping systems for tomatoes irrigation," in *Renewable Energy Research and Applications (ICRERA), 2013 International Conference on*, pp. 1089–1095, IEEE, 2013.

[20] J. Salazar, F. Tadeo, and L. Valverde, "Predictive control of a renewable energy microgrid with operational cost optimization," in *Industrial Electronics Society, IECON 2013-39th Annual Conference of the IEEE*, pp. 7950–7955, IEEE, 2013.

[21] T. Markvat, *Solar Electricity.* John Wiley & Sons, second edition ed., 2000.

[22] A. Kolodziej, "Staebler-wronski effect in amorphous silicon and its alloys," *Opto-electronics review*, vol. 12, no. 1, pp. 21–32, 2004.

[23] C. H. Henry, "Limiting efficiencies of ideal single and multiple energy gap terrestrial solar cells," *Journal of applied physics*, vol. 51, no. 8, pp. 4494–4500, 1980.

[24] J. E. Granata, J. H. Ermer, P. Hebert, M. Haddad, R. R. King, D. D. Krut, J. Lovelady, M. S. Gillanders, N. H. Karam, and B. T. Cavicchi, "Triple-junction gainp/gaas/ge solar cells-production status, qualification results and operational benefits," in *Photovoltaic Specialists Conference, 2000. Conference Record of the Twenty-Eighth IEEE*, pp. 1181–1184, IEEE, 2000.

[25] M. Veerachary, T. Senjyu, and K. Uezato, "Feedforward maximum power point tracking of pv systems using fuzzy controller," *Aerospace and Electronic Systems, IEEE Transactions on*, vol. 38, no. 3, pp. 969–981, 2002.

[26] A. R. Reisi, M. H. Moradi, and S. Jamasb, "Classification and comparison of maximum power point tracking techniques for photovoltaic system: A review," *Renewable and Sustainable Energy Reviews*, vol. 19, pp. 433–443, 2013.

[27] M. M. Algazar, H. A. EL-halim, M. E. E. K. Salem, *et al.*, "Maximum power point tracking using fuzzy logic control," *International Journal of Electrical Power & Energy Systems*, vol. 39, no. 1, pp. 21–28, 2012.

[28] C. B. Salah and M. Ouali, "Comparison of fuzzy logic and neural network in maximum power point tracker for pv systems," *Electric Power Systems Research*, vol. 81, no. 1, pp. 43–50, 2011.

[29] F. Liu, Y. Kang, Y. Zhang, and S. Duan, "Comparison of p&o and hill climbing mppt methods for grid-connected pv converter," in *Industrial Electronics and Applications, 2008. ICIEA 2008. 3rd IEEE Conference on*, pp. 804–807, IEEE, 2008.

[30] W. Nwesaty, A. I. Bratcu, and A. Hably, "Extremum seeking control techniques applied to photovoltaic systems with multimodal power curves," in *Renewable Energy Research and Applications (ICRERA), 2013 International Conference on*, pp. 85–90, IEEE, 2013.

[31] P. Lall, "Challenges in accelerated life testing," in *Thermal and Thermomechanical Phenomena in Electronic Systems, 2004. ITHERM'04. The Ninth Intersociety Conference on*, vol. 2, pp. 727–Vol, IEEE, 2004.

[32] S. Koch, C. Seidel, P. Grunow, S. Krauter, and M. Schoppa, "Polarization effects and tests for crystalline silicon cells," in *26th European Photovoltaic Solar Energy Conference and Exhibition*, pp. 1726 – 1731, 2011.

[33] J. Berghold, O. Frank, H. Hoehne, S. Pingel, B. Richardson, and M. Winkler, "Potential induced degradation of solar cells and panels," *25th EUPVSEC*, pp. 3753–3759, 2010.

[34] B. Sopori, P. Basnyat, S. Devayajanam, S. Shet, V. Mehta, J. Binns, and J. Appel, "Understanding light-induced degradation of c-si solar cells," in *Photovoltaic Specialists Conference (PVSC), 2012 38th IEEE*, pp. 001115–001120, IEEE, 2012.

[35] R. Swanson, M. Cudzinovic, D. DeCeuster, V. Desai, J. Jürgens, N. Kaminar, W. Mulligan, L. Barbarosa, D. Rose, D. Smith, *et al.*, "The surface polarization effect in high-efficiency silicon solar cells," in *Proceedings of 15th International Photovoltaic Science and Engineering Conference (PVSEC-15), Shanghai, China*, 2005.

[36] M. Hidalgo and F. Medlege, "Procede de caracterisation d'un copolymere d'ethylene et d'acetate de vinyle," Apr. 9 2014. EP Patent App. EP20,120,712,315.

[37] F. Pern, A. Czanderna, K. Emery, and R. Dhere, "Weathering degradation of eva encapsulant and the effect of its yellowing on solar cell efficiency," in *Photovoltaic Specialists Conference, 1991., Conference Record of the Twenty Second IEEE*, pp. 557–561, IEEE, 1991.

[38] P.-O. Westin, P. Neretnieks, and M. Edoff, "Damp heat degradation of cigs-based pv modules," in *21st European Photovoltaic Solar Energy Conference*, pp. 2470–2473, 2006.

[39] S. Kajari-Schršder, I. Kunze, and M. Kšntges, "Criticality of cracks in pv modules," *Energy Procedia*, vol. 27, pp. 658–663, 2012.

[40] G. Mathiak, J. Althaus, S. Menzler, L. Lichtschläger, and W. Herrmann, "Pv module corrosion from ammonia and salt mist - experimental study with fullsize modules," in *27th European Photovoltaic Solar Energy Conference and Exhibition*, 2012.

[41] C. Andersson and J. Liu, "Low cycle fatigue behavior of sn-4.0 ag-0.5 cu lead-free in corrosive environmental conditions," in *Proceedings of the 1st IEEE CPMT Electronics Systemintegration Technology Conference (ESTC2006)*, pp. 457–467, 2006.

[42] E. Lechovič, E. Hodúlová, B. Szewczyková, I. Kovaříková, and K. Ulrich, "Solder joint reliability," *Materials Science and Technology*, vol. 9, pp. 1–8, 2009.

[43] J.-P. M. Clech, D. M. Noctor, J. C. Manock, G. W. Lynott, and F. E. Bader, "Surface mount assembly failure statistics and failure free time," in *Electronic Components and Technology Conference, 1994. Proceedings., 44th*, pp. 487–497, IEEE, 1994.

[44] J.-P. CIech, "Solder reliability solutions: A pc-based design-for-reliability tool*," *Soldering & Surface Mount Technology*, vol. 9, no. 2, pp. 45–54, 1997.

[45] M. D. FAR, *Conversion de L'énergie Solaire Contribution à la Détection de Défaut Dans les Systèmes Photovoltaïques*. PhD thesis, Université de Picardie Jules Verne, 2014.

[46] D. Otth, R. Sugimura, and R. Ross Jr, "Development of design criteria and qualification tests for bypass diodes in photovoltaic applications," in *IN: Institute of Environmental Sciences, Annual Technical Meeting, 31st, Las Vegas, NV, April 30-May 2, 1985, Proceedings (A86-23001 09-38). Mount Prospect, IL, Institute of Environmental Sciences, 1985, p. 242-248. NASA-DOE-sponsored research.*, vol. 1, pp. 242–248, 1985.

[47] Z. Zhang, J. Wohlgemuth, and S. Kurtz, "The thermal reliability study of bypass diodes in photovoltaic modules," *PV Module Reliability Workshop, Golden*, 2013.

[48] N. Pandiarajan and R. Muthu, "Mathematical modeling of photovoltaic module with simulink," in *International Conference on Electrical Energy Systems (ICEES 2011)*, vol. 6, 2011.

[49] G. Walker *et al.*, "Evaluating mppt converter topologies using a matlab pv model," *Journal of Electrical & Electronics Engineering, Australia*, vol. 21, no. 1, p. 49, 2001.

[50] B. Nehme, N. K. M'Sirdi, and T. Akiki, "A geometric approach for pv modules degradation," in *Renewable Energies for Developing Countries (REDEC), 2014 International Conference on*, pp. 49–53, IEEE, 2014.

[51] G. Tina and S. Scrofani, "Electrical and thermal model for pv module temperature evaluation," in *Electrotechnical Conference, 2008. MELECON 2008. The 14th IEEE Mediterranean*, pp. 585–590, IEEE, 2008.

[52] C. H and D. A., "A fundamental overview of accelerated -testing- analytic models," in *Reliability and Maintainability Symposium*, 1998.

[53] P. Hacke, K. Terwilliger, R. Smith, S. Glick, J. Pankow, M. Kempe, S. K. I. Bennett, and M. Kloos, "System voltage potential-induced degradation mechanisms in pv modules and methods for test," in *Photovoltaic Specialists Conference (PVSC), 2011 37th IEEE*, pp. 000814–000820, IEEE, 2011.

[54] F. Pern, "Factors that affect the eva encapsulant discoloration rate upon accelerated exposure," vol. 1, pp. 897–900, 1994.

[55] J.-S. Jeong and N. Park, "Field discoloration analysis and uv/temperature accelerated degradation test of eva for pv," in *Photovoltaic Specialists Conference (PVSC), 2013 IEEE 39th*, pp. 3010–3013, IEEE, 2013.

[56] M. A. Yaklin, D. A. Schneider, K. Norman, J. E. Granata, and C. L. Staiger, "Impacts of humidity and temperature on the performance of transparent conducting zinc oxide," in *Photovoltaic Specialists Conference (PVSC), 2010 35th IEEE*, pp. 002493–002496, IEEE, 2010.

[57] M. D. Kempe, "Control of moisture ingress into photovoltaic modules," in *Photovoltaic Specialists Conference, 2005. Conference Record of the Thirty-first IEEE*, pp. 503–506, IEEE, 2005.

[58] J. Kapur, J. L. Norwood, and C. D. Cwalina, "Determination of moisture ingress rate through photovoltaic encapsulants," in *Photovoltaic Specialists Conference (PVSC), 2013 IEEE 39th*, pp. 3020–3023, IEEE, 2013.

[59] M. Köntges, I. Kunze, S. Kajari-Schröder, X. Breitenmoser, and B. Bjørneklett, "The risk of power loss in crystalline silicon based photovoltaic modules due to micro-cracks," *Solar Energy Materials and Solar Cells*, vol. 95, no. 4, pp. 1131–1137, 2011.

[60] M. Paggi, M. Corrado, and M. A. Rodriguez, "A multi-physics and multi-scale numerical approach to microcracking and power-loss in photovoltaic modules," *Composite Structures*, vol. 95, pp. 630–638, 2013.

[61] M. D. Kempe and J. H. Wohlgemuth, "Evaluation of temperature and humidity on pv module component degradation," in *Photovoltaic Specialists Conference (PVSC), 2013 IEEE 39th*, pp. 0120–0125, IEEE, 2013.

[62] C. Osterwald, J. Adelstein, J. Del Cueto, B. Kroposki, D. Trudell, and T. Moriarty, "Comparison of degradation rates of individual modules held at maximum power," in *Photovoltaic Energy Conversion, Conference Record of the 2006 IEEE 4th World Conference on*, vol. 2, pp. 2085–2088, IEEE, 2006.

[63] D. C. Jordan, B. Sekulic, B. Marion, and S. R. Kurtz, "Performance and aging of a 20-year-old silicon pv system," *Photovoltaics, IEEE Journal of*, vol. 5, no. 3, pp. 744–751, 2015.

[64] D. C. Jordan and S. Kurtz, "Analytical improvements in pv degradation rate determination," in *Photovoltaic Specialists Conference (PVSC), 2010 35th IEEE*, pp. 002688–002693, IEEE, 2010.

[65] D. C. Jordan and S. R. Kurtz, "Photovoltaic degradation rates - an analytical review," *Progress in photovoltaics: Research and Applications*, vol. 21, no. 1, pp. 12–29, 2013.

[66] M. K. Alam, F. Khan, J. Johnson, and J. Flicker, "A comprehensive review of catastrophic faults in pv arrays: Types, detection, and mitigation techniques," *Photovoltaics, IEEE Journal of*, vol. 5, no. 3, pp. 982–997, 2015.

[67] A. Jones and C. Underwood, "A thermal model for photovoltaic systems," *Solar energy*, vol. 70, no. 4, pp. 349–359, 2001.

[68] R. Bharti, J. Kuitche, and M. G. TamizhMani, "Nominal operating cell temperature (noct): Effects of module size, loading and solar spectrum," in *Photovoltaic Specialists Conference (PVSC), 2009 34th IEEE*, pp. 001657–001662, IEEE, 2009.

[69] M. Rosa-Clot, P. Rosa-Clot, and G. Tina, "Tespi: thermal electric solar panel integration," *Solar Energy*, vol. 85, no. 10, pp. 2433–2442, 2011.

[70] S. Armstrong and W. Hurley, "A thermal model for photovoltaic panels under varying atmospheric conditions," *Applied Thermal Engineering*, vol. 30, no. 11, pp. 1488–1495, 2010.

[71] F. M. White, *Heat and Mass Transfer*. Addison Wesley, 1991.

[72] M. Mattei, G. Notton, C. Cristofari, M. Muselli, and P. Poggi, "Calculation of the polycrystalline pv module temperature using a simple method of energy balance," *Renewable Energy*, vol. 31, no. 4, pp. 553 – 567, 2006.

[73] M. A. Djeziri, R. Merzouki, B. O. Bouamama, and G. Dauphin-Tanguy, "Bond graph model based for robust fault diagnosis," in *American Control Conference, 2007. ACC'07*, pp. 3017–3022, IEEE, 2007.

[74] A. Chouder and S. Silvestre, "Automatic supervision and fault detection of pv systems based on power losses analysis," *Energy conversion and Management*, vol. 51, no. 10, pp. 1929–1937, 2010.

[75] L. Bonsignore, M. Davarifar, A. Rabhi, G. M. Tina, and A. Elhajjaji, "Neuro-fuzzy fault detection method for photovoltaic systems," *Energy Procedia*, vol. 62, pp. 431–441, 2014.

[76] M. K. Alam, F. H. Khan, J. Johnson, and J. Flicker, "Pv faults: Overview, modeling, prevention and detection techniques," in *Control and Modeling for Power Electronics (COMPEL), 2013 IEEE 14th Workshop on*, pp. 1–7, IEEE, 2013.

[77] B. J. Fontenault and E. Gutierrez-Miravete, "Modeling a combined photovoltaic-thermal solar panel," in *Comsol Conference, Boston, MA*, pp. 1–8, 2002.

[78] B. Nehme, N. KM'Sirdi, and T. Akiki, "Assessing the effect of temperature on degradation modes of pv panels," in *To be published in MedICT'2015*, 2015.

[79] H. Teo, P. Lee, and M. N. A. Hawlader, "An active cooling system for photovoltaic modules," *Applied Energy*, vol. 90, no. 1, pp. 309–315, 2012.

[80] H. Chen, S. B. Riffat, and Y. Fu, "Experimental study on a hybrid photovoltaic/heat pump system," *Applied Thermal Engineering*, vol. 31, no. 17, pp. 4132–4138, 2011.

[81] D. Yang, Z. Yuan, P. Lee, and H. Yin, "Simulation and experimental validation of heat transfer in a novel hybrid solar panel," *International Journal of Heat and Mass Transfer*, vol. 55, no. 4, pp. 1076–1082, 2012.